Universidad de Oviedo

Programa de Doctorado en Materiales

MATERIALES COMPUESTOS CERÁMICA-METAL NANOESTRUCTURADOS DE INTERÉS TECNOLÓGICO

NANOSTRUCTURED CERAMIC-METAL COMPOSITE MATERIALS OF TECHNOLOGICAL INTEREST

TESIS DOCTORAL

Juan Piñuela Noval

Abril 2024

Universidad de Oviedo

Programa de Doctorado en Materiales

MATERIALES COMPUESTOS CERÁMICA-METAL NANOESTRUCTURADOS DE INTERÉS TECNOLÓGICO

NANOSTRUCTURED CERAMIC-METAL COMPOSITE MATERIALS OF TECHNOLOGICAL INTEREST

TESIS DOCTORAL

Directores de tesis
Dr. D. Adolfo Fernández Valdés
Dr. D. Daniel Fernández González

Universidad de Oviedo

RESUMEN DEL CONTENIDO DE TESIS DOCTORAL

1.- Título de la Tesis	
Español: Materiales compuestos cerámica-metal nanoestructurados de interés tecnológico.	Inglés: Nanostructured ceramic-metal composite materials of technological interest.

2.- Autor	
Nombre: Juan Piñuela Noval	
Programa de Doctorado: Materiales	
Órgano responsable: Centro Internacional de Postgrado	

RESUMEN (en español)

Las exigencias medioambientales, económicas, y sobre todo sociales del siglo XXI han derivado en una búsqueda incansable de nuevos materiales que permitan lograr el progreso tecnológico en todos los sectores, desde la electrónica al transporte, incluyendo la transición energética. En este sentido, los nanocomposites cerámica-metal, y en particular los materiales compuestos de matriz carbonosa (grafito o grafeno) y disperso metálico (molibdeno o cromo), son un campo de investigación prometedor. De esta manera, la tesis se ha dividido en dos grandes líneas, donde el denominador común lo constituye el empleo de materiales compuestos carbono-metal y el uso de la novedosa técnica de sinterización *spark plasma sintering* (SPS), que son:

- El desarrollo de novedosos materiales compuestos grafito-molibdeno y grafito-cromo (grafito con carburos metálicos tras la sinterización) para su empleo en el campo de los disipadores de calor.
- La investigación acerca de nuevos materiales para las baterías Li-ion y Li-sulfuro. Por una parte, la incorporación de nanocomposites grafito-MoC y grafito-Cr_3C_2 en los materiales para los ánodos de baterías de Li-ion. Por otra parte, el desarrollo de nuevos nanocomposites grafeno-MoO_3 para minimizar el *shuttle effect* (fenómeno relacionado con el desplazamiento de los polisulfuros de litio solubles que reduce el contenido de sustancia activa en las baterías y deteriora el comportamiento electroquímico de las mismas) y mejorar el rendimiento electroquímico en las baterías de Li-sulfuro.

Además del método de sinterización, se han empleado otras técnicas novedosas para mejorar la distribución de las segundas fases, como la síntesis coloidal. Por otra parte, los nanocomposites de grafeno-MoO_3 se han obtenido mediante síntesis hidrotermal.

Los composites grafito-molibdeno son una buena alternativa en el campo de los disipadores de calor. En esta tesis doctoral se estudia la influencia del contenido en molibdeno en las propiedades térmicas, eléctricas y mecánicas de estos composites. Se encontró que entre las composiciones estudiadas (2, 5 y 10% vol), la del 10 % en volumen proporcionaba unas buenas propiedades para su utilización en la transmisión de calor, aunque las temperaturas de sinterización para el sistema carbono (grafito)-molibdeno superaban sobradamente los 2400 ºC, de modo que los siguientes trabajos se centraron en estudiar la obtención de materiales densos con propiedades similares pero que se pudieran sinterizar a una temperatura inferior. De esta manera, se indagó en el sistema carbono (grafito)-cromo por la posibilidad de obtener cuerpos densos involucrando fase líquida a temperaturas claramente inferiores (<2000 ºC). En primer lugar, se estudió el efecto del contenido en cromo (0, 1, 2, 2.5, 5, 7 y 10 % vol) para lograr las mejores propiedades térmicas, eléctricas y mecánicas en los composites obtenidos por mezcla mecánica. Se observó que un 7% en volumen de este metal era la mejor opción. Por otra parte, se analizó la utilización de la ruta de síntesis coloidal para obtener las nanopartículas de cromo a partir de precursores químicos en disolución y lograr su mejor distribución en el composite, lo que dio lugar a unas mejores propiedades termo-mecánicas. El composite es competitivo con metales como el aluminio y el cobre para la disipación de calor.

En el campo de las baterías, el empleo de los composites grafito-MoC y grafito-Cr_3C_2 como material anódico en sustitución del grafito en las baterías de ánodo de silicio permite una mejora significativa de las propiedades electroquímicas de las baterías de Li-ion al prolongar el número de ciclos de carga-descarga sin pérdida de la capacidad. Por otra parte, los nanocomposites de grafeno-Mo (óxido), preparados por vía hidrotermal, permiten lograr una disminución del *shuttle effect*, relacionado con los polisulfuros de litio solubles en las baterías de Li-sulfuro, y mejorar las prestaciones electroquímicas de las baterías.

RESUMEN (en Inglés)

Environmental, economic, and especially social requirements of the XXIst century have derived in the pursuit of new materials to achieve the technological progress in all sectors, from electronics to transport, including the energy transition. This way, ceramic-metal nanocomposites and, particularly, the composites with carbon matrix (graphite or graphene) and metallic dispersed phase (molybdenum or chromium), are a promising research field. Therefore, this thesis has divided into two big lines, where the common denominator is the use of carbon-metal composites and the employ of the novel sintering technique of *spark plasma sintering* (SPS). These lines are:

- The development of novel composites of graphite-molybdenum and graphite-chromium (in fact, graphite with metal carbides after sintering) for their use in the field of heat dissipation.
- The investigation about new materials for the Li-ion and Li-sulfur batteries. On the one hand, the incorporation of graphite-MoC and graphite-Cr_3C_2 nanocomposites in the anodic materials of Li-ion batteries. On the other hand, the development of novel graphene-MoO_3 nanocomposites to minimize the shuttle effect (phenomenon related to the displacement of the soluble lithium polysulphides that reduces the quantity of active material in the batteries and deteriorates its electrochemical behavior) and improve the electrochemical performance in the Li-sulfur batteries.

Apart from the sintering method, other novel techniques have been used to improve the distribution of the second phase, i. e. colloidal synthesis route. On the other hand, graphene-MoO_3 nanocomposite has been obtained by hydrothermal synthesis.

Graphite-molybdenum composites are a good alternative in the field of heat dissipation. The influence of the molybdenum content in the thermal, electrical, and mechanical properties in these composites has been studied in this thesis. It is possible to indicate that, from the studied compositions (2, 5 and 10 vol. %), the 10 vol. % reported good properties for the use of the composite in heat transfer although the sintering temperatures in this carbon(graphite)-molybdenum exceeded the 2400 ºC. Thus, the following research aimed at obtained dense composites with similar properties but that could be sintered at lower temperature. Therefore, investigations focused on the carbon (graphite)-chromium system due to the possibility of obtaining dense bodies, involving liquid phase, at temperatures well below than 2000 ºC. First, the role of chromium content was studied by analyzing the composition (0, 1, 2, 2.5, 5, 7 and 10 vol. %) to obtain the composites with the best thermal, electrical, and mechanical properties by mechanical mixing of powders. A 7 vol. % of Cr provided the best results. On the other hand, the utilization of colloidal route to obtain chromium nanoparticles from dissolved chemical precursors and obtain a better distribution in the composite was studied, which reported the best thermal-mechanical properties. The composite is competitive with metals as the aluminum or the copper in the heat dissipation.

In the field of batteries, the use of graphite-MoC and graphite-Cr_3C_2 as anodic material in substitution of the graphite in the batteries of silicon anode allows a significative improvement of the electrochemical properties of the Li-ion batteries as the number of charge-discharge cycles increases without a loss of capacity. On the other hand, graphene-Mo (oxide) nanocomposites, prepared via hydrothermal synthesis, allow a decrease in the *shuttle effect*, related with the soluble lithium polysulphides in the Li-sulfur batteries, improving the electrochemical performance of the batteries.

SR. PRESIDENTE DE LA COMISIÓN ACADÉMICA DEL PROGRAMA DE DOCTORADO EN MATERIALES

AGRADECIMIENTOS

Quisiera expresar mi más sincero agradecimiento a Belén, mi familia y amigos que, directa o indirectamente, han contribuido al desarrollo de lo que es mi Tesis Doctoral.

En primer lugar, quisiera agradecer al Dr. Adolfo Fernández Valdés por haberme dado la oportunidad de realizar todo el trabajo de esta tesis bajo su dirección y por su ayuda, aportaciones, sugerencias, discusiones y apoyo a lo largo de estos años. Por el mismo motivo, agradecer al Dr. Daniel Fernández González por haber codirigido este trabajo y haber estado ahí en todo momento. No puedo obviar la labor del Prof. Dr. Luis Felipe Verdeja González por haberme introducido en el mundillo de la investigación primeramente en el Trabajo Fin de Grado y posteriormente en el Trabajo Fin de Máster, sin olvidar su apoyo en esta Tesis Doctoral, donde ha actuado desde un segundo plano.

Agradecer también al Consejo Superior de Investigaciones Científicas y, en particular, al Centro de Investigación en Nanomateriales y Nanotecnología donde se han llevado a cabo estas investigaciones.

Agradecer la ayuda del Programa "Severo Ochoa" para la formación en investigación y docencia del Principado de Asturias por los fondos recibidos para la realización de esta tesis doctoral (Ref.: BP20 041).

Asimismo, agradecer la ayuda de Estancias Breves en otros Centros de Investigación dentro del programa “Severo Ochoa” por la ayuda recibida para la realización de una estancia predoctoral en la Universidad de la Sapienza (Roma, Italia) durante el año 2022 (Ref.: EB22-11). En este punto es imprescindible mencionar y agradecer su dedicación a Sergio Brutti y Marco Agostini, profesores del Departamento de Química de la Universidad de la Sapienza, y valedores de mi fructífera estancia en Italia.

Por otra parte, las investigaciones relativas a los materiales compuestos de grafito con carburos metálicos se realizaron en el marco del proyecto Ultramateriales de carbono para gestión térmica financiado por el Ministerio de Ciencia e Innovación en la convocatoria del Programa Estatal de I+D+i Orientada a los Retos de la Sociedad [RTI2018-102269-B-I00].

Igualmente, las investigaciones relativas a las baterías se realizaron en el contexto del proyecto Investigación industrial de materiales estratégicos para baterías de ión-litio de alta densidad energética y coste optimizado en electromovilidad sostenible

LiOn-HD dentro de Iniciativas Estratégicas Sectoriales de Innovación Empresarial (Programa "Misiones CDTI"), en el marco del Programa Estatal de Liderazgo Empresarial en 1+D+I, del Plan Estatal de Investigación Científica y Técnica y de Innovación 2017-2020 del Ministerio de Ciencia e Innovación.

Contenido

Resumen 9

Summary 11

1. Introducción 13

2. Técnicas de fabricación 15

2.1. Síntesis Coloidal 15

2.2. Síntesis Hidrotermal 15

2.3. Spark Plasma Sintering (SPS) 16

3. Objetivos 19

4. Disipación de energía: Motivación de la investigación, novedad y discusión de los principales avances en el área. 21

4.1. Sistema grafito-molibdeno 23

4.2. Sistema grafito-cromo 26

5. Almacenamiento de energía: Motivación de la investigación, novedad y principales avances en el área. 31

5.1. Baterías de Ion-Litio (Li-Ion) 32

5.2. Baterías de Litio-Azufre (Li-S) 34

6. Bibliografía 39

7. Artículos publicados 55

Artículo 1: Effect of Mo content on the properties of graphite–MoC composites sintered by spark plasma sintering. 59

Artículo 2: Characterization of graphite–chromium carbide composites manufactured by spark plasma sintering. 69

Artículo 3: Spark plasma sintering of graphite-chromium carbide composites: Influence of the sintering temperature and powder synthesis method. 81

Artículo 4: Metal carbide additives in graphite-silicon composites for Lithium-Ion batteries 93

Artículo 5: Modifying reduced graphene oxide substrate with Mo/MoO_3: benefits on Li/S cell performance. 103

9. Conclusiones y trabajos a futuro 123

9.1. Disipadores de calor 123

9.2. Almacenamiento de energía 124

10. Conclusions and future work 127

10.1. Heat sinks 127

10.2. Energy storage... 128

Resumen

Las exigencias medioambientales, económicas, y sobre todo sociales del siglo XXI han derivado en una búsqueda incansable de nuevos materiales que permitan lograr un progreso tecnológico representado por una mejora de las prestaciones de éstos. Esta indagación abarca todos los campos, pero el de la gestión de la energía tiene una importancia significativa para contribuir al avance de todos los sectores, desde la electrónica al transporte, incluyendo la tan afamada transición energética. En este sentido, los nanocomposites cerámica-metal, y en particular los materiales compuestos de matriz carbonosa (grafito o grafeno) y disperso metálico (molibdeno o cromo), son un campo de investigación realmente prometedor. De esta manera, la tesis se ha dividido en dos grandes líneas, donde el denominador común lo constituyen el empleo de materiales compuestos carbono-metal y el uso de la novedosa técnica de sinterización *spark plasma sintering* (SPS), que son:

- El desarrollo de novedosos materiales compuestos grafito-molibdeno y grafito-cromo (en realidad, grafito-carburo de molibdeno y grafito-carburo de cromo tras la sinterización) para su empleo en el campo de los disipadores de calor.
- La investigación acerca de nuevos materiales para las baterías Li-ion y Li-S. Por una parte, la incorporación de nanocomposites grafito-MoC y grafito-Cr_3C_2 en los materiales para los ánodos de baterías de Li-ion. Por otra parte, el desarrollo de nuevos nanocomposites grafeno-Mo para minimizar el *shuttle effect* (fenómeno relacionado con el desplazamiento de los polisulfuros de litio solubles que reduce el contenido de sustancia activa en las baterías y deteriora el comportamiento electroquímico de las mismas) y mejorar el rendimiento electroquímico en las baterías de Li-S.

Además de la mencionada sinterización empleando la tecnología SPS, se han empleado otras técnicas novedosas orientadas a lograr una mejor distribución de las segundas fases en los nanocomposites, como la síntesis coloidal. Por otra parte, los nanocomposites de grafeno-Mo se han obtenido mediante síntesis hidrotermal.

Así pues, teniendo en consideración las líneas de trabajo anteriormente expuestas, se puede decir que, por una parte, los composites grafito-molibdeno son una buena alternativa en el campo de los disipadores de calor, presentándose en esta tesis doctoral trabajos orientados a estudiar la influencia del contenido en molibdeno en las propiedades térmicas, eléctricas y mecánicas de estos composites. Se encontró que entre

las composiciones estudiadas (2, 5 y 10% en volumen), la del 10 % en volumen proporcionaba unas buenas propiedades para su utilización en la transmisión de calor. En cualquier caso, las temperaturas de sinterización para el sistema carbono (grafito)-molibdeno involucrando fase líquida superaban sobradamente los 2400 ºC de acuerdo con los diagramas de fases, de modo que los siguientes trabajos se centraron en estudiar la posibilidad de obtener materiales densos con propiedades similares a las obtenidas en el caso del sistema carbono (grafito)-molibdeno pero que se pudieran sinterizar a una temperatura inferior. Así pues, se estudió el sistema carbono (grafito)-cromo por la posibilidad de obtener cuerpos densos involucrando fase líquida a temperaturas claramente inferiores. De esta manera, en primer lugar, se hizo un estudio acerca de que contenido en cromo (0, 1, 2.2.5, 5, 7 y 10 % en volumen) proporcionaba las mejores propiedades térmicas, eléctricas y mecánicas en los composites de grafito-cromo obtenidos por mezcla mecánica de los materiales de partida y se observó que un 7% en volumen de este metal era la mejor opción. Por otra parte, conocido el hecho de que la ruta coloidal permite lograr una mejor distribución de las segundas fases en composites de matriz cerámica, se estudió esta ruta de síntesis para obtener las nanopartículas de cromo a partir de precursores químicos en disolución y se observó que, aparte de la reducción en la temperatura de sinterización (<2000 ºC), se lograba una mejor distribución de la segunda fase en el composite y unas mejores propiedades termo-mecánicas. El composite es competitivo con metales como el aluminio y el cobre para la disipación de calor.

En el campo de las baterías, el empleo de los composites grafito-MoC y grafito-Cr_3C_2 como material anódico en sustitución del grafito en las baterías de ánodo de silicio permite una mejora significativa de las propiedades electroquímicas de las baterías de Li-ion al prolongar el número de ciclos de carga-descarga sin que se produzca una pérdida de la capacidad. Por otra parte, los nanocomposites de grafeno-Mo (óxido), preparados por vía hidrotermal, permiten lograr una disminución del *shuttle effect*, relacionado con los polisulfuros de litio solubles en las baterías de Li-S, y mejorar las prestaciones electroquímicas de las baterías.

De esta manera, esta tesis contribuye al diseño y procesamiento de materiales compuestos con matriz carbonosa y segunda fase de carburos de metal (o metal) para el campo de la gestión de la energía, tanto en el campo de los disipadores de calor como en el de las baterías.

Summary

Environmental, economic and, particularly, social requirements of the XXIst century have derived in an indefatigable search for new materials that could be suitable for the technological progress, represented by an improvement of the features of these materials. This inquiry includes all the fields, but that of the energy management has a relevant importance to contribute to the progress of all the sectors, from that of the electronics to that of the transport, including the renowned topic of the energy transition. Therefore, the ceramic-metal nanocomposites and, in particular, the composites of carbon matrix (graphite or graphene) and metallic dispersed second phase (molybdenum or chromium), are a really promising field of research. Thus, this doctoral thesis has divided into two big lines, where the common denominators are the use carbon-metal composites and the utilization of the novel sintering technique known as *spark plasma sintering* (SPS), which are:

- The development of novel composites of graphite-molybdenum and graphite-chromium (in fact, graphite-molybdenum carbide, and graphite-chromium carbide after sintering) for their use in the field of heat dissipation.
- The investigation about new materials for the Li-ion and Li-S batteries. On the one hand, the incorporation of graphite-MoC and graphite-Cr_3C_2 nanocomposites in the anodic materials of Li-ion batteries. On the other hand, the development of novel graphene-Mo nanocomposites to minimize the *shuttle effect* (phenomenon related to the displacement of the soluble lithium polysulphides that reduces the quantity of active material in the batteries and deteriorates its electrochemical behavior) and improve the electrochemical performance in the Li-S batteries.

Apart from the already mentioned sintering using the SPS technology, other novel techniques oriented to achieve a better distribution of the second phases in the nanocomposites were employed in this doctoral thesis. This is the case of the colloidal synthesis. On the other hand, the graphene-Mo nanocomposites have been obtained by hydrothermal synthesis.

Therefore, considering the above-reported research lines, it is possible to indicate that, on the one hand, the graphite-molybdenum composites are a suitable alternative in the field of heat dissipation. Thus, the influence of the molybdenum

content in the thermal, electrical, and mechanical properties of the composites was studied in this doctoral thesis. Results indicate that from the studied compositions (2, 5 and 10 vol. %), that of 10 vol. % provides good properties to be used in heat transfer. In any case, sintering temperatures for the carbon (graphite)-molybdenum system involving liquid phase exceed the 2400 ºC according to the phase diagrams. This way, the following works focused on studying the possibility of obtaining dense materials with similar properties to those obtained in the case of the carbon (graphite)-molybdenum system but that could be sintered at a lower temperature. Therefore, the carbon (graphite)-chromium system was studied due to the possibility of obtaining dense bodies involving liquid phase at clearly lower temperatures. Thus, first, a study about the chromium content (0, 1, 2.2.5, 5, 7 and 10 vol. %) was made to analyze the content that provided the best thermal, electrical, and mechanical properties in the graphite-chromium composites obtained by mechanical mixing of the starting materials. A 7 vol. % was observed to be the best option. On another note, known the fact that the colloidal synthesis route allows obtaining a better distribution of the second phases in the ceramic matrix composites, this route of synthesis was studied to obtain chromium nanoparticles as second phase from chemical precursors in solution and it was checked that, apart from the reduction of the sintering temperature (<2000 ºC), better both distribution of the second phase in the composite and thermal-mechanical properties were observed. The composite is competitive with metals as the aluminum and the copper for the heat dissipation.

In the field of batteries, the use of graphite-MoC and graphite-Cr_3C_2 as anodic material in substitution of the graphite in the batteries of silicon anode allows a significative improvement of the electrochemical properties of the Li-ion batteries as the number of charge-discharge cycles increases without a loss of capacity. On the other hand, graphene-Mo (oxide) nanocomposites, prepared via hydrothermal synthesis, allow a decrease in the *shuttle effect*, related with the soluble lithium polysulphides in the Li-S batteries, improving the electrochemical performance of the batteries.

Therefore, this doctoral thesis contributes to the design and processing of composites with carbonaceous matrix and second phase comprising metal carbides (or metal) for the field of the energy management, either in the field of heat dissipation or in the topic of batteries.

1. Introducción

Los materiales cerámicos han jugado un papel relevante en el progreso de la humanidad, desde los primeros recipientes y útiles hasta los más recientes cerámicos avanzados empleados en salud o almacenamiento energético. La investigación y desarrollo en el campo de estos materiales, la cual ha tenido mayor énfasis en las últimas décadas, ha sido vital en el avance de otras tecnologías emergentes, contribuyendo al desarrollo de sectores económicos e industriales como los de la automoción, la metalurgia, la energía o el medio ambiente, entre otros.

Sin embargo, las cerámicas técnicas-avanzadas disponibles en el mercado en ocasiones no cumplen con los requerimientos demandados por las cada vez más exigentes aplicaciones derivadas de las innovaciones tecnológicas que hacen progresar a nuestra sociedad. Esto se debe a que no es sencillo combinar en un mismo material cerámico unas excelentes propiedades mecánicas junto con otras funcionalidades necesarias para su aplicación.

Una estrategia para superar algunas de las limitaciones expuestas anteriormente, y aportar otras propiedades, es el desarrollo de nuevos composites cerámica-metal, los cuales permiten lograr una mejora de las propiedades mecánicas y proporcionar propiedades funcionales, como la mejora de las propiedades térmicas y eléctricas. Representan, por lo tanto, una categoría avanzada de materiales que ha surgido como una alternativa innovadora y eficiente en diversas aplicaciones, destacando especialmente en campos como la industria aeroespacial, automotriz y, de manera significativa, en el sector de la energía (*Cardinal y otros, 2009*).

Estos materiales compuestos, de matriz cerámica y una segunda fase integrada por un constituyente metálico, presentan propiedades únicas y beneficios distintivos que los hacen atractivos para una variedad de aplicaciones (*Aramian y otros, 2023*) como, por ejemplo, el almacenamiento y la disipación de energía, que es la temática sobre la que pivota esta tesis doctoral. Para ello en este trabajo se recurre a los materiales de carbono para la matriz, y a diferentes metales (molibdeno y cromo) como segunda fase.

La investigación presentada en este documento, partiendo de un punto común como es el empleo composites de carbono-metal, toma dos caminos distintos marcados por la funcionalidad: nuevos materiales para la fabricación de disipadores de calor y composites que busquen la mejora en la eficiencia energética de baterías Li-ion y Li-S. En ellos, la clave, y parte común, es la implementación de técnicas de fabricación avanzadas para obtener composites carbono-metal que puedan cumplir las funciones que se les requieren, véase propiedades mecánicas combinadas con una buena conductividad térmica y bajos coeficientes de expansión térmica en el primer caso, y propiedades mecánicas combinadas con buen comportamiento electroquímico en el segundo caso.

2. Técnicas de fabricación

El desarrollo de los materiales de matriz carbonosa y segunda fase metálica lleva asociadas a su vez dificultades de fabricación para conseguir materiales completamente densos y con el control microestructural deseado. Por ello, previo paso a la introducción de cada línea de investigación se explican tres técnicas de fabricación que son la base de esta tesis doctoral. Por una parte, en lo que a la preparación de polvos se refiere se describen las técnicas: Síntesis Coloidal e Hidrotermal. Por otra parte, por lo que respecta a la obtención del composite denso se presenta la tecnología Spark Plasma Sintering (SPS). En cualquier caso, cada artículo que acompaña a esta tesis doctoral contiene una detallada explicación de la metodología experimental empleada en cada caso. No obstante, parece oportuno incluir una descripción de las técnicas novedosas y fundamentales empleadas en estos trabajos.

2.1. Síntesis Coloidal

El método de síntesis coloidal es una ruta de obtención de materiales a partir de precursores orgánicos o inorgánicos disueltos en un medio líquido. La técnica se ha empleado ampliamente en la síntesis de diferentes tipos de materiales incluyendo, nanopartículas metálicas, de óxidos o de otros tipos de compuestos (*Gu Kwon y Hyeon, 2008*; *Velikov y otros, 2003*). La ruta coloidal es también una alternativa prometedora para la preparación de nanocomposites cerámicos con constituyentes dispersos metálicos (óxidos y carburos entre otros) debido a una mejor distribución de la segunda fase en el compuesto, resultando un material más homogéneo en composición y, por lo tanto, en propiedades (*Kedzierska-Sar y otros, 2021*; *Moreno, 2017*; *Fernández-González, y otros, 2023*), para lo que se puede interactuar con el tipo de precursor, la concentración o el pH, entre otros parámetros.

2.2. Síntesis Hidrotermal

La ruta hidrotermal tiene sus orígenes en el campo de la geología a mediados del siglo XIX cuando los geólogos simulaban condiciones hidrotermales para estudiar la formación de ciertos minerales y rocas. Posteriormente, el método se aplicó al crecimiento de cristales y preparación de polvos, haciendo de esta una técnica de gran potencial para la preparación de nanocomposites de matriz cerámica. En la ruta hidrotermal se parte de disoluciones acuosas que se someten posteriormente a elevadas presiones y temperaturas, por lo general empleando reactores a presión. De esta manera, ocurren reacciones heterogéneas en presencia de solventes acuosos y agentes complejantes que se disuelven y cristalizan en las condiciones de elevada presión y temperatura de los autoclaves, cosa que no ocurriría en condiciones ordinarias. Esta tecnología es transversal y ha sido empleada por investigadores y expertos de diferentes campos y tecnologías como la geología, la biología, la física, la cerámica, la metalurgia, la ingeniería o la ciencia de los materiales (*Parr Instrument Company, 2019*; *Yang y Park, 2019*). La síntesis hidrotermal es una de las técnicas más ampliamente empleadas para la preparación de nanomateriales (*Gan y otros, 2020*) y, en particular, de polvos cerámicos y nanocomposites de matriz cerámica (*Kaya y otros, 2002*; *Ortiz-Landeros y otros, 2012*; *Suchanek y Riman, 2006*; *Vignesh Raj y otros, 2018*).

2.3. Spark Plasma Sintering (SPS)

La sinterización por descarga de plasma, o spark plasma sintering (SPS) por su denominación en inglés, es una técnica de sinterización que se basa en la aplicación simultánea de una presión uniaxial y una corriente eléctrica pulsada bajo una atmósfera controlada (habitualmente en vacío, aunque se puede operar en atmósfera de argón, nitrógeno o hidrógeno según se requiera) para lograr de manera rápida, temperaturas por encima de 2000 ºC (*Suárez, y otros, 2013*). Esta combinación permite la consolidación rápida de polvos. Las elevadas velocidades de calentamiento y enfriamiento, junto con el efecto de la presión, permiten lograr altas densificaciones sin producir un crecimiento significativo del tamaño de grano manteniéndose, por lo tanto, las características nanoestructuradas o nanométricas de los polvos de partida, existiendo, pues, una disociación entre la densificación del material y el crecimiento del tamaño de grano. El paso de la corriente a través de los polvos, que se calientan por efecto Joule en las fronteras de grano, es la diferencia fundamental con otras técnicas similares como el Hot Isostatic Pressing (HIP), y uno de los fundamentos de la tecnología SPS, que permite acortar los tiempos de sinterización con respecto a otras competidoras (*Suárez, y otros, 2013*). Sin embargo, más allá del particular método de consolidación de polvos, el *Spark Plasma Sintering* es una tecnología que permite interactuar con una gran cantidad de variables como las relacionadas con la corriente (afectando al calentamiento), la temperatura, la presión o la atmósfera de trabajo, para lograr composites densos nanoestructurados.

La aplicación de corriente eléctrica para asistir a la sinterización fue iniciada en los años 30 con los trabajos de Taylor en el campo de los carburos cementados (*EEUU Patente nº US Patent No. 1,896,854, 1933*), aunque no fue hasta los años 90 cuando la Sumitomo Heavy Industries Ltd. (Japón) desarrolló las primeras máquinas comerciales de spark plasma sintering (*Yanagisawa y otros, 1994*). Desde entonces, la investigación en este campo ha alcanzado a la gran mayoría de familias de materiales, y en particular, el campo de los cerámicos y composites de matriz cerámica ha sido un área de intenso trabajo (*Cardinal y otros, 2009*) (*Stuer y otros, 2020*). En la **Ilustración 1** se muestra un esquema del funcionamiento de la tecnología SPS.

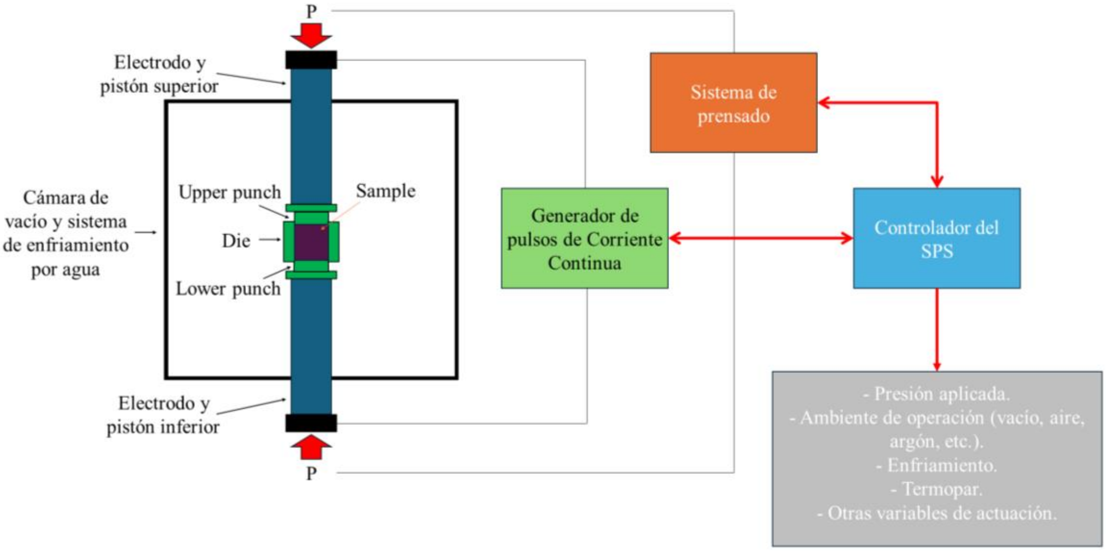

Ilustración 1. Esquema de funcionamiento de la tecnología SPS.

3. Objetivos

La investigación recogida en esta tesis doctoral se centra en dos campos de gran relevancia en la actualidad: la disipación de calor y el almacenamiento de energía. Así pues, el objetivo general de estos trabajos es la obtención de nuevos materiales compuestos de matriz carbonosa y disperso metálico para su utilización en los campos anteriormente descritos. De esta manera, los objetivos específicos se dividen en dos bloques en función de la aplicación:

- Materiales de grafito-metal (carburo) para su uso en disipadores de calor:
    - Estudiar la influencia del contenido en molibdeno en las propiedades térmicas, eléctricas y mecánicas de los composites grafito-molibdeno obtenidos por síntesis coloidal y spark plasma sintering.
    - Analizar el sistema grafito-cromo para reducir la temperatura de sinterización con relación al sistema grafito-molibdeno. Para ello se plantea estudiar la influencia del contenido en cromo, el método de fabricación de los polvos (ruta de mezcla mecánica y síntesis coloidal) y la temperatura de sinterización para obtener el compacto denso, empleando la tecnología SPS.
- Materiales de carbono-metal (carburo) para su empleo en baterías:
    - Demostrar que el empleo de los composites de grafito-MoC o grafito-Cr_3C_2 anteriores como reemplazo de parte del grafito que junto con el silicio constituye el material anódico de las baterías Li-ion conduce a un incremento de la estabilidad frente al ciclado de carga y descarga con relación a los ánodos fabricados únicamente de grafito y silicio.
    - Evaluar el papel de los composites grafeno-molibdeno (óxido) obtenidos por ruta hidrotermal como un material para minimizar los problemas relacionados con la descarga de polisulfuros de litio en las baterías de Li-S (*shuttle effect*), que conducen a pérdidas de material activo y merman las prestaciones electroquímicas en este tipo de baterías.

4. Disipación de energía: Motivación de la investigación, novedad y discusión de los principales avances en el área.

La disipación de energía es un aspecto clave para cualquier dispositivo electrónico o máquina, pues permitirá prolongar la vida útil de estos. Por este motivo, todos ellos llevan incorporados disipadores de calor, siendo elementos pasivos que transfieren el calor generado desde el foco caliente a un foco frío (un líquido o gas refrigerante, normalmente aire), y permiten regular la temperatura de trabajo de los equipos. Por otra parte, el progreso tecnológico tiende en este campo a la miniaturización de dispositivos, y al aumento de la ligereza, eficiencia y vida útil, lo que viene demandando nuevos materiales que vengan a satisfacer estos requisitos, ya que muchos de los materiales actualmente empleados no presentan las prestaciones suficientes para enfrentarse a estas demandas, dando lugar a deterioros más frecuentes y, por ende, mayores costes (*Li y otros, 2010*). En línea con lo anteriormente expuesto, hay que tener en consideración que la vida útil de un dispositivo se reduciría a la mitad cuando la temperatura aumenta 10 ºC (*Rho, y otros, 2021*) y, además de la selección de materiales, el diseño de los disipadores va a desempeñar un papel importante, aunque este último aspecto trascienda al ámbito de esta tesis doctoral. Por lo que respecta a la cuestión del material, las propiedades que este ha de cumplir para su empleo en disipación de calor han de ser que, además de altas conductividades térmica y eléctrica, posea un bajo coeficiente de expansión térmica, o al menos similar a la de los demás componentes del dispositivo (*Schubert, y otros, 2007a*), y baja densidad para no incrementar el peso del equipo.

Históricamente, los metales y sus aleaciones han sido los materiales empleados para la fabricación de disipadores de calor gracias a su elevada conductividad térmica (*Schubert, y otros, 2007a*). Entre los más usados encontramos:

- Aluminio: Su conductividad térmica (cercana a 250 W/mK), su ligereza, bajo coste y adecuada maquinabilidad lo hacen muy interesante para este propósito, a pesar de tener grandes limitaciones por su bajo punto de fusión y su elevado coeficiente de expansión térmica ($25.5 \cdot 10^{-6}$ K^{-1}) (*Pero-Sanz y otros, 2019*).

- Cobre: Posee una conductividad térmica que ronda los 400 W/mK y puede ser usado a altas temperaturas, aunque, de igual manera, su coeficiente de expansión térmica es bastante elevado ($16.7 \cdot 10^{-6}$ K^{-1}) (*Schubert, y otros, 2007a*). Por otro lado, es más pesado y caro. Para superar estas limitaciones y otras como el creep o el bajo punto de fusión (1085 ºC), se han desarrollado nuevos composites con matriz de cobre: cobre-carburo de silicio (*Schubert, y otros, 2007b*), cobre-molibdeno (*Shen y otros, 2012*), cobre-titanio (*Yang y otros, 2019*), y cobre-nitruro de aluminio (*Lee y otros, 2007*). Merece la pena destacar el material compuesto cobre-wolframio (*Kim y otros, 2001*), cuyo valor de conductividad térmica es elevado incluso a altas temperaturas (> 300 W/mºC a 1000 ºC, aunque los mejores valores fueron medidos a 500 ºC).

Adicionalmente, en estos últimos años se han comenzado a incorporar materiales carbonosos a estos metales para disminuir su densidad y aumentar la conductividad térmica. En un primer momento se empleó el diamante en aplicaciones térmicas (en especial en la industria microelectrónica) debido a su alta resistividad eléctrica y alta conductividad térmica (*Hausmann, y otros, 2010*), siendo el material conocido con su valor más elevado (> 2200 W/mK) (*Greaber, 1995*; *Kidalov y Shakhov, 2009*): cobre-diamante (*Shen y otros, 2012*; *Chu y otros, 2010*)**,** Cu-0.2% Ti/diamante (*Yang y otros, 2019*), Cu-0.3 % en peso de B/diamante (*Bai, y otros, 2018*) y Cu-0.5 % en peso de Zr/diamante (*Li y otros, 2015*; *Wang y otros, 2019*).

No obstante, el elevado coste del diamante, así como su escasez, lo hacen inviable para su uso masivo en electrónica y disipación de calor. Como alternativa, el diamante sintético ha sido empleado como segunda fase en composites (Cu, Al, Ag y SiC) (*Yoshida y Morigami, 2009*; *Battabyal y otros, 2008*)**,** al igual que la fibra de carbono (*Prakasam y otros, 2020*). Recientemente, las investigaciones se han centrado en el empleo de otro alótropo de carbono, el grafeno (*Ghosh y otros, 2008*; *Malekpour y otros, 2014*), aunque todavía no existe información precisa acerca de si su empleo mejora (*Nazeer y otros, 2019*) o no (*Rho y otros, 2021*) la conductividad térmica de los materiales compuestos de matriz metálica.

Una alternativa a estudiar para mejorar las prestaciones de los disipadores de calor es el material carbonoso por excelencia, el grafito. Este material posee bajos coste y densidad, estabilidad química, bajo coeficiente de expansión térmica, propiedades mecánicas aceptables, y buena conductividad eléctrica y térmica cuando es adecuadamente sinterizado (*Chung, 2002*; *Sengupta y otros, 2011*). Para alcanzar las exigencias tecnológicas actuales en el campo de la energía, este material es combinado con metales de diversa índole como segunda fase: aluminio (*Oddone y otros, 2017*;

Chen y Huang, 2013), magnesio (*Oddone y otros, 2017*) y cobre (*Yang y otros, 2013*; *Byun y otros, 2019*). Esta familia de materiales lleva estudiándose desde hace más 50 años (*White y Pontelandolfo, 1966*; *Harada y Rubin, 1966*), pero no ha sido hasta la década del 2010 cuando los composites de matriz grafítica y como segunda fase metales reactivos (molibdeno, niobio, tantalio y hafnio, entre otros) han recibido atención en campos avanzados (*Matthews, 1970*), como la alta velocidad, la industria aerospacial o la investigación en física de partículas (colimadores y aceleradores de partículas) (*Mariani, 2014*; *Italia Patente nº PCT/EP2013/072818, 2016*), debido a las excelentes prestaciones que ofrecen: baja densidad, carácter refractario, buenas propiedades mecánicas y elevada conductividad térmica.

4.1. Sistema grafito-molibdeno

De entre todos los composites de grafito-metal (carburo), destaca sobremanera el composite grafito-molibdeno por su extraordinarias características para su uso en los colimadores del Large Hadron Collider en las instalaciones del CERN (Conseil Européen pour la Recherche Nucléaire) (*Guardia-Valenzuela y otros, 2018*). Para incrementar las prestaciones de este composite para esta aplicación se incorpora a su composición una o más fases adicionales (i.e. titanio, fibras de carbono, silicio, carburo de silicio o wolframio). Así, se evitan, entre otras cuestiones, transformaciones cristalográficas indeseadas y que algunas fases formadas a elevada temperatura existan a temperatura ambiente (por ejemplo, el MoC) o se mejoran características del composite como la resistencia a la oxidación a elevadas temperaturas, las propiedades mecánicas o la conductividad térmica. Más allá de investigar la incorporación de fases adicionales al composite grafito-molibdeno (carburo), la investigación en este campo se ha centrado en la sinterización empleando técnicas no convencionales basadas en el calentamiento a elevadas temperaturas con aplicación simultánea de presión. Se puede encontrar varios estudios en esta línea:

- Nicola Mariani (*Mariani, 2014*) obtuvo el material compuesto de grafito con carburo de molibdeno mediante rapid hot pressing (10 min) a elevadas temperaturas (1700 ºC). Este proceso requirió la aplicación de presión constante a 45 MPa en vacío (10^{-4} mbar) y en una atmósfera reductora (97% N_2 – 3% H_2).

- Por su parte, Alessandro Bertarelli y Stefano Bizarro (*Italia Patente nº PCT/EP2013/072818, 2016*) fabricaron el composite grafito-MoC mediante mezclado de polvos, compactación en verde (10-20 MPa) y hot pressing a una temperatura comprendida entre 2500 y 2600 ºC, así como una presión superior a 35 MPa.

- Jorge Guardia-Valenzuela y sus compañeros (*Guardia-Valenzuela y otros, 2018*) prepararon materiales compuestos de grafito-carburo de Mo-carburo de Ti partiendo de grafito, molibdeno y titanio metal. La mezcla de polvos se realizó en una máquina de mezclado 3D para, después, ser compactados en una prensa uniaxial a 300 MPa y sinterizados mediante la tecnología SPS a temperaturas superiores a 2500 ºC.

Finalmente, nuestro centro también ha estado involucrado en la investigación acerca de los materiales compuestos del sistema grafito-molibdeno. Uno de los primeros trabajos consistió en el empleo de la ruta de síntesis coloidal para preparar polvos del material compuesto grafito-Mo- Ti, que luego se sinterizaron en el equipo SPS para obtener los cuerpos densos de grafito con los carburos metálicos (*Suárez y otros, 2021*). Por comparación con los polvos de la misma composición preparados por mezcla mecánica en molinos de atricción (y sinterizados en el SPS), se observó una sustancial mejora en las propiedades térmicas, eléctricas y mecánicas. Por otra parte, el otro de los trabajos se centró en analizar la influencia que ejercía la etapa de prensado en frío para obtener el compacto en verde en las propiedades finales del material compuesto sinterizado también empleando la tecnología SPS (*Suárez, y otros, 2022*). En ambos casos se pudo comprobar que empleando una temperatura de sinterización 600 ºC inferior a la de Jorge Guardia-Valenzuela (que llegaba en su caso a los 2600 ºC, *Guardia-Valenzuela y otros, 2018*), se lograba un composite plenamente funcional para el campo de la disipación de calor. Este hecho conduciría a un acortamiento de los tiempos de sinterización y podría traducirse en un potencial ahorro energético. Sumado a ello, el segundo trabajo también reveló que con un prensado uniaxial de 60 MPa para obtener los compactos en verde era posible obtener unas propiedades adecuadas para el campo de la disipación de calor. Sirva de referencia el hecho de que en los composites obtenidos por Jorge Guardia-Valenzuela, las presiones empleadas para obtener el cuerpo verde llegaban a los 300 MPa (*Guardia-Valenzuela y otros, 2018*).

En esta línea todavía existen algunos factores pendientes de ser estudiados, como es la influencia que el contenido en molibdeno podría tener en la propiedades del composite grafito-molibdeno. De esta manera, el primer artículo que sustenta esta tesis doctoral se centra en este aspecto:

- Marta Suárez, Daniel Fernández-González, Luis Antonio Díaz, ***Juan Piñuela-Noval***, Amparo Borrell, José Serafín Moya, Ramón Torrecillas, Adolfo Fernández, 2023: *Effect of Mo content on the properties of graphite–MoC composites sintered by spark plasma sintering*, Boletín de la Sociedad Española de Cerámica y Vidrio, 62(6), 588-596. https://doi.org/10.1016/j.bsecv.2023.02.005

Así pues, el ***primer artículo de esta tesis doctoral*** versa sobre la influencia del contenido de molibdeno en las propiedades de los composites grafito-carburo de molibdeno (MoC) preparados mediante síntesis coloidal y SPS para aplicaciones de disipación de energía. De esta manera, a partir de cloruro de molibdeno, como precursor del molibdeno, se depositaron nanopartículas del precursor en diferentes contenidos (2.5, 5.0 y 10.0 % en volumen) sobre el grafito, que tras una serie de tratamientos térmicos intermedios se transformaron en molibdeno. Posteriormente, los polvos obtenidos por la ruta de síntesis coloidal se compactaron en verde a 15 MPa y se sinterizaron mediante la técnica *spark plasma sintering* para obtener grafito con carburo de cromo a una temperatura inferior a la que se reportaba en *Guardia-Valenzuela y otros, 2018*. Se pudo constatar que las mejores propiedades (densidad, conductividad eléctrica en el plano, conductividad térmica en el plano y la resistencia a flexión) se lograron cuando el contenido metálico era más elevado (10.0 % en volumen), respectivamente: 2.50 ± 0.02 g/cm^3, 1.07 ± 0.04 MS/m, 255.35 ± 44.01 W/m °C y 53.45 ± 8.27 MPa. Considerando la propiedad más relevante de cara a la disipación de calor la conductividad térmica en el plano, k, su valor relativo en relación con la densidad, ρ, es: k/ρ, lo que nos permite efectuar una comparativa con otros trabajos realizados en nuestro grupo de investigación para diferentes composiciones (en el caso del primer artículo de la tesis este valor alcanzó **102.1**). Así pues, los valores obtenidos son:

- *Suárez, y otros, 2021:* 81.8 (síntesis coloidal, 10% en volumen Mo)
- *Suárez, y otros, 2022:* 79.2 (mezcla mecánica, 5.5% en volumen Mo)
- *Aluminio:* 87.8 (conductividad térmica: 237 W/m ºC)
- *Cobre:* 43.0 (conductividad térmica: 385.2 W/m ºC)

De acuerdo con estos resultados, podemos decir que el material compuesto obtenido en este trabajo es competitivo con otros de la misma familia y con otros materiales habitualmente empleados en el campo de la disipación de calor.

En cualquier caso, el empleo de molibdeno en estos materiales tiene múltiples ventajas, pero existe un inconveniente que es oportuno mencionar: la temperatura necesaria de sinterización para la sinterización en presencia de fase líquida en el sistema grafito-molibdeno requiere alcanzar temperaturas por encima de los 2000 ºC. De esta manera, alcanzar estas temperaturas de sinterización que permiten unos extraordinarios valores de densificación para materiales de naturaleza grafítica es todavía un desafío en el mundo del I+D. Es necesario tener en cuenta que estas condiciones de sinterización extremas conducen a ciclos largos que merman la productividad de la tecnología SPS y redundan en un deterioro prematuro de los equipos, que se ven obligados a trabajar en unas condiciones bordeando los límites de operación del equipo.

4.2. Sistema grafito-cromo

La problemática de la temperatura de sinterización se puede afrontar con el estudio de otros sistemas grafito-metal. En cualquier caso, las prestaciones, siempre pensando en su potencial aplicación como disipadores de calor, deben ser análogas a las obtenidas en el caso del composite grafito-molibdeno. El elemento objeto de estudio en este caso fue el cromo (Cr), el cual posee un carácter similar al molibdeno, pero su temperatura de fusión, de acuerdo con el diagrama carbono-cromo recogido en la **Ilustración 2**, es significativamente más baja (1907 ºC) (*Venkatraman y Neumann, 1990*), y presenta reacciones invariantes a temperaturas inferiores a las que se observan en el caso del diagrama carbono-molibdeno (**Ilustración 3**). Así pues, si en el caso del sistema grafito-molibdeno se requerían temperaturas para la sinterización en presencia de fase líquida superiores a los 2600 ºC, en el caso del sistema grafito-cromo los composites densos se podrían obtener en el SPS a temperaturas inferiores a los 2000 ºC. Estas cuestiones, así como el rol del cromo, que se transforma en carburo de cromo (Cr_3C_2) tras la sinterización, en las propiedades térmicas y mecánicas, han sido objeto de discusión en los siguientes dos artículos que constituyen esta tesis doctoral.

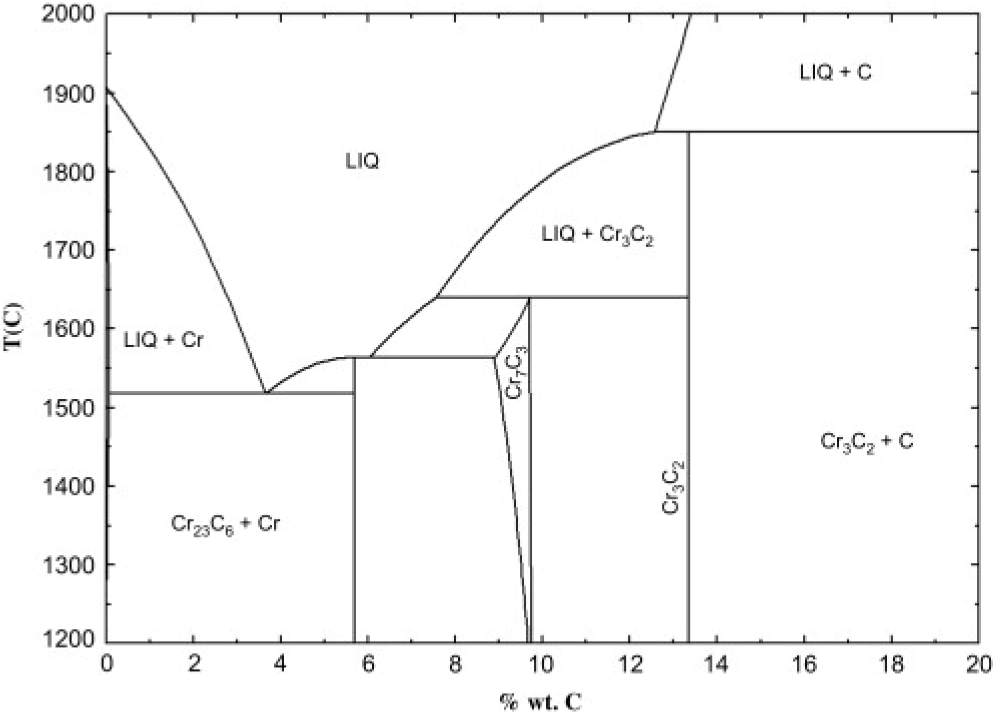

Ilustración 2. Diagrama carbono-cromo (*Gasik y otros, 2013*).

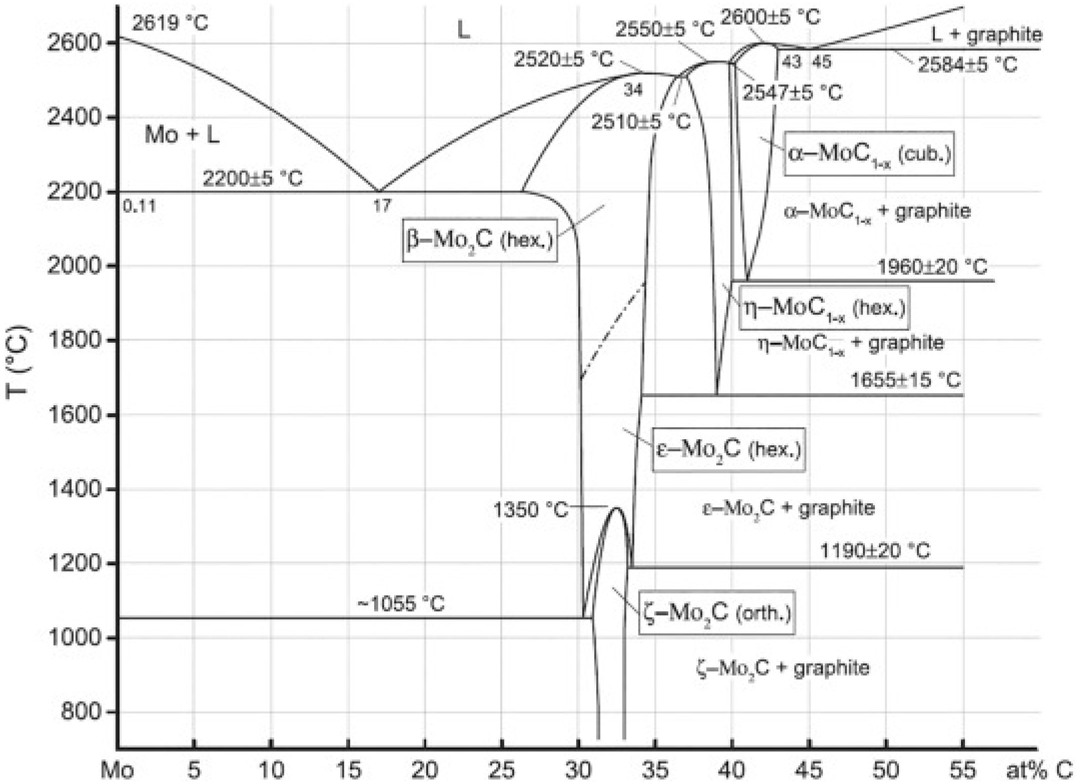

Ilustración 3. Diagrama carbono-molibdeno (*Braun y otros, 2020*).

- ***Juan Piñuela-Noval***, Daniel Fernández-González, Marta Suárez, Luis Antonio Díaz, Luis Felipe Verdeja, Adolfo Fernández, 2023: *Characterization of graphite–chromium carbide composites manufactured by spark plasma sintering*, Journal of the American Ceramic Society, 106(9), 5157-5166. https://doi.org/10.1111/jace.19145

El ***segundo artículo de esta tesis doctoral*** aborda el estudio del papel que tendría el contenido en cromo en las propiedades eléctricas, térmicas y mecánicas de los materiales compuestos grafito-cromo preparados a partir de mezclas de polvos de grafito y cromo metal. Se estudiaron diferentes contenidos en cromo (0, 1, 2, 5, 7 y 10 % en volumen), y la densificación se llevó a cabo mediante la tecnología SPS a una temperatura de 1800 ºC de acuerdo con el diagrama de fases recogido en la **Ilustración 2**. En este sentido es necesario tener en cuenta que a 1850 ºC existe una reacción invariante que implica la presencia de fase líquida y, dado que las condiciones de operación en el SPS conducen a un desplazamiento de estas transformaciones hacia temperaturas inferiores, la temperatura de sinterización escogida fue de 1800 ºC. Los polvos se presaron uniaxialmente antes del SPS a 60 MPa, y la sinterización se realizó en condiciones de vacío y con una presión aplicada de 30 MPa. La densificación alcanzada en estas condiciones se aproximó al 90% para el composite con un 7 % en volumen de cromo, el cual es un valor comparable al de los materiales grafíticos policristalinos (*Aguiar y otros, 2020*). Mayores contenidos en cromo no dieron lugar a mejoras debido a pérdidas de material por extrusión del metal fundido hacia las paredes del molde. Las propiedades (densidad, conductividad eléctrica en el plano, conductividad térmica en el plano y la resistencia a flexión) del material compuesto con un 7% en volumen de cromo fueron: 2.2932 g/cm^3, 0.79 ± 0.14 MS/m, 264 W/m K y 38.97 MPa, respectivamente. Esto nos da un valor de la conductividad térmica relativa de 115.1, que estaría por encima del valor que se había obtenido en el caso del composite de grafito con un 10% en volumen de molibdeno.

Como se había visto en la literatura, la ruta de síntesis coloidal era adecuada para lograr una distribución más homogénea de la segunda fase en el composite y así mejorar las propiedades de éste. Este estudio fue objeto del siguiente artículo de la tesis doctoral.

- ***Juan Piñuela-Noval***, Daniel Fernández-González, Marta Suárez, Cristian Gómez-Rodríguez, Adolfo Fernández, 2023: *Spark plasma sintering of graphite-*

chromium carbide composites: Influence of the sintering temperature and powder synthesis method, Ceramics International, 49(21), 33891-33900. https://doi.org/10.1016/j.ceramint.2023.08.083

Así pues, el ***tercer artículo de la tesis doctoral*** se dedicó a comparar los métodos de mezcla mecánica de polvos de partida y síntesis coloidal para la obtención de materiales compuestos de grafito con un 7% en volumen de cromo. De esta manera, se estudió si la forma de preparar los polvos afectaba al tamaño y distribución de la segunda fase. Por otra parte, se investigó la influencia de la temperatura de sinterización en las propiedades del material compuesto de matriz grafítica. Es estudio se llevó a cabo desde de los 1600 hasta los 2000 ºC. En este sentido, se logró una densificación superior al 90% para muestras obtenidas por síntesis coloidal, con valores próximos al 95% para las muestras sinterizadas a 1900 ºC. Para esta última se logran las siguientes propiedades (densidad, conductividad eléctrica en el plano, conductividad térmica en el plano y la resistencia a flexión) en el material compuesto de grafito con un 7% en volumen de cromo: 2.48 g/cm^3, 0.7509 MS/m, 370.1 W/m·K, y 117.5 MPa. Así pues, la conductividad térmica relativa alcanza un valor **149.2**, lo que nos indica que este composite podría ser competitivo con otros materiales de matriz grafítica, y con otros materiales típicamente empleados en disipación de calor como el cobre y el aluminio. Adicionalmente, este composite de grafito con 7% en volumen de cromo resulta más ligero que estos metales y presenta un menor coeficiente de expansión térmica.

5. Almacenamiento de energía: Motivación de la investigación, novedad y principales avances en el área.

El despliegue de las energías renovables junto con la electrificación de la sociedad tiene en la actualidad un papel clave en la descarbonización. En este sentido, cobran gran importancia los sistemas de almacenamiento de energía para hacer frente a la producción irregular de las energías renovables asociada a la disponibilidad del recurso renovable o a la existencia de dispositivos y equipos portátiles con mayor autonomía y durabilidad, desde el vehículo eléctrico hasta el reproductor portátil de música. Así pues, se han de buscar sistemas de almacenamiento eficientes, duraderos, de gran autonomía y capacidad y de menor coste. Por ello, muchas de las investigaciones en este campo se están centrando en dos grandes grupos de tecnologías electroquímicas que satisfagan estos requisitos: baterías y tecnologías de hidrógeno basadas en electrolizadores y pilas de combustible (*Kulova y otros, 2018*).

Dentro del mundo de las baterías eléctricas, históricamente han ido apareciendo diferentes generaciones de baterías que buscaban superar las limitaciones de las anteriores, ya fuera en capacidad, como en fiabilidad, durabilidad o coste, entre otros aspectos. Así pues, en la **Ilustración 4** se puede encontrar una comparativa entre los diferentes tipos de baterías por orden de invención y densidad energética: baterías plomo-ácido (*Bode 1977*), níquel-cadmio (*Jeyaseelan y otros, 2020*), níquel-hidruro metálico (MH) (*Feng y otros, 2001*), litio-ion (*Winter y otros, 2018*), litio-azufre (*Bruce y otros, 2012*) y litio-oxígeno (*Bruce y otros, 2012*). Actualmente, las baterías de iones de litio están dominando el campo del almacenamiento de energía, siendo las de Li-S las que parecen presentar un futuro más prometedor. De esta manera, en esta tesis doctoral se recogen investigaciones acerca de materiales avanzados para mejorar algunas de las prestaciones de las baterías Li-ion y Li-S que, entre otras cuestiones, impiden su uso masivo en dispositivos eléctricos y electrónicos.

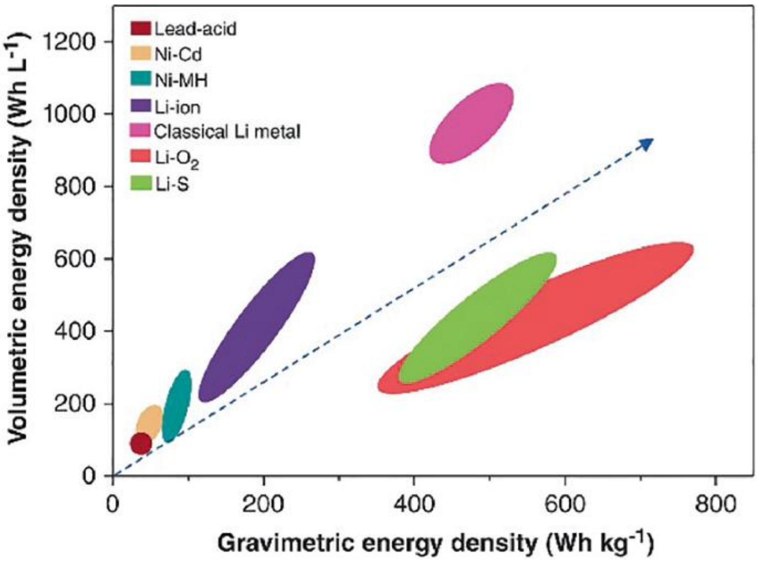

Ilustración 4. Comparativa de las distintas baterías electroquímicas existentes y en desarrollo en la actualidad (Demiryürek y otros, 2022).

5.1. Baterías de Ion-Litio (Li-Ion)

Las baterías de ion-litio, funcionando con un voltaje de aproximadamente 3.7 V y exhibiendo una densidad energética de alrededor de 220 Wh/kg (*Tarascon y Armand, 2001*), se utilizan hoy en día ampliamente en dispositivos portátiles dentro de los mercados electrónicos pudiendo lograr tasas de carga rápida con una buena durabilidad. Sin ir más lejos, la tecnología de iones de litio fue galardonada en 2019 con el Premio Nobel de Química por la invención del primer prototipo de batería Li-Ion con un cátodo (electrodo positivo) de $LiCoO_2$ y un ánodo (electrodo negativo) de grafito (*Ramanan 2019*). Con la creciente necesidad de reducir los combustibles fósiles se está prestando atención al empleo de nuevas familias de baterías para alimentar vehículos eléctricos, con el objetivo final de llegar a cero emisiones en un período corto.

Sin embargo, varias razones obstaculizan la generalización de las baterías de Li-Ion (*Kim y otros, 2020*), muchas de ellas relacionadas con el campo de los materiales, que conducen a valores de densidad energética limitados (*Xia y Yin, 2023*; *Kim y otros, 2019*), pese al gran potencial teórico que ofrecen este tipo de baterías. Una de las principales limitaciones de las baterías de Li-Ion se encuentra en el material del ánodo, que hoy en día se fabrica a nivel comercial en grafito, donde el almacenamiento de litio está termodinámicamente limitado por el mecanismo de intercalación y desintercalación de Li^+ en las capas del grafeno que integra el grafito, y proporciona valores de capacidad de 372 mAh g^{-1} (*Chae y otros, 2019*; *Kim y otros, 2020*; *Chaves y otros, 2021*). Como alternativa al ánodo de grafito, el silicio se presenta como una alternativa debido a su alta capacidad teórica (3579 mAh g^{-1}) gracias al compuesto formado durante la litiación ($Li_{15}Si_4$), el bajo potencial de trabajo (aproximadamente 0,4 V vs. Li^+/Li), la abundancia natural y la no toxicidad (*Kim y otros, 2020*). No obstante, el desarrollo de ánodos de silicio comerciales sigue siendo un gran desafío, ya que los grandes cambios de volumen de las partículas de silicio durante el proceso de (de)litiación (superior al 300%) conducen a la fractura del silicio y a la deformación, pulverización y delaminación del electrodo (*Chae y otros, 2019*; *Xia y Yin, 2023*). Además, las partículas de Si catalizan la descomposición del electrolito con un crecimiento incontrolable de una capa sólida semiconductora (SEI, *Solid Electrolyte Interphase* layer) con una baja conductividad eléctrica ($6{,}7\times10^{-1}$ S cm^{-1}) lo que limita la tasa de carga (*Yoon y otros, 2015*; *Aurbach 2020*).

Para abordar los problemas anteriores, se han adoptado diferentes enfoques en la última década. Uno de ellos es emplear silicio nanoestructurado (nanopartículas, yolk-shell o nanowires entre otros) (*Li y otros, 2017*; *Wagner y otros, 2019*), compuestos (*Li y otros, 2021*; *Moyassari y otros, 2022*), aglutinantes poliméricos (*Li y otros, 2022*) (*Hamzelui y otros, 2021*), y aditivos (*Esthetu y Figgemeier, 2019*; *Zhou y otros, 2021*) para mejorar el rendimiento de los electrodos de Si en celdas de Li.

Intercalar carburos metálicos en ánodos de silicio es otra estrategia que aún no se ha explorado en detalle para aumentar la capacidad y el ciclo de vida de los electrodos en las baterías de Li-Ion. En este sentido, investigadores han empleado un compuesto de silicio/carburo de wolframio-grafeno con una particular microestructura que ha permitido mantener una alta eficiencia culómbica y ciclo de vida prolongado, aliviando las modificaciones sufridas por la estructura debido a los cambios de volumen antes mencionados (*Sun y otros, 2016*). Por otro lado, otros académico han observado que el empleo de carburos metálicos (Mo_2C, Cr_2C_3, etc.) formando electrodos con silicio y grafeno proporcionaban un buen rendimiento electroquímico (*Liu y otros, 2019*). Además, los carburos, en general, pueden generar también un excelente esqueleto conductor para mejorar la conductividad eléctrica del silicio, gracias a la presencia de nanocanales conductores que reducen la resistencia a la transferencia de electrones (*Pan y otros, 2021*; *Xu y otros, 2023*).

Es precisamente en la línea de emplear carburos metálicos para mejorar las prestaciones de los ánodos de las baterías de Li-Ion en la que se han centrado las investigaciones que se presentan en esta tesis doctoral.

- ***Juan Piñuela-Noval***, Daniel Fernández-González, Sergio Brutti, Marta Suárez, Franco Mazzei, Maria Assunta Navarra, Luis Felipe Verdeja, Adolfo Fernández, Marco Agostini, 2023: *Metal Carbide Additives in Graphite-Silicon Composites for Lithium-Ion Batteries*, ChemElectroChem, 10(21), e202300339. https://doi.org/10.1002/celc.202300339

En este ***cuarto artículo de la tesis doctoral*** se han desarrollado materiales compuestos de grafito-silicio-carburos metálicos (MoC o Cr_3C_2) para su empleo como material activo anódico de baterías de Li-Ion. Los composites de grafito con carburos metálicos fueron obtenidos mediante el empleo de la tecnología SPS, y fueron mezclados con un 20% de silicio en forma de nanopartículas. Las propiedades electroquímicas de este nuevo material anódico fueron comparadas con las del material anódico fabricado con polvo de grafito, análogo al empleado para preparar los composites con carburos, y 20% de silicio, y las de material anódico en la que el material carbonoso era grafito con calidad específica para baterías. De esta manera, se ha observado que se mejoraba considerablemente la estabilidad electroquímica de las celdas electroquímicas Li-ion por encima de los 400 ciclos sin una evidencia de caída en la capacidad específica (en el rango 200-250 $mAh \cdot g^{-1}$) para los ánodos fabricados con silicio y carburos metálicos, especialmente en el caso del composite de silicio-grafito-MoC. De esta manera, la presencia de los carburos metálicos en la matriz de grafito produce efectos beneficiosos en términos de propiedades mecánicas, permitiendo soportar los cambios de volumen tan bruscos (de más del 300%) generados en los procesos de litiación y delitiación. Asimismo, se formará una SEI layer menos compacta que conduce, también, a unas mejores prestaciones electroquímicas.

5.2. Baterías de Litio-Azufre (Li-S)

Las baterías de Li-Ion tienen gran importancia en el campo del almacenamiento de energía (*Kulova y otros, 2020*). Sin embargo, esta tecnología ha llegado casi a sus límites y todavía se caracteriza por su alto coste, lo que plantea la necesidad del desarrollo de tecnologías que den solución a algunas de estas cuestiones (*Demiryüreky otros, 2022*). Así es posible encontrar otras familias, como las de Li-O_2, Li-metal o Li-S, cuyas capacidades y densidades electroquímicas (Wh/kg) son netamente superiores a las existentes en las baterías Li-Ion (**Ilustración 4**).

Dentro de las nuevas generaciones de baterías, las de Li-S (LSB) son una tecnología prometedora para desarrollar sistemas innovadores de almacenamiento de energía electroquímica de alta capacidad gracias a su elevada densidad energética teórica (> 2600 Wh/kg) (*Benveniste y otros, 2018*), estando basadas en compuestos de intercalación (*Wang y otros, 2014*) y donde el azufre desempeña un papel fundamental. Una serie de aspectos juegan a favor del azufre y son el hecho de que se trata del elemento más abundante en la corteza terrestre, tiene un bajo coste y es relativamente seguro para los humanos y el medio ambiente (*Ahn y otros, 2009*), lo que se podría traducir en una potencial ventaja competitiva con respecto a otras familias de baterías (*Agostini y otros, 2018a*; *Lee y otros, 2018*).

La celda Li-S basa su funcionamiento en la reacción redox de conversión $2Li+S \leftrightarrow Li_2S$ (*Zhu y otros, 2019*). En la **Ilustración 5** figura una imagen del funcionamiento de las baterías de Li-S. A pesar de su simplicidad sobre el papel, el mecanismo real es mucho más complejo e incluye la formación de polisulfuros de litio intermedios (Li_2S_x, donde $4 \leq x \leq 8$) que son altamente solubles en el electrolito líquido orgánico. Este fenómeno es la principal fuente de pérdidas del material activo durante el ciclado, activando el llamado *shuttle effect* que acelera la muerte de la celda electroquímica (*Su y otros, 2018*). Sumado a esto, también se reportan otros problemas que impiden aún su comercialización (*Agostini y otros, 2018b*). De forma más específica, se hacen necesarias grandes cantidades de electrolito para un eficiente funcionamiento de la batería, lo que conduce a una disminución de la energía específica de las baterías de litio-azufre (*Shen y otros, 2019*). Además, está el problema de la autodescarga, que se debe a la interacción química del electrodo de litio metal con el azufre y los polisulfuros de litio en el electrolito (*Knap y otros, 2016*).

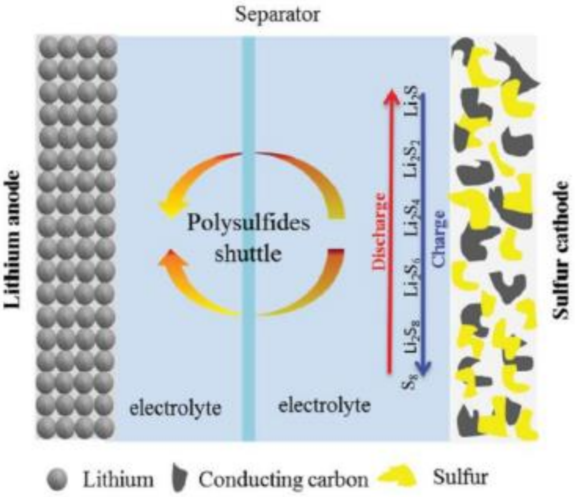

Ilustracion 5. Representación esquemática del funcionamiento de las baterías Li-S (Kaiser y otros, 2017).

Una estrategia adecuada en el diseño de electrodos se basa en evitar la disolución del azufre en el electrolito para que no se formen los polisulfuros, para lo que se trata de encapsular el azufre en materiales carbonosos (*Agostini y otros, 2018a*). Asimismo, los compuestos azufre-carbono muestran una buena conductividad eléctrica al tiempo que proporcionan un buen confinamiento físico del azufre, lo que limita la disolución de los polisulfuros durante el ciclado electroquímico (*Wu y otros, 2019*; *Ren y otros, 2019*). Muchos materiales se han estudiado como base para el azufre en electrodos de LSB: carbones micro y mesoporosos (*Sun y otros, 2013*; *Ko y otros, 2022*), aerogeles de carbono (*Balakumar y Kalaiselvi, 2015*; *Liu y otros, 2016*) o nanotubos de carbono (*Razzaq y otros, 2019*; Zheng y otros, 2019). Recientemente, el grafeno se está utilizando también en este campo (*Zhang y otros, 2018*; *Kamisan y otros, 2022*). Desde su descubrimiento (*Müllen 2013*), se han identificado numerosas potenciales aplicaciones para este alótropo de carbono debido a sus prometedoras propiedades (*Xu 2018*; *Wypych 2019*), particularmente en el campo de la electroquímica. Sin embargo, la problemática de los polisulfuros no puede evitarse totalmente con el simple confinamiento físico del azufre en un material de carbono poroso, es, por lo tanto, necesaria la funcionalización de los materiales de carbono, en particular del grafeno. En cualquier caso, la decoración del grafeno con diferentes materiales está ampliamente reportada en la literatura (*Khan y otros, 2017*) no solo en el tema de las baterías (*Kim y otros, 2018*), sino en muchos otros campos como la conversión de energía (*Covarrubias-García y otros, 2020*; *Wu y otros, 2020*), catalizadores (*Lin y otros, 2020*; *Mateo-Mateo y otros, 2019*), sensores (*Rodner y otros,* *2020*; *Rattan y Goswamy, 2022*), electroquímica (*Song y otros, 2012*), óptica y fotocatálisis (*Hu y otros, 2011*) o superconductividad (*Ciudad 2015*). En este contexto, la modificación superficial del grafeno para su empleo en baterías de litio-azufre se considera una forma eficaz de suprimir el desplazamiento de polisulfuros debido a la fuerte interacción química de estos, altamente iónicos, con la superficie del material inorgánico, habiéndose probado varios materiales inorgánicos funcionales como aditivos en los electrodos de base grafeno para LSB: óxidos metálicos (*Li y otros, 2019*), sulfuros metálicos (*Xiao y otros, 2017*)**,** nitruros (*Sun y otros, 2017*), metal (*Liu y otros, 2021*), nitrógeno (*Yuan y otros, 2018*), fosfuros metálicos (*Liu y otros, 2020*), carburos metálicos (*Niu y otros, 2020*) o hidróxidos (*Tian y otros, 2019*).

En esta línea, en esta tesis doctoral se han desarrollado nanocomposites de óxido de grafeno reducido (rGO) decorados con MoO_3 para mejorar las prestaciones electroquímicas de las baterías de Li-S.

- ***Juan Piñuela-Noval***, Daniel Fernández-González, Marta Suárez, Luis Felipe Verdeja, Arcangelo Celeste, Adriano Pierini, Franco Mazzei, Maria Assunta Navarra, Sergio Brutti, Adolfo Fernández, Marco Agostini, 2024: *Enhancement of Li/S battery performance by a modified reduced graphene oxide carbon host decorated with MoO_3*, enviado a ChemSusChem.

En el ***quinto artículo de la tesis doctoral*** se han desarrollado nanocomposites de óxido de grafeno reducido decorados con óxido de molibdeno (VI) preparados mediante la ruta de síntesis hidrotermal. El material sintetizado se empleó como material activo para los electrodos en un 80% junto con un 10% de PVDF (fluoruro de polivinilideno) y un 10% de carbono de calidad específica para el campo de las baterías. El empleo del material desarrollado en este tipo de baterías logra una mejora en las interacciones del S_8 y el Li_2S_n con el electrodo, lo que permite incrementar la estabilidad electroquímica de la batería, la cual presenta una capacidad específica en el entre 600 y 700 $mAh\cdot g^{-1}$ durante un número de ciclos por encima de los 250. En este sentido, el óxido de molibdeno con el que se funcionaliza el grafeno contribuye como un eficiente *scavenger* de polisulfuros, confinando el material activo en el lado del cátodo y previniendo las migraciones al ánodo de litio. De esta manera, se evidencia una mejora de las prestaciones de las baterías de Li-S con el empleo del rGO-MoO_3.

6. Bibliografía

Agostini, M., Hwang, J.-Y., Kim, H., Bruni, P., Brutti, S., Croce, F., Matic, A., Sun, Y.-K. (2018a). Minimizing the electrolyte volume in Li-S batteries: A step forward to high gravimetric energy density. *Adv Energy Mater*, 8(26), 1801560. https://doi.org/10.1002/aenm.201801560

Agostini, M., Lim, D.-H., Sadd, M., Hwang, J.-Y., Brutti, S., Heo, J., Ahn, J.H., Sun. Y.K., Matic, A. (2018b). Rational design of low cost and high energy lithium batteries through tailored fluorine-free electrolyte and nanostructured S/C composite. *ChemSusChem*, 11(17), 2981-2986. https://doi.org/10.1002/cssc.201801017

Aguiar, J.A., Kwon, S., Coryell, B.D. Eyerman, E., Bokov, A.A., Castro, R.H.R., Burns, D., Hartmann, H.T., Luther, E.P. (2020). Densification of graphite under high pressure and moderate temperature. *Materials Today Comunications*, 22, 100821. https://doi.org/10.1016/j.mtcomm.2019.100821

Ahn, H.-J., Kim, K.-W., Ahn, J.-H., & Cheruvally, G. (2009). Secondary batteries - lithium rechargable systems: All-solid state battery. En: *Encyclopedia of Electrochemical Power Sources* (editor Jürgem Garche), Elsevier, Boston, 155-161. https://doi.org/10.1016/B978-044452745-5.00210-0

Aramian, A., Sadeghian, Z., Narimani, M., Razavi, N., & Berto, F. (2023). A review on the microstructure and properties of TiC and Ti(C,N) based cermets. *Int J Refract Met H*, 115, 106230. https://doi.org/10.1016/j.ijrmhm.2023.106320

Aurbach, D. (2020). Review of selected electrode–solution interactions which determine the performance of Li and Li ion batteries. *J Power Sources*, 89(2), 206–218. https://doi.org/10.1016/S0378-7753(00)00431-6

Bai, G., Li, N., Wang, X., Wang, J., Kim, M., Zhang, H. (2018). High thermal conductivity of Cu-B/diamond composites prepared by gas pressure infiltration. *J Alloys Compd*, 735, 1648-1653. https://doi.org/10.1016/j.jallcom.2017.11.273

Balakumar, K., Kalaiselvi, N. (2015). High sulfur loaded carbon aerogel cathode for lithium–sulfur batteries. *RSC Adv*, 5, 34008-34018. https://doi.org/10.1039/C5RA01436K

Battabyal, M., Beffort, O., Kleiner, S., Vaucher, S., Rohr, L. (2008). Heat transport across the metal-diamond interface. *Diam Relat Mater*, 17 (7-10), 1438-1442. https://doi.org/10.1016/j.diamond.2008.01.023

Benveniste, G., Rallo, H., Canals Casals, L., Merino, A., Amante, B. (2018). Comparison of the state of Lithium-Sulphur and Lithium-Ion batteries applied to electromobility. *J Environ Manage*, 226, 1-12. https://doi.org/10.1016/j.jenvman.2018.08.008

Bertarelli, A., Bizarro, S. (2016). A molybdenum carbide/carbon composite and manufacturing method. *Italia Patente nº PCT/EP2013/072818.*

Bode, H. (1977). *Lead-acid batteries.* United States: OSTI.GOV. Obtenido de https://www.osti.gov/biblio/6653002

Braun, J., Kaserer, L., Letofsky-Papst, I., Leitz, K.-H., Kestler, H., Leichtfried, G. (2020). On the role of carbon in molybdenum manufactured by Laser Powder Bed Fusion. *Int J Refract Met H*, 92, 105283. https://doi.org/10.1016/j.ijrmhm.2020.105283

Bruce, P., Freunberger, S., Herdwick, L., Tarascon, J.-M. (2012). Li–O_2 and Li–S batteries with high energy storage. *Nat Mat*, 11(1), 19-29. https://doi.org/10.1038/nmat3191

Byun, M., Kim, D., Sung, K., Jung, J., Song, Y.-S., Park, S., Son, I. (2019). Characterization of copper–graphite composites fabricated via electrochemical deposition and spark plasma sintering. *Appl Sci*, 9(14), 2853. https://doi.org/10.3390/app9142853

Cardinal, S., Malchère, A., Garnier, V., Fantozzi, G. (2009). Microstructure and mechanical properties of TiC-TiN based cermets for tools application. *Int J Refract Met Hard Mater*, 27(3), 521-527. https://doi.org/10.1016/j.ijrmhm.2008.10.006

Chae, S., Choi, S.-H., Kim, N., Sung, J., Cho, J. (2019). Integration of graphite and silicon anodes for the commercialization of high-energy Lithium-Ion batteries. *Angew Chem Int Ed*, 59(1), 110-135. https://doi.org/10.1002/anie.201902085

Chaves, C., Pereira, E., Ferreira, P., Dias, A. (2021). Concerns about lithium extraction: A review and application for Portugal. *The Extractive Industries and Society*, 8(3), 100928. https://doi.org/10.1016/j.exis.2021.100928

Chen, J., Huang, I. (2013). Thermal properties of aluminum–graphite composites by powder metallurgy. *Compos Part B: Eng*, 44(1), 698-703. https://doi.org/10.1016/j.compositesb.2012.01.083

Chu, K., Liu, Z., Jia, C., Chen, H., Liang, X., Gao, W., Tian, W., Guo, H. (2010). Thermal conductivity of SPS consolidated Cu/diamond composites with Cr-coated diamond particles. *J Alloys Compd*, 490(1-2), 453–458. https://doi.org/10.1016/j.jallcom.2009.10.040

Chung, D. (2002). Review graphite. *J Mater Sci*, 37, 1475-1489. https://doi.org/10.1023/A:1014915307738

Ciudad, D. (2015). Lithium-decorated graphene. *Nat Mat*, 14, 1075. https://doi.org/10.1038/nmat4472

Covarrubias-García, I., Quijano, G., Aizpuru, A., Sánchez-García, J. L., Rodríguez-López, J. L., Arriaga, S. (2020). Reduced graphene oxide decorated with magnetite nanoparticles enhance biomethane enrichment. *J Hazard Mater*, 397, 122760. https://doi.org/10.1016/j.jhazmat.2020.122760

Demiryürek, R., Nurullah Ates, M., Tunaboylu, B. (2022). Future of lithium Ion batteries for electric vehicles: Problems and expected developments. *The International Symposium for Production Research: Towards Industry 5.0* (págs. 524-540). Antalya: Springer. https://doi.org/10.1007/978-3-031-24457-5_42

Esthetu, G., Figgemeier, E. (2019). Confronting the challenges of next-generation silicon anode-based Lithium-Ion batteries: Role of designer electrolyte additives and polymeric binders. *ChemSusChem*, 12(12), 2488-2828. https://doi.org/10.1002/cssc.201900209

Feng, F., Geng, M., Northwood, D. (2001). Electrochemical behaviour of intermetallic-based metal hydrides used in Ni/metal hydride (MH) batteries: a review. *Int J Hydrogen Energ*, 26(7), 725-734. https://doi.org/10.1016/S0360-3199(00)00127-0

Fernández-González, D., Suárez, M., Piñuela-Noval, J., Díaz, L., Gómez-Rodríguez, C., García Quiñonez, L., Borrell, Fernández, A. (2023). Alumina/molybdenum nanocomposites obtained by colloidal synthesis and spark plasma sintering. *Ceram Int*, 49(6), 9432-9441. https://doi.org/10.1016/j.ceramint.2022.11.108

Gan, Y., Jayatissa, A., Yu, Z., Chen, X., Li, M. (2020). Hydrothermal synthesis of nanomaterials. *J Nanomater*, Article ID 8917013. https://doi.org/10.1155/2020/8917013

Gasik, M.I. (2013). Chapter 8 - Technology of Chromium and Its Ferroalloys. En: Handbook of Ferroalloys (editado por Michael Gasik), Londres: Elsevier, 267-316. https://doi.org/10.1016/B978-0-08-097753-9.00008-3

Ghosh, S., Calizo, I., Teweldebrhan, D., Pokatilov, E., Nika, D., Balandin, A., Bao, W., Lau, C. (2008). Extremely high thermal conductivity of graphene: prospects for thermal management applications in nanoelectronic circuits. *Appl Phys Lett*, 92, 151911.

Greaber, J. (1995). Thermal conductivity of diamond. En: *Diamond: Electronic Properties and Applications. The Kluwer International Series in Engineering and Computer Science* (editado por L. Pan, y D. Kania). Boston: Springer.

Gu Kwon, S., Hyeon, T. (2008). Colloidal Chemical Synthesis and Formation Kinetics of Uniformly Sized Nanocrystals of Metals, Oxides, and Chalcogenides. *Acc Chem Res*, 41(12), 1696–1709.

Guardia-Valenzuela, J., Bertarelli, A., Carra, F., Mariani, N., Bizarro, S., Arenal, R. (2018). Development and properties of high thermal conductivity molybdenum carbide-graphite composites. *Carbon*, 135, 72-84.

Hamzelui, N., Esthetu, G., Figgemeier, E. (2021). Customizing active materials and polymeric binders: stern requirements to realize silicon-graphite anode based Lithium-Ion batteries. *J Energy Storage*, 35, 102098.

Harada, Y., Rubin, G. (1966). Fabrication and characterization of metal carbide-graphite composites. *Paper presented at the 68th Annual Meeting of the American Ceramic Society*. Washington DC.

Hausmann, B., Khan, M., Zhang, Y., Babinec, T., Martinick, K., McCutcheon, M., Hemmer, P.R., Loncar, M. (2010). Fabrication of diamond nanowires for quantum information processing applications. *Diam Relat Mater*, 19(5-6), 621-629.

Hu, H., Wang, X., Liu, F., Wang, J., Xu, C. (2011). Rapid microwave-assisted synthesis of graphene nanosheets–zinc sulfide nanocomposites: Optical and photocatalytic properties. *Synthetic Met*, 161(5-6), 404-410.

Jeyaseelan, C., Jain, A., Khurana, P., Kumar, D., Thatai, S. (2020). Ni-Cd Batteries. En: *Rechargeable Batteries: History, Progress, and Applications* (editado por R. Boddula, R. Pothu, Inamuddin, A. Asiri), Londres: Wiley Online Library.

Kaiser, M., Chou, S., Liu, H.-K., Dou, S.-X., Wang, C., Wang, J. (2017). Structure–property relationships of organic electrolytes and their effects on Li/S battery performance. *Adv Mat*, 29(48), 1700449.

Kamisan, A., Kudin, T., Kamisan, A., Omar, A., Taib, M., Hasan, O., Ali, A., Yahya, M. (2022). Recent advances on graphene-based materials as cathode materials in lithium-sulfur batteries. *Int J Hydrogen Energ*, 47(13), 8630-8657.

Kaya, C., He, J., Gu, X., Butler, E. (2002). Nanostructured ceramic powders by hydrothermal synthesis and their applications. *Micropor Mesopor Mat*, 54(1-2), 37-49.

Kedzierska-Sar, A., Falkowski, P., Smalc-Koziorowska, J., Gierlotka, S., Szafran, M. (2021). Al_2O_3–W nanocomposites obtained by colloidal processing and in situ synthesis of nano-metal particles. *J Eur Ceram Soc*, 41(6), 3527-3534.

Khan, A., Khan, A., Asiri, A., Ashraf, G., Alhogbia, B. (2017). Graphene oxide based metallic nanoparticles and their some biological and environmental application. *Curr Drug Metab*, 18(11), 1020-1029.

Kidalov, S., Shakhov, F. (2009). Thermal conductivity of diamond composites. *Materials*, 2(4), 2467-2495.

Kim, H., Krishna, T., Zeb, K., Rajangam, V., Gopi, C., Sambasivam, S., Raghavendra, K, Obaidat, I. (2020). A Comprehensive Review of Li-Ion Battery Materials and Their Recycling Techniques. *Electronics*, 9(7), 1161.

Kim, J., Byun, S., Chung, S., Kim, S. (2018). Preparation and capacitance properties of graphene based composite electrodes containing various inorganic metal oxides. *Carbon Lett*, 25(1), 14-24.

Kim, T., Song, W., Son, D.-Y., Ono, L., Qi, Y. (2019). Lithium-ion batteries: outlook on present, future, and hybridized technologies. *J Mater Chem*, 7, 2942-2964.

Kim, Y., Oh, N., Oh, S.-T., Moon, I.-H. (2001). Thermal conductivity of W–Cu composites at various temperatures. *Mater Lett*, 51(5), 420-424.

Knap, V., Stroe, D.-I., Swierczynski, M., Teodorescu, R., Schaltz, E. (2016). Investigation of the Self-Discharge Behavior of Lithium-Sulfur Batteries. *J Electrochem Soc*, 163(6), A911.

Ko, Y.-C., Hsu, C.-H., Lo, C.-A., Wu, C.-M., Yu, H.-L., Hsu, C.-H., Lin, H.-P., Mou, C.-Y., Wu, H.-L. (2022). Interconnected microporous and mesoporous carbon derived from pitch for lithium-sulfur batteries. *ACS Sustainable Chem Eng*, 10(14), 4462–4472.

Kulova, T., Fateev, V., Seregina, E., Grigoriev, A. (2020). A brief review of post-lithium-ion batteries. *Int J Electrochem Sci*, 15(8), 7242-7259.

Kulova, T., Nikolaev, I., Fateev, V., Aliyev, S. (2018). Electrochemical systems of energy acumulation. *Chemical Problems*, 1, 9-34.

Lee, J., Kang, J., Kim, S.-W., Halim, W., Frey, M., Joo, Y. (2018). Effective suppression of the polysulfide shuttle effect in lithium–sulfur batteries by implementing rGO–PEDOT: PSS-coated separators via air-controlled electrospray. *ACS Omega*, 3(12), 16465-16471.

Lee, K.-M., Oh, D.-K., Choi, W.-S., Weissgärber, T., Kieback, B. (2007). Thermomechanical properties of AlN-Cu composite materials prepared by solid state processing. *J Alloys Compd*, 434-435, 375–377.

Li, H., Chiang, M., Lee, C., Yang, W. (2010). Thermal performance of plate-fin vapor chamber heat sinks. *Int Commun Heat Mass Tran*, 37(7), 731-738.

Li, H., Wang, J., Zhang, Y., Wang, Y., Mentbayeva, A., Bakenov, Z. (2019). Synthesis of carbon coated Fe_3O_4 grown on graphene as effective sulfur-host materials for advanced lithium/sulfur battery. *J Power Sources*, 437, 226901.

Li, J., Wang, X., Qiao, Y., Zhang, Y., He, Z., Zhang, H. (2015). High thermal conductivity through interfacial layer optimization in diamond particles dispersed Zr-alloyed Cu matrix composites. *Scripta Mater*, 109, 72-5.

Li, J.-Y., Xu, Q., Li, G., Yin, Y.-X., Wan, L.-J., Guo, Y.-G. (2017). Research progress regarding Si-based anode materials towards practical application in high energy density Li-ion batteries. *Mater Chem Front*, 1, 1691-1708. https://doi.org/10.1039/C6QM00302H

Li, P., Kim, H., Myung, S.-T., & Sun, Y.-K. (2021). Diverting exploration of silicon anode into practical way: A review focused on silicon-graphite composite for lithium ion batteries. *Energy Storage Mater*, 35, 550. https://doi.org/10.1016/j.ensm.2020.11.028

Li, Z., Wu, G., Yang, Y., Wan, Z., Zeng, X., Yan, L., Wu, S., Ling, M., Liang, C., Hui, K.n., Lin, Z. (2022). An ion-conductive grafted polymeric binder with practical loading for silicon anode with high interfacial stability in lithium-ion batteries. *Adv Energy Mater*, 12(29), 2201197. https://doi.org/10.1002/aenm.202201197

Lin, Q., Dong, X., Wang, Y., Zheng, N., Zhao, Y., Xu, W., Ding, T. (2020). Molybdenum disulfide with enlarged interlayer spacing decorated on reduced graphene oxide for efficient electrocatalytic hydrogen evolution. *J Mater Sci*, 55, 6637-6647. https://doi.org/10.1007/s10853-020-04478-w

Liu, G., Zhang, Z., Tian, W., Chen, W., Xi, B., Li, H., Feng, J., Xiong, S. (2020). $Ni_{12}P_5$ nanoparticles bound on graphene sheets for advanced lithium–sulfur batteries. *Nanoscale*, 12, 10760-10770. https://doi.org/10.1039/C9NR10680D

Liu, M., Yang, Z., Sun, H., Lai, C., Zhao, X., Peng, H., Liu, T. (2016). A hybrid carbon aerogel with both aligned and interconnected pores as interlayer for high-performance lithium–sulfur batteries. *Nano Res*, 9, 3735–3746. https://doi.org/10.1007/s12274-016-1244-1

Liu, Y., Chatterjee, A., Rusch, P., Wu, C., Nan, P., Peng, M., Bettels, F., Li, T., Ma, C., Zhang, C., Ge, B., Bigall, N.C., Pfnür, H., Ding, F., Zhang, L. (2021). Monodisperse molybdenum nanoparticles as highly efficient electrocatalysis for Li-S batteries. *ACS Nano*, 15(9), 15047-15056. https://doi.org/10.1021/acsnano.1c05344

Liu, Y., Sun, W., Lan, X., Hu, R., Cui, J., Liu, J., Liu, J., Zhang, Y., Zhu, M. (2019). Adding metal carbides to suppress the crystalline $Li_{15}Si_4$ formation: a route toward cycling durable Si-based anodes for lithium-ion batteries. *ACS Appl Mater Interfaces*, 11(42), 38727-38736. https://doi.org/10.1021/acsami.9b13024

Malekpour, H., Chang, K.-H., Chen, J.-C., Lu, C.-Y., Nika, D., Novoselov, K., Balandin, A. (2014). Thermal conductivity of graphene laminate. *Nano Lett*, 14(9), 5155-5161. https://doi.org/10.1021/nl501996v

Mariani, N. (2014). Ph.D. Thesis. *Development of Novel, Advanced Molybdenum-based Composites for High Energy Physics Applications*. Milan Polytechnic.

Mateo-Mateo, D., Garcia-Mulero, A., Albero-Sancho, J., García Gómez, H. (2019). N-doped defective graphene decorated by strontium titanate as efficient photocatalyst for overall water splitting. *Appl Catal B-Environ*, 252, 111-119. https://doi.org/10.1016/j.apcatb.2019.04.011

Matthews, R. (1970). Ph.D. Thesis. *Deformation and Strengthening in Molybdenum Carbide-Natural Graphite Composite Materials*. University of Wales.

Moreno, R. (2017). *Institute of Ceramics and Glass, CSIC.* (J. T. Paper, Ed.) Recuperado el 13 de enero de 2023, de Better ceramics through colloid chemistry: https://digital.csic.es/bitstream/10261/218153/1/Moreno_Better_JECS_Trust_Award_Paper.pdf

Moyassari, E., Roth, T., Kücher, S., Chang, C.-C., Hou, S.-C., Spingler, F., Jossen, A. (2022). The role of silicon in silicon-graphite composite electrodes regarding specific capacity, cycle stability, and expansion. *J Electrochem Soc*, 169, 010504. https://doi.org/10.1149/1945-7111/ac4545

Müllen, K. (2013). Graphene as target for polymer synthesis. En *Hierarchical Macromolecular Structures: 60 Years after the Staudinger Nobel* (editado por Virgil Percec). Verlag: Springer. Páginas: 61-92 https://doi.org/10.1007/12_2013_239

Nazeer, F., Ma, Z., Gao, L., Wang, F., Khan, M., Malik, A. (2019). Thermal and mechanical properties of copper-graphite and copper-reduced graphene oxide composites. *Compos Part. B-Eng*, 163, 77-85. https://doi.org/10.1016/j.compositesb.2018.11.004

Niu, S., Zhang, S.-W., Shi, R., Wang, J., Wang, W., Chen, X., Zhang, Z., Miao, J., Amini, A., Zhao, Y., Cheng, C. (2020). Freestanding agaric-like molybdenum carbide/graphene/N-doped carbon foam as effective polysulfide anchor and catalyst for high performance lithium sulfur batteries. *Energy Storage Materials*, 33, 73-81. https://doi.org/10.1016/j.ensm.2020.05.033

Oddone, J., Boerner, B., Reich, S. (2017). Composites of aluminum alloy and magnesium alloy with graphite showing low thermal expansion and high specific thermal conductivity. *Sci Technol Adv Mater*, 18(1), 180-186. https://doi.org/10.1080/14686996.2017.1286222

Ortiz-Landeros, J., Gómez-Yáñez, C., López-Juárez, R., Dávalos-Velasco, I., Pfeiffer, H. (2012). Synthesis of advanced ceramics by hydrothermal crystallization and modified related methods. *J Adv Ceram*, 1, 204-220. https://doi.org/10.1007/s40145-012-0022-0

Pan, W., Cai, X., Yang, C., Zhou, L. (2021). Amorphous Si/TiC/Graphite composite fabricated by high-energy ball-milling as an anode for lithium-ion batteries. *J Electron Mater*, 50, 2584-2593. https://doi.org/10.1007/s11664-021-08767-1

Parr Instrument Company. (15 de agosto de 2019). Obtenido de What is Hydrothermal Synthesis?: https://www.parrinst.com/blog/2019/08/what-is-hydrothermal-synthesis/

Pero-Sanz, J., Fernández-González, D., Verdeja, L. (2019). *Structural Materials: Properties and Selection*. Cham: Springer. https://doi.org/10.1007/978-3-030-26161-0

Piñuela-Noval, J., Fernández-González, D., Brutti, S., Suárez, M., Mazzei, F., Navarra, M., Verdeja, L.F., Fernández, A., Agostini, M. (2023). Metal carbide additives in graphite-silicon composites for lithium-ion batteries. *ChemElectroChem*, 10(21), e202300339. https://doi.org/10.1002/celc.202300339

Piñuela-Noval, J., Fernández-González, D., Suárez, M., Díaz, L., Verdeja, L., Fernández, A. (2023). Characterization of graphite–chromium carbide composites manufactured by spark plasma sintering. *J Am Ceram Soc*, 106(9), 5157-5166. https://doi.org/10.1111/jace.19145

Piñuela-Noval, J., Fernández-González, D., Suárez, M., Gómez-Rodríguez, C., Fernández, A. (2023). Spark plasma sintering of graphite-chromium carbide composites: Influence of the sintering temperature and powder synthesis method. *Ceram Int*, 49(21), 33891-33900. https://doi.org/10.1016/j.ceramint.2023.08.083

Prakasam, M., Morvan, A., Azina, C., Constantin, L., Goglio, G., Largeteau, A., Bordère, S., Heintz, J.-M., Lu, Y., Silvain, J.-F. (2020). Ultra-low temperature fabrication of copper carbon fibre composites by hydrothermal sintering for heat sinks with enhanced thermal efficiency. *Comps Part A-Appl S*, 133, 105858. https://doi.org/10.1016/j.compositesa.2020.105858

Ramanan, A. (2019). Nobel Prize in Chamistry 2019. *Resonance Journal of Science Education*, 24(12), 1381-1395. https://www.ias.ac.in/article/fulltext/reso/024/12/1381-1395

Rattan, S. K., Goswamy, J. K. (2022). Gold nanoparticle decorated graphene for efficient sensing of NO_2 gas. *Sensors Int*, 3, 100147. https://doi.org/10.1016/j.sintl.2021.100147

Razzaq, A., Yao, Y., Shah, R., Qi, P., Miao, L., Chen, M., Zhao, X., Peng, Y., Deng, Z. (2019). High-performance lithium sulfur batteries enabled by a synergy between sulfur and carbon nanotubes. *Energy Storage Materials*, 16, 194-202. https://doi.org/10.1016/j.ensm.2018.05.006

Ren, W., Ma, W., Zhang, S., Tang, B. (2019). Recent advances in shuttle effect inhibition for lithium sulfur batteries. *Energy Storage Materials*, 23, 707-732. https://doi.org/10.1016/j.ensm.2019.02.022

Rho, H., Jang, Y., Bae, H., Cha, A.-N., Lee, S., Ha, J.-S. (2021). Fanless porous Graphene-copper composite heat sink for micro devices. *Sci Rep*, 11, 17607. https://doi.org/10.1038/s41598-021-97165-y

Rodner, M., Icardi, A., Kodu, M., Jaaniso, R., Schütze, A., Eriksson, J. (2020). Metal oxide nanolayer-decorated epitaxial graphene: A gas sensor study. *Nanomaterials-Basel*, 10(11), 2168. https://doi.org/10.3390/nano10112168

Ryu, H., Ahn, H., Kim, K., Ahn, J., Cho, K., Nam, T. (2006). Self-discharge characteristics of lithium/sulfur batteries using TEGDME liquid electrolyte. *Electrochim Acta*, 52(4), 1563-1566. https://doi.org/10.1016/j.electacta.2006.01.086

Schubert, T., Ciupinski, T., Morgiel, J., Weidmuller, H., Weissgarber, T., Kieback, B. (2007a). Advanced composite materials for heat sink applications. *EuroPM Toulousse France*, del 15 al 17 de Octubre de 2007, Paper No 587,

Schubert, T., Brendel, A., Schmid, K., Koeck, T., Ciupinski, L., Zielinski, W., Weibgärder, T., Kieback, B. (2007b). Interfacial design of Cu/SiC composites prepared by powder metallurgy for heat sink applications. *Compos Part A-Appl S*, 38(12), 2398–2403. https://doi.org/10.1016/j.compositesa.2007.08.012

Sengupta, R., Bhattacharya, M., Bandyopadhyay, S., Bhowmick, A. (2011). A review on the mechanical and electrical properties of graphite and modified graphite reinforced polymer composites. *Prog Polym Sci*, 36(5), 638-670. https://doi.org/10.1016/j.progpolymsci.2010.11.003

Shen, C., Xie, J., Zhang, M., Andrei, P., Hendrickson, M., Plichta, E., Zheng, J. (2019). Self-discharge behavior of lithium-sulfur batteries at different electrolyte/sulfur ratios. *J Electrochem Soc*, 166, A5287. https://doi.org/10.1149/2.0461903jes

Shen, X.-Y., He, X.-B., Ren, S.-B., Zhang, H.-M., Qu, X.-H. (2012). Effect of molybdenum as interfacial element on the thermal conductivity of diamond/Cu composites. *J Alloys Compd*, 529, 134-139. https://doi.org/10.1016/j.jallcom.2012.03.045

Song, W., Xie, J., Liu, S., Zheng, Y., Cao, G., Zhu, T., Zhao, X. (2012). Graphene decorated with ZnO nanocrystals with improved electrochemical properties prepared by a facile in situ hydrothermal route. *Int J Electrochem Sci*, 7(3), 2164-2174. https://doi.org/10.1016/S1452-3981(23)13870-3

Stuer, M., Paul, B., Zhao, Z. (2020). Spark Plasma Sintering of ceramics: from modeling to practice. *Ceramics*, 3(4), 476-493. https://doi.org/10.3390/ceramics3040039

Su, D., Zhou, D., Wang, C., Wang, G. (2018). Toward high performance lithium–sulfur batteries based on Li_2S cathodes and beyond: Status, challenges, and perspectives. *Adv Funct Mater*, 28(38), 1800154. https://doi.org/10.1002/adfm.201800154

Suárez, M., Fernández, A., Menéndez, J., Torrecillas, R., Kessel, H., Hennicke, J., Kirchner, R., Kessel, T. (2013). Challenges and Opportunities for Spark Plasma

Sintering: A Key Technology for a New Generation of Materials. En *Sintering Applications* (editado por Burcu Ertug), Londres: Intechopen. https://doi.org/10.5772/53706

Suárez, M., Fernández-González, D., Díaz, L., Borrell, A., Moya, J., Fernández, A. (2021). Synthesis and processing of improved graphite-molybdenum-titanium composites by colloidal route and spark plasma sintering. *Ceram Int*, 47(21), 30993-30998. https://doi.org/10.1016/j.ceramint.2021.07.267

Suárez, M., Fernández-González, D., Díaz, L., Piñuela-Noval, J., Borrell, A., Moya, J., Torrecillas, R., Fernández, A. (2023). Effect of Mo content on the properties of graphite–MoC composites sintered by spark plasma sintering. *Bol Soc Esp Ceram V*, 62(6), 588-596. https://doi.org/10.1016/j.bsecv.2023.02.005

Suárez, M., Fernández-González, D., Gutiérrez-González, C.F., Díaz, L.A., Borrell, A., Moya, J., Torrecillas, R., Fernández, A. (2022). Effect of green body density on the properties of graphite–molybdenum–titanium composite sintered by spark plasma sintering. *J Eur Ceram Soc*, 42(5), 2048-2052. https://doi.org/10.1016/j.jeurceramsoc.2021.12.073

Suchanek, W., Riman, R. (2006). Hydrothermal synthesis of advanced ceramic powders. *Adv Sci Tech*, 45, 184-193. https://doi.org/10.4028/www.scientific.net/AST.45.184

Sun, F., Wang, J., Chen, H., Li, W., Qiao, W., Long, D., Ling, L. (2013). High efficiency immobilization of sulfur on nitrogen-enriched mesoporous carbons for Li–S batteries. *ACS Appl Mater Interfaces*, 5(12), 5630-5638. https://doi.org/10.1021/am400958x

Sun, W., Hu, R., Liu, H., Zhang, H., Liu, J., Yang, L., Wang, H., Zhu, M. (2016). Silicon/Wolfram Carbide@Graphene composite: enhancing conductivity and structure stability in amorphous-silicon for high lithium storage performance. *Electrochim Acta*, 191, 462-472. https://doi.org/10.1016/j.electacta.2016.01.096

Sun, Z., Zhang, J., Yin, L., Hu, G., Fang, R., Cheng, H.-M., Li, F. (2017). Conductive porous vanadium nitride/graphene composite as chemical anchor of polysulfides for lithium-sulfur batteries. *Nat Commun*, 8, 14627. https://doi.org/10.1038/ncomms14627

Tarascon, J.-M., Armand, M. (2001). Issues and challenges facing rechargable lithium batteries. *Nature*, 414, 359-367. https://doi.org/10.1038/35104644

Taylor, G. (Febrero de 1933). *Apparatus for making hard metal compositions*, EEUU Patente nº US Patent No. 1896854.

Tian, Y., Zhao, Y., Zhang, Y., Ricardez-Sandoval, L., Wang, X., Li, J. (2019). Construction of oxygen-deficient $La(OH)_3$ nanorods wrapped by reduced graphene oxide for polysulfide trapping toward high-performance lithium/sulfur batteries. *ACS Appl Mater Interfaces*, 11(26), 23271–23279. https://doi.org/10.1021/acsami.9b06904

Velikov, K., Zegers, G., Van Blaaderen, A. (2003). Synthesis and characterization of large colloidal silver particles. *Langmuir*, 19(4), 1384–1389. https://doi.org/10.1021/la026610p

Venkatraman, M., Neumann, J. (1990). The C-Cr (carbon-chromium) system. *Bulletin of Alloy Phase Diagrams*, 11, 152-159. https://doi.org/10.1007/BF02841701

Vignesh Raj, S., Rajkumar, M., Meenakshi Sundaram, N., Kandaswamy, A. (2018). Synthesis and characterization of hydroxyapatite/alumina ceramic nanocomposites for biomedical applications. *Bull Mater Sci*, 41, 93. https://doi.org/10.1007/s12034-018-1612-4

Wagner, N., Tron, A., Tolchard, J., Noia, G., Bellman, M. (2019). Silicon anodes for lithium-ion batteries produced from recovered kerf powders. *J Power Sources*, 414, 486-494. https://doi.org/10.1016/j.jpowsour.2019.01.035

Wang, L., Li, J., Bai, G., Li, N., Wang, X., Zhang, H., Wang, J., Kim, M. (2019). Interfacial structure evolution and thermal conductivity of Cu-Zr/diamond composites prepared by gas pressure infiltration. *J Alloys Compd*, 781, 800-809. https://doi.org/10.1016/j.jallcom.2018.12.053

Wang, Z., Dong, Y., Li, H., Zhao, Z., Wu, H., Hao, C., Liu, S., Qiu, J., Lou, X. (2014). Enhancing lithium-sulphur battery performance by strongly binding the discharge products on amino-functionalized reduced graphene oxide. *Nat Commun*, 5, 50002. https://doi.org/10.1038/ncomms6002

White, J., Pontelandolfo, J. (1966). Graphite-carbide materials prepared by hot-working with a dispersed liquid-carbide phase. *Carbon*, 4(3), 305-306 (IN1-IN3, 307-314). https://doi.org/10.1016/0008-6223(66)90043-1

Winter, M., Barnett, B., Xu, K. (2018). Before li ion batteries. *Chem Rev*, 118(23), 11433–11456. https://doi.org/10.1021/acs.chemrev.8b00422

Wu, J., Zhang, Q., Li, M., Yan, J., Liu, J., Wu, Y. (2019). Nitrogen, sulfur-codoped micro-mesoporous carbon derived from boat-fruited sterculia seed for robust lithium–sulfur batteries. *RSC Adv*, 9, 15715-15726. https://doi.org/10.1039/C9RA02037C

Wu, R., Ma, L., Patil, A., Meng, Z., Liu, S., Hou, C., Zhang, Y., Yu, W., Guo, W., Liu, X. (2020). Graphene decorated carbonized cellulose fabric for physiological signal monitoring and energy harvesting. *J Mater Chem A*, 8, 12665-12673. https://doi.org/10.1039/D0TA02221G

Wypych, A. (2019). *Graphene. Important Results and Applications*, 1ª edición, Londres: ChemTec Publishing.

Xia, Y., Yin, Y. (2023). *Encyclopedia of Nanomaterials*. Londres: Elsevier.

Xiao, Z., Yang, Z., Zhang, L., Pan, H., Wang, R. (2017). Sandwich-type NbS_2@S@I-doped graphene for high-sulfur-loaded, ultrahigh-rate, and long-life Lithium–Sulfur batteries. *ACS Nano*, 11(8), 8488-8498. https://doi.org/10.1021/acsnano.7b04442

Xu, K., Li, X., Liu, X., Yu, Y., Zhang, X., Lei, W., Xie, Z., Zhang, S, Jia, Q., Zhang, H. (2023). In-situ synthesis of Si@G@TiC double protective layer structure for enhancing cycling stability of lithium-ion batteries. *Sustain Mater Technol*, 36, e00583. https://doi.org/10.1016/j.susmat.2023.e00583

Xu, Z. (2018). Fundamental properties of graphene. En: *Graphene: Fabrication, Characterizations, Properties and Applications* (editado por H. Zhu, Z. Xu, D. Xie, Y. Fang) London: Academic Press, páginas 73-102. https://doi.org/10.1016/B978-0-12-812651-6.00004-5

Yanagisawa, O., Hatayama, T., Matsugi, K. (1994). Recent research on spark sintering. *Mateira Japan*, 33(12), 1489-1496. https://doi.org/10.2320/materia.33.1489

Yang, G., Park, S.-J. (2019). Conventional and microwave hydrothermal synthesis and application of functional materials: A review. *Materials*, 12(7), 1177. https://doi.org/10.3390/ma12071177

Yang, L., Sun, L., Bai, W., Li, L. (2019). Thermal conductivity of Cu-Ti/diamond composites via spark plasma sintering. *Diamond Relat Mater*, 94, 37-42. https://doi.org/10.1016/j.diamond.2019.02.014

Yang, W., Zhou, L., Peng, K., Zhu, J., Wan, L. (2013). Effect of tungsten addition on thermal conductivity of graphite/copper composites. *Compos Part B: Eng*, 55, 1-4. https://doi.org/10.1016/j.compositesb.2013.05.023

Yoon, T., Nguyen, C., Seo, D., Lucht, B. (2015). Capacity fading mechanisms of silicon nanoparticle negative electrodes for lithium ion batteries. *J Electrochem Soc*, 162, A2325-A2330. https://doi.org/10.1149/2.0731512jes

Yoshida, K., Morigami, H. (2009). Thermal conductivity of diamond composites. *Materials*, 2(4), 2467-2495. https://doi.org/10.3390/ma2042467

Yuan, H., Zhang, W., Wang, J.-G., Zhou, G., Zhuang, Z., Luo, J., Huang, H., Gan, Y., Liang, C., Xia, Y., Zhang, J., Tao, X. (2018). Facilitation of sulfur evolution reaction by pyridinic nitrogen doped carbon nanoflakes for highly-stable lithium-sulfur batteries. *Energy Storage Materials*, 10, 1-9. https://doi.org/10.1016/j.ensm.2017.07.015

Zhang, Y., Gao, Z., Song, N., He, J., Li, X. (2018). Graphene and its derivatives in lithium–sulfur batteries. *Mater Today Energ*, 9, 319-335. https://doi.org/10.1016/j.mtener.2018.06.001

Zheng, M., Chi, Y., Hu, Q., Tang, H., Jiang, X., Zhang, L., Zhang, S., Pang, H., Xu, Q. (2019). Carbon nanotube-based materials for lithium–sulfur batteries. *J Mater Chem A*, 7, 17204-17241. https://doi.org/10.1039/C9TA05347F

Zhou, Y., Sun, H., Uddin, M., Barr, M., Wisser, D., Robmann, P., Esper, J.D., Tymek, S., Döhler, D., Peukert, W., Hartmann, M., Bachmann, J. (2021). *Electrochim. Acta*, 388, 138522. https://doi.org/10.1016/j.electacta.2021.138522

Zhu, K., Wang, C., Chi, Z., Ke, F., Yang, Y., Wang, A., Wang, W., Miao, L. (2019). How far away are lithium-sulfur batteries from commercialization? *Front Energy Res*, 7, 123. https://doi.org/10.3389/fenrg.2019.00123

7. Artículos publicados

A raíz de esta tesis doctoral se han publicado un total de 5 artículos indexados en el *Journal of Citations Reports*. Los artículos se referencian a continuación en los que los tres primeros forman parte del bloque de los materiales de matriz carbonosa para el campo de los disipadores de calor, y los dos últimos se corresponden al bloque de los materiales de matriz carbonosa para el campo de las baterías:

1. Marta Suárez, Daniel Fernández-González, Luis Antonio Díaz, **Juan Piñuela-Noval**, Amparo Borrell, José Serafín Moya, Ramón Torrecillas, Adolfo Fernández, 2023: Effect of Mo content on the properties of graphite–MoC composites sintered by spark plasma sintering, Boletín de la Sociedad Española de Cerámica y Vidrio, 62(6), 588-596, https://doi.org/10.1016/j.bsecv.2023.02.005
2. **Juan Piñuela-Noval**, Daniel Fernández-González, Marta Suárez, Luis Antonio Díaz, Luis Felipe Verdeja, Adolfo Fernández, 2023: Characterization of graphite–chromium carbide composites manufactured by spark plasma sintering, Journal of the American Ceramic Society, 106, 5157–5166. https://doi.org/10.1111/jace.19145
3. **Juan Piñuela-Noval**, Daniel Fernández-González, Marta Suárez, Cristian Gómez-Rodríguez, Adolfo Fernández, 2023: Spark plasma sintering of graphite-chromium carbide composites: Influence of the sintering temperature and powder synthesis method, Ceramics International, 49(21), 33891-33900, https://doi.org/10.1016/j.ceramint.2023.08.083
4. **Juan Piñuela-Noval**, Daniel Fernández-González, Sergio Brutti, Marta Suárez, Franco Mazzei, Maria Assunta Navarra, Luis Felipe Verdeja, Adolfo Fernández, Marco Agostini, 2023: Metal carbide additives in graphite-silicon composites for Lithium-Ion batteries, ChemElectroChem, 10, e202300339, https://doi.org/10.1002/celc.202300339
5. **Juan Piñuela-Noval**, Daniel Fernández-González, Marta Suárez, Luis Felipe Verdeja, Arcangelo Celeste, Adriano Pierini, Franco Mazzei, Maria Assunta Navarra, Sergio Brutti, Adolfo Fernández, Marco Agostini, 2024: Enhancement of Li/S battery performance by a modified reduced graphene oxide carbon host decorated with MoO_3, enviado.

Los artículos se han publicado en revistas indexadas en el Journal of Citations Reports. Por lo que respecta a los índices de calidad de las revistas en los que se han publicado los artículos, estos se recogen en la **Tabla 1** con los últimos datos disponibles (2022).

Tabla 1. Métricas de las revistas en las que se publicaron los trabajos que sustentan esta tesis doctoral.

Nombre de la revista	Categoría	Factor de impacto	Cuartil	Ranking
Boletín de la Sociedad Española de Cerámica y Vidrio	MATERIALS SCIENCE, CERAMICS	3.4	Q1	6/29
Journal of the American Ceramic Society	MATERIALS SCIENCE, CERAMICS	3.9	Q1	4/29
Ceramics International	MATERIALS SCIENCE, CERAMICS	5.2	Q1	3/29
ChemElectroChem	ELECTROCHEMISTRY	4.0	Q2	14/30

Asimismo, las investigaciones realizadas en la presente tesis doctoral han sido presentadas a congresos de índole nacional e internacional. Se detallan a continuación los trabajos presentados junto:

- Internacionales:
    - **Juan Piñuela-Noval**, Marco Agostini, Sergio Brutti, Adolfo Fernández, Daniel Fernández-González, Marta Suárez, Luis Felipe Verdeja: Synthesis of RGO-Mo and rGO-Mo_2C composites as active material to alleviate the shuttle effect of polysulphides in Li-S batteries, FEMS EUROMAT, del 3 al 7 de septiembre de 2023, Frankfurt, Alemania. (ORAL)
    - **Juan Piñuela-Noval**, Daniel Fernández-González, Marta Suárez, Cristian Gómez, Adofo Fernández: Graphite-Cr composites sintered by SPS technique: Influence of the temperature and powder processing method on

the properties, XVIIIth Conference of the European Ceramic Society, 2 al 6 de julio de 2023, Lyon, Francia. (ORAL)

- Nacionales:

    - **Juan Piñuela-Noval**, Daniel Fernández-González, Marco Agostini, Marta Suárez, Luis Felipe Verdeja, Maria Assunta Navarra, Adolfo Fernández, Sergio Brutti: Composite grafito–silicio en aplicaciones de gestión de energía, XV Congreso Nacional de Materiales Compuestos, del 13 al 15 de junio de 2023, Xixón/Gijón, Asturias, España. (ORAL)

    - Daniel Fernández-González, Marta Suárez, **Juan Piñuela-Noval**, Cristian Gómez, Luis Antonio Díaz, Adolfo Fernández: Composites de grafito con carburo de cromo con potencial aplicación en disipación de calor, XV Congreso Nacional de Materiales Compuestos, del 13 al 15 de junio de 2023, Xixón/Gijón, Asturias, España. (ORAL)
    - **Juan Piñuela-Noval**, Marta Suárez, Daniel Fernández-González Luis Antonio Díaz, Ramón Torrecillas, Luis Felipe Verdeja, Amparo Borrell, Adolfo Fernández: Composites grafito-metal para aplicaciones de gestión de energía, VIII Congreso de Sociedad Española de Cerámica y Vidrio, del 3 al 6 de mayo de 2022, Madrid, España. (ORAL)
    - **Juan Piñuela-Noval**, Daniel Fernández-González, Marta Suárez, Luis Felipe Verdeja, Adolfo Fernández: Materiales compuestos nanoestructurados cerámica-metal de interés tecnológico mediante Spark Plasma Sintering, II Congreso Anual Internacional de Estudiantes de Doctorado (CAIED), del 3 al 4 de febrero de 2022, Elche, España. (PÓSTER)

Artículo 1: Effect of Mo content on the properties of graphite–MoC composites sintered by spark plasma sintering.

BOLETÍN DE LA SOCIEDAD ESPAÑOLA DE CERÁMICA Y VIDRIO 62 (2023) 588–596

BOLETIN DE LA SOCIEDAD ESPAÑOLA DE
Cerámica y Vidrio
www.elsevier.es/bsecv

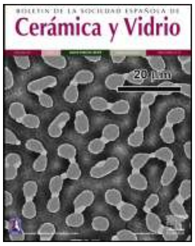

Effect of Mo content on the properties of graphite–MoC composites sintered by spark plasma sintering

Marta Suárez[a], *Daniel Fernández-González*[a,*], *Luis Antonio Díaz*[a], *Juan Piñuela-Noval*[a], *Amparo Borrell*[b], *José Serafín Moya*[a], *Ramón Torrecillas*[a], *Adolfo Fernández*[a]

[a] *Nanomaterials and Nanotechnology Research Center (CINN-CSIC), Universidad de Oviedo (UO), Principado de Asturias (PA), El Entrego, Spain*
[b] *Instituto de Tecnología de Materiales, Universitat Politècnica de València (UPV), Valencia, Spain*

ARTICLE INFO

Article history:
Received 15 July 2022
Accepted 20 February 2023
Available online 15 March 2023

Keywords:
Graphite
Spark plasma sintering
Thermal conductivity
Mechanical properties
Electrical conductivity

ABSTRACT

Graphite–molybdenum–titanium powders prepared by colloidal processing technique were sintered by Spark Plasma Sintering (SPS). This material is proposed in this manuscript due to its potential interest as heat sink. The influence of the molybdenum content (2.5, 5.0 and 10.0 vol.%) on the thermal, electrical, and mechanical properties of the composite are studied to define the composite with the best properties. Thermal, electrical, and mechanical properties of the composite graphite–10 vol.% Mo–1 vol.% Ti (that are composites of graphite with molybdenum and titanium carbides after sintering) are significantly better than those of the composites with lower molybdenum contents (2.5 vol.% and 5 vol.%). This way, flexural strength, electrical conductivity, and thermal conductivity are 1.5, 7.8 and 18 times greater, respectively, than in the composite graphite–2.5 vol.% Mo–1 vol.% Ti. In the case of comparing with the composite graphite–5 vol.% Mo–1 vol.% Ti, flexural strength, electrical conductivity, and thermal conductivity are 1.2, 5.1 and 3.2 greater in the composite graphite–10 vol.% Mo–1 vol.% Ti, respectively.

Influencia del contenido en Mo en las propiedades de materiales compuestos de grafito-MoC sinterizados por Spark Plasma Sintering

RESUMEN

Se sinterizaron por Spark Plasma Sintering (SPA) polvos de grafito-molibdeno-titanio preparados mediante la técnica de síntesis coloidal. En el presente manuscrito se propone este material debido a su potencial en disipadores de calor. Se estudió la influencia del contenido en molibdeno (2,5, 5,0 y 10,0 vol.%) en las propiedades térmicas, eléctricas y

Palabras clave:
Grafito
Spark plasma sintering
Conductividad térmica

---

* *Corresponding author.*
E-mail address: d.fernandez@cinn.es (D. Fernández-González).

https://doi.org/10.1016/j.bsecv.2023.02.005

Propiedades mecánicas
Conductividad eléctrica

mecánicas del material compuesto para definir aquel con las mejores propiedades. De este modo, las propiedades térmicas, eléctricas y mecánicas del material compuesto grafito-10 vol.% Mo-1 vol.% Ti (que son composites de grafito con carburos de titanio y molibdeno tras la sinterización) son significativamente mejores que aquellas de los materiales compuestos con menores contenidos en molibdeno (2,5 vol.% y 5 vol.%). Así pues, la resistencia a flexión, la conductividad eléctrica y la conductividad térmica son 1,5, 7,8 y 18 veces superiores, respectivamente, a las del composite grafito-2,5 vol. Mo-1 vol.% Ti. Si la comparación se lleva a cabo con el material compuesto grafito-5 vol.% Mo-1 vol.% Ti, la resistencia a flexión, la conductividad eléctrica y la conductividad térmica son 1,2, 5,1 y 3,2 veces superiores en el material compuesto grafito-10 vol. Mo-1 vol.% Ti, respectivamente.

Introduction

Graphite is a carbon allotrope characterized by the good thermal and electrical conductivities, which make it interesting for thermal management applications when it is adequately sintered. Nevertheless, thermal, electrical, and mechanical properties are sometimes poor for such applications and, metallic second phases are added to obtain graphite-metal composites with improved properties. These metallic second phases include molybdenum [1–4], aluminum [5–8], or copper [9–16]. Graphite-metal composites, and in particular graphite–molybdenum composites, have been subject of research for years [1]. Focusing on the case of graphite–molybdenum carbide composites, the interest mainly arises from the thermal-mechanical properties conferred by the molybdenum carbides (MoC and Mo_2C). Within this line, White and Pontelandolfo produced graphite–molybdenum carbide composites by liquid phase sintering at high temperatures under applied pressure [17–19]. In addition, Harada and Rubin [20] studied the formation of carbides in graphite–molybdenum composites by hot pressing of petroleum coke (used as graphite source) and metal or metal carbide mixtures (prepared by dry blending of powders) at high temperatures (2000 °C). The excellent thermal, electrical, and mechanical properties of this composite, even under extreme conditions, have made them to find application in rocket nozzles [21] and, more recently, in collimators of particle accelerators for the Large Hadron Collider at CERN (Conseil Européen pour la Recherche Nucléaire) [22–24]. Within this last application, several researchers have proposed different methods to obtain the graphite–molybdenum carbide composites:

- Mariani [22] was involved in the preparation of molybdenum carbide-graphite composites by rapid hot pressing (10 min) at high temperatures (1700 °C). The process required the application of constant pressure (45 MPa) under vacuum (10^{-4} mbar) and reducing atmosphere (97% N_2–3% H_2).
- Bertarelli and Bizarro [23] were also involved in the preparation of molybdenum carbide-ceramic composites by powder mixing, green compaction (10–20 MPa) and hot pressing at temperatures within 2500 and 2600 °C and pressures between 35 and 45 MPa.
- Guardia-Valenzuela and colleagues [24] prepared graphite–molybdenum carbide-titanium carbide composites from graphite, molybdenum (with a constant molybdenum content, 4.5 vol.%), titanium and, in some cases, carbon fibers. Powder mixture was prepared in a 3D mixing machine and, then powders were compacted by uniaxial hydraulic pressing at 300 MPa and sintered by spark plasma sintering at temperatures exceeding 2500 °C.

Graphite–molybdenum carbide composites have also potential application in the field of catalyzers for energy conversion devices. Within this line, Huang and colleagues synthesized graphite–Mo_2C nanocomposites by solid-state reaction from melamine and MoO_3 as precursors under inert atmosphere. Then, pressed pellets of precursors were treated in a tubular furnace under N_2 flow at 1400 °C for 3 h [25].

Finally, our research group has also been involved in the research within the topic of graphite–molybdenum carbide composites for thermal management applications. We have investigated the utilization of colloidal synthesis and spark plasma sintering in the consolidation of graphite–molybdenum carbide–titanium carbide composite [26], which resulted in improved properties (thermal, electrical, and mechanical) with respect to those of the composite obtained by attrition milling and spark plasma sintering. This research reported that sintering at significantly lower temperature (2000 °C) than that indicated in Valenzuela et al. [24] (2600 °C) and, therefore, without involving liquid phase [27], was possible. Despite all the existing research within this topic, studies about the influence of molybdenum content on the graphite–molybdenum carbide composites were not found in the state of the art. Thus, the aim of the present manuscript is to study the influence of the molybdenum content on the final properties of graphite–molybdenum carbide-titanium carbide composites prepared by colloidal route and sintered by spark plasma sintering.

Materials and methods

Graphite–molybdenum–titanium composite powders were prepared by colloidal processing route. Graphite powder (crystalline natural graphite, grade 93004, Asbury Carbons

Company, flake morphology, $d_{50} = 6.007\,\mu\text{m}$, BET: 17 m^2/g) was the matrix constituent of the composite and, molybdenum (V) chloride (Sigma–Aldrich, Spain) and titanium isopropoxide (ABCR, Spain) were the precursors of molybdenum and titanium, respectively, which were the disperse constituents.

Colloidal processing consisted in adding dropwise a solution of $MoCl_5$ and $Ti[OCH(CH_3)_2]_4$ in ethanol into the graphite dispersion also in ethanol. Then, the slurry was first heated under magnetic stirring at 70 °C to facilitate the dispersion of the constituents and, it was later dried in drying oven under air atmosphere at 120 °C for 24 h to start the nucleation of molybdenum and titanium and to evaporate the alcohol. Afterward, dried material was grounded, and the powder was sieved through <180 μm. Finally, powders were subjected to heat treatment at 450 °C for 2 h in air to eliminate chloride and isopropoxide traces and, powder was later sieved through <180 μm before being sintered in the spark plasma sintering apparatus.

Green compacts of 40 mm in diameter and 3 mm in height were first obtained by uniaxial pressing at 15 MPa. These green compacts were later sintered in spark plasma sintering equipment (FCT-HP D25/1) using a graphite mold of 40 mm in diameter. Sintering cycle consisted in heating at a rate of 25 °C min^{-1} up to 1500 °C and 10 °C min^{-1} to the final dwell temperature (2400 °C) under an applied pressure of 30 MPa during all sintering process and vacuum conditions (10^{-1} mbar). Dwell time was 15 min, and cooling was carried out inside of the SPS equipment. Temperature was controlled by an axial pyrometer focused on the upper graphite punch measuring the temperature above the sample center, as it is the usual practice in this equipment.

Three molybdenum contents were chosen to evaluate their influence on the thermal, electrical, and mechanical properties of the composite on five specimens of each composition: 2.5 vol.%, 5 vol.% and 10 vol.% Mo. Titanium content was 1 vol.% in all the samples to stabilize at room temperature the cubic MoC formed at high temperatures. These three molybdenum contents were chosen to study a great field of compositions and optimize the number of experiments.

Characterization techniques

Different techniques were employed to analyze the thermal, electrical, and mechanical properties as well as the microstructural characteristics of the composite. This way, the adequate distribution of the molybdenum and titanium nanoparticles chemically adhered to the graphite surface was corroborated by means of high-resolution transmission electron microscopy (HRTEM, JEOL JEM 2100F with an acceleration voltage of 200 kV and field emission gun). Powders of the composite were dispersed in ethanol and one droplet of dispersion was put on the carbon-copper grid for HRTEM observation.

The mineralogical phases of the powder and sintered samples were analyzed by X-ray diffraction (XRD) technique. A Philips X' Pert Pro X-ray diffractometer was used: Cu-Kα radiation (λ = 0.15406 nm) in the range from 5° to 70°, with step size of 0.030° and step time 0.5 s. Peak fitting of the crystalline phases was carried out using the diffraction pattern files of the JCPDS (International Center for Diffraction Data).

The densification rate (or relative density) of the sintered samples was calculated by the relation between the density value determined by Archimedes' method and the theoretical density obtained by helium pycnometer (AccuPyc 1330 V2.04N) on powdered samples (<63 μm) of the sintered composite.

The fracture surface of sintered samples was characterized by field emission scanning electron microscopy (FESEM, Quanta FEG 650, Thermo Fisher Scientific, USA) in the backscatter electron mode.

Thermal (specific heat, diffusivity, and conductivity), electrical (conductivity) and mechanical (Young's modulus and flexural strength) properties of the composite were determined on the sintered composites. All the properties were measured in the in-plane direction of samples, except thermal properties. These were measured in the through-plane direction and the value in the in-plane direction was indirectly calculated by means of the Wiedemann–Franz law with a modified Lorenz number [28–30], where a value of the electrical conductivity in the through-plane <0.1 MS/m (0.08 MS/m) was assumed [24,26,27]. The thickness of the samples (3 mm) does not allow measuring the other properties in the through-plane direction because this thickness was not sufficient to machine specimens. Anyway, properties are worse in through-plane direction because of graphite lamellae disposition on the specimen favorably oriented in the in-plane direction [24,26,27], as it was checked by scanning electron microscope.

Regarding mechanical properties, Young's modulus was measured using resonance frequency equipment (Grindosonic MK7, Belgium). The flexural strength of the sintered samples was determined by three-point bending tests [C1161 – 13. Standard Test Method for Flexural Strength of Advanced Ceramics at Ambient Temperature] in specimens of 3 mm × 4 mm × 40 mm using a universal mechanical testing machine (Shimadzu-series AGS-IX, Japan) with a 10 kN load cell at a crosshead speed of 0.5 mm min^{-1}. The flexural strength (σ) was calculated using Eq. 1:

$$\sigma = \frac{3FL}{2wt^2} \tag*{(Eq. (1)}$$

where F is the load (force) at the fracture point, L is the length of the support spam, w and t are the width and the thickness of the sample, respectively.

Electrical conductivity was determined on the sintered sample in the in-plane direction using Sigma Scope SMP350 from Helmut Fischer GMBH equipment. 10 measurements were made on each surface of the sintered sample and the mean value of the 20 measurements was considered as representative of the electrical conductivity of the composite.

Thermal conductivity is an indirect measurement calculated in the through-plane direction from the thermal diffusivity and the specific heat using Eq. 2:

$$\lambda = \alpha \cdot \rho \cdot c_p \tag*{(Eq. (2)}$$

where λ is the thermal conductivity (W/m K), α is the thermal diffusivity (mm^2/s), ρ is the density (g/cm^3) and c_p is the specific heat (J/g K). This way, thermal diffusivity was measured in the through-plane direction using LFA 457 MicroFlash Netzsch

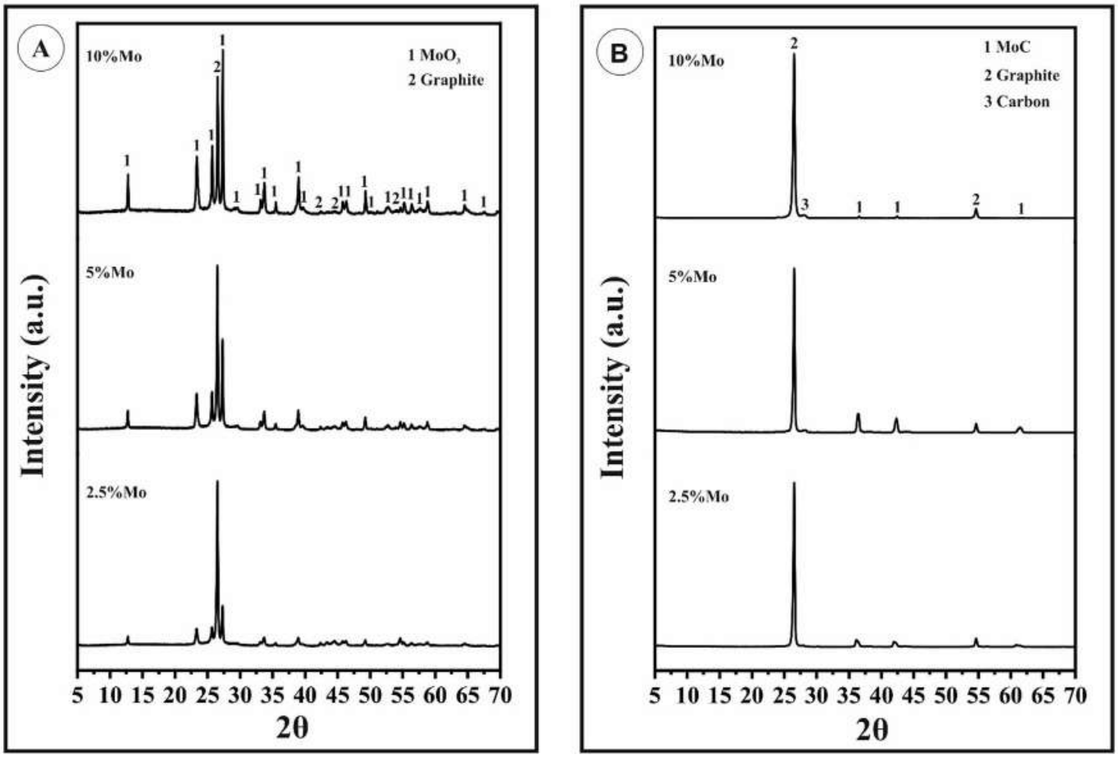

Fig. 1 – X-ray diffraction patterns of: (A) powders obtained after heat treatment at 450 °C for 2 h in air; (B) samples sintered in spark plasma sintering apparatus.

equipment, which is based on the flash method, on squared specimens of 10 mm × 10 mm × 3 mm. On the other hand, specific heat was determined using a C80 (Setaram Instrumentation) calorimeter, equipped with stainless steel cells (S60/1413). Measurements were made in continuous mode: heating ramp of 0.1 °C min^{-1} from 20 to 40 °C with 2 h of stabilization at the start and end temperatures. Data was processed with the Calisto Software. Thermal conductivity values in-plane were calculated using Eq. 3 considering the above-mentioned assumptions:

$$\frac{k}{\sigma} = LT \qquad \text{(Eq. (3)}$$

where k is the thermal conductivity, σ is the electrical conductivity, L is the modified Lorenz number and T is the temperature.

Results and discussion

Phase identification

Colloidal processing was employed, as mentioned, to obtain the composite because this technique ensures a more homogenous distribution of the second phases in the graphite matrix. The mixture of graphite with the precursors ($MoCl_5$ and $Ti[OCH(CH_3)_2]_4$) was first heated at 120 °C for 24 h to start the nucleation of molybdenum and titanium and to evaporate the alcohol, but chemical transformations were not experienced at this stage. Afterward, dried powders were subjected to heat treatment at 450 °C for 2 h in air to eliminate chloride and isopropoxide traces. This heat treatment involved the transformation of the precursors into oxides according to reactions 4 and 5 [31]:

$$MoCl_5(s) + 3/2O_2(g) = MoO_3(s) + 5/2Cl_2(g) \qquad \text{(Eq. (4)}$$

$$Ti(OCH(CH_3)_2)_4(s) = TiO_2(s) + 4C_3H_6(g) + 2H_2O(g) \qquad \text{(Eq. (5)}$$

The product of the chemical reaction (Eq. 4) was observed in X-ray diffraction analyses (that of titanium was not clearly observed due to both the quantity of titanium, but it formed during the sintering a complex carbide phase with the molybdenum, $(Ti_{1-x},Mo_x)_{1-y}C_y$, which stabilized the cubic molybdenum carbide phase) see Fig. 1a. Peaks corresponding to molybdenum oxide (VI) (JCPDS: 01-089-7112) increase in intensity as the molybdenum content grows.

After reactive sintering, where oxides of molybdenum and titanium were reduced in the SPS machine, and transformed into carbides, independent of the molybdenum content, graphite (JCPDS: 00-056-0159) and MoC JCPDS: 01-089-2868) are the main mineralogical phases (see Fig. 1b, corresponding to the sintered composites). MoC has cubic structure (a = 4.27 Å), which corresponds to the carbide of molybdenum that, according to the Mo-C binary phase diagram, is formed at high temperature (which is stable at room temperature due to the presence of titanium, as it was already reported). Carbon donates electrons to the metal atoms and the coordination of metal atoms changes to form the carbide structures. The stability of this carbide structure is promoted by the

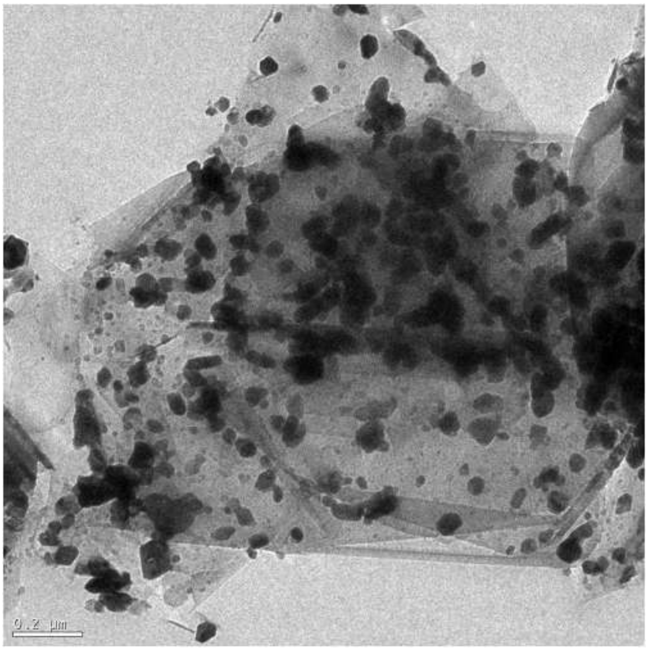

Fig. 2 – HRTEM image of graphite–molybdenum composite synthesized by colloidal route (sample graphite–5 vol.% Mo in the image).

covalent nature of the metal–carbon bond. The formation of the MoC starts at low temperature with the reaction of the molybdenum and graphite to form hexagonal or orthorhombic Mo_2C. The process continues with the diffusion of carbon inside Mo_2C to finally generate MoC. The stabilization of the α-MoC_{1-x} at room temperature is promoted by small additions of titanium. Otherwise, this phase (cubic) results only stable at temperatures above 1960 °C according to the Mo-C binary phase diagram. Molybdenum carbides and, in particular MoC, are beneficial for the mechanical properties of the composite and the suitable distribution of carbides within the graphite matrix has also a great influence on them. Nevertheless, MoC at grain boundaries or in acicular form are detrimental for the strength of the composite [23,26,27].

Microstructural characterization

Fig. 2 shows a HRTEM image of the composite, graphite in light gray color and MoC in black color, with a globular shape and a particle size around 10–100 nm, appears adequately distributed in the graphite matrix constituent because of the colloidal processing technique. There is chemical affinity between molybdenum and graphite [23], which can be also deduced from the X-ray diffraction analyses. Thus, hexagonal Mo_2C will appear above 1000 °C as a consequence of the carbon atoms diffusion inside of the molybdenum bcc lattice interstitials. This results in the formation of hexagonal Mo_2C when the amount of carbon reaches 33 at.%. Diffusion of carbon inside Mo_2C continues and MoC is formed, which justifies the identification of MoC in the samples, as it was already pointed out.

Diffusion processes have relevant importance in the formation of carbides. Thus, carbon is a relatively small atom that can rapidly displace throughout metal carbide lattices via interstitial vacancies [32]. On the other hand, the opposite mechanism, displacement of metal atoms in graphitic materials, is comparatively slow and difficult [27].

Field Emission Scanning Electron Microscopy (FESEM) was employed to study the microstructure of the fracture surface of the sintered samples. Fig. 3 shows the microstructures of the sintered composites of graphite with 2.5 vol.%, 5 vol.% and 10 vol.% Mo (and 1 vol.% Ti). Several conclusions can be deduced from these figures. It is possible to see in all the cases that the second phase is homogeneously distributed in the matrix of graphite, which has later influence in the properties of the composite. For the greatest contents in molybdenum (10 vol.% Mo), the size of this phase, which sintered appears as MoC, ranges from hundreds of nanometers to several microns due to the agglomeration of the particles related to the Mo content. In the case of composites with 2.5 vol.% and 5 vol.% Mo, the size of the second phases does not exceed 1 μm.

Images of the surface of fracture were taken from samples broken by three-point bending test. Fig. 4 corresponds to the sample graphite–10 vol.% Mo–1 vol.% Ti. It is possible to see that graphite lamellae appear oriented perpendicular to the pressing direction, which confirms the anisotropic behavior of the composite. This results in better properties in the in-plane direction than in the through-plane direction, as it is going to be later demonstrated. This anisotropic behavior is a potential advantage in the directional dissipation of heat.

Density

Natural graphite powders are characterized by exhibiting self-lubricating properties that make possible to obtain green samples with high densification (≃85%) using very low values of pressure, as high pressures involve risks of delamination of the green compacts. Anyway, the values of densification are far from those of other common ceramic materials, as silicon

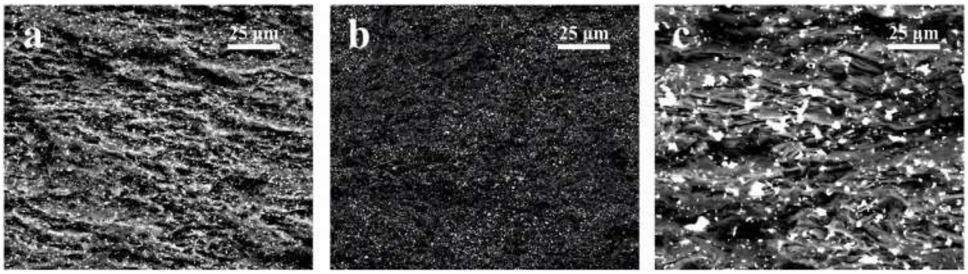

Fig. 3 – FESEM images of doped graphite with (a) 2.5 vol.% Mo, (b) 5 vol.% Mo and (c) 10 vol.% Mo

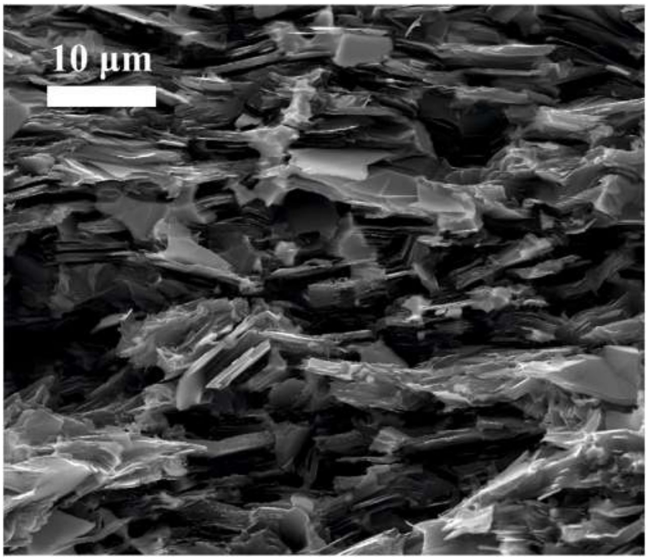

Fig. 4 – SEM image corresponding to the surface of fracture of the sample graphite–10 vol.% Mo–1 vol.% Ti.

carbide or alumina refractories, which even approach the theoretical density. In the case of graphite materials, according to Aguiar et al. [33], it is difficult to obtain densification rates >85% for non-conventional shapes, because of the high pressures required to obtain near-net shapes. In any case, values of densification do not exceed 95% even when greater pressures (to obtain green compacts) are used in other research works as in Suárez and coauthors [27]. In the case of the samples of this manuscript, the pressure applied to obtain green compacts was 15 MPa (uniaxial pressing) and values of densification rate are comparable for the three compositions (≃85%). This value of applied uniaxial pressure is 20 times smaller than that used by Guardia-Valenzuela and collaborators [24] and 3 times smaller than that employed by Suárez and colleagues [27]. Temperature is also important in the densification of the composite. The temperature at the dwell time was 2400 °C in this research, which is 200 °C lower than in the case of Guardia-Valenzuela et al. [24] and 400 °C greater than in the case of Suárez et al. [27]. In this second case, the higher temperature compensates at a certain extent the effect of the pressure applied to obtain the green compacts. Thus, these values of densification, see Table 1, are obtained, in general, without presence of liquid phase. Within this context, titanium melts at 1668 °C, which gives as result a small fraction of transitory liquid that will immediately react with the carbon to form a titanium–molybdenum complex carbide. Moreover, a eutectic point at 2200 °C for ∼3 wt. % carbon is found in the Mo-C binary phase diagram, which might locally have resulted in liquid phase at the sintering temperatures in zones locally enriched in molybdenum. Undoubtedly, this small fraction of liquid phase might have promoted the transport of mass and, therefore, the sintering of the composite.

Mechanical characterization

The Young's modulus and the flexural strength have been evaluated and the results can be found in Tables 2 and 3, respectively. The properties of molybdenum carbide-doped graphite show a clear anisotropic behavior since the properties depend on the orientation of the graphite flakes (see Fig. 4). Stronger interatomic bond appears in the perpendicular direction to the applied pressure. The presence of MoC nanoparticles, finely and homogeneously distributed, together with the strong carbide-graphite bond in samples obtained by colloidal route allows obtaining better mechanical properties in these composites than in the case of those obtained by simply mixing of powders [26].

Electrical conductivity

Electrical conductivity measurements on sintered samples are shown in Table 4. It is possible to see that increasing the molybdenum content represents a clear improvement of the electrical conductivity of the samples, particularly when the molybdenum content is as high as 10 vol.%. Therefore, electrical conductivity for this composite is 7.8 and 5.1 times greater than in the cases of 2.5 vol.% Mo and 5.0 vol.% Mo, respectively. This value is higher than that measured by Guardia-Valenzuela and colleagues [24] and Suárez and co-researchers [26,27] for composites of the graphite–molybdenum–titanium system with less molybdenum content.

Thermal conductivity

Values of the thermal conductivity in the graphite – molybdenum – titanium composite are shown in Table 5. These follow a similar trend to that of the electric conductivity, being higher in the in-plane than in the through-plane direction, with the greatest values for the composite with 10 vol.% Mo. This result, which is the same that in the case of the other properties, indicates that sintering graphite–molybdenum carbide–titanium carbide composites at temperatures significantly lower (2400 °C) than those proposed by Guardia-Valenzuela et al. [24] (2600 °C) is possible, as it was suggested by Suárez et al.

Table 1 – Density of SPS sintered samples at 2400 °C for different molybdenum contents.

Mo content (vol.%)	2.5	5.0	10.0
Green density (g/cm^3)	2.08 ± 0.02	2.33 ± 0.03	2.50 ± 0.02
SPS sample density (%)	82.32	86.05	85.24

Table 2 – Young's modulus of SPS sintered samples at 2400 °C for different molybdenum contents (in-plane).

Mo content (vol.%)	2.5	5.0	10.0
Young's modulus (GPa)	113.93 ± 22.29	203.59 ± 32.87	224.19 ± 65.93

Table 3 – Flexural strength of SPS sintered samples at 2400 °C for different molybdenum contents (in-plane).

Mo content (vol.%)	2.5	5.0	10.0
Flexural strength (MPa)	36.13 ± 7.98	44.90 ± 3.56	53.45 ± 8.27

Table 4 – Electrical conductivity of SPS sintered samples at 2400 °C for different molybdenum contents (in-plane).

Mo content (vol.%)	2.5	5.0	10.0
Electrical conductivity (MS/m)	0.14 ± 0.02	0.21 ± 0.03	1.07 ± 0.04

Table 5 – Thermal conductivity of SPS sintered samples at 2400 °C for different molybdenum contents.

Mo content (vol.%)	2.5	5.0	10.0
Thermal conductivity (W/m °C) (through-plane)	10.26 ± 1.33	30.65 ± 3.54	19.04 ± 1.45
Thermal conductivity (W/m °C) (in-plane)	14.17 ± 2.25	79.76 ± 6.20	255.35 ± 44.01

Table 6 – Relative values of the properties of the composites sintered at 2400 °C for different molybdenum contents (this indicates the number of times the parameter is greater in the case of the samples with 10 vol.% Mo).

Mo content (vol.%)	2.5	5.0
Flexural strength (MPa)	1.5	1.2
Electrical conductivity (MS/m)	7.8	5.1
Thermal conductivity (W/m °C)	18.0	3.2

[26,27] Values of thermal conductivity obtained for 10 vol.% Mo are, comparatively with those indicated in Guardia-Valenzuela et al. [24], lower but sufficient for not as extremely demanding applications as colliders but for less demanding applications of light heat dissipation devices. These last devices habitually demand excellent thermal conductivity, lightness, thermal resistance, or machinability, among other properties, and aluminum or copper are typically used in this application. However, graphite–molybdenum composites are, comparatively with the copper and aluminum, lighter (<2.50 g/cm^3 of graphite–Mo–Ti composite, in front of the 2.7 g/cm^3 of the aluminum or 8.96 g/cm^3 of the copper), with comparable thermal conductivity (>255 W/m K of graphite–Mo–Ti composite, in front of the 220 W/m K of the aluminum or 400 W/m K of the copper), better machinability or resistance at higher temperatures. Within this line, using hard sintering conditions as high temperatures (exceeding 2600 °C as in Guardia-Valenzuela et al. [24]) or pressures (300 MPa as in Guardia-Valenzuela et al. [24]) involve more expensive equipment and greater consumption of energy resources, resulting in more expensive components.

Discussion

Graphite–molybdenum–titanium composites were prepared by colloidal synthesis and sintered by Spark Plasma Sintering (SPS). It was possible to check that increasing the molybdenum content has had a noticeable influence on the properties of the composite (Table 6).

It is particularly relevant the influence of the molybdenum content on the electrical conductivity (and therefore on the thermal conductivity, since both parameters are related by the modified Wiedemann–Franz law). It is possible to see that increasing the metallic content, apart from improving the mechanical properties of the composite, results in greater conductivities. Typical value of electrical conductivity of graphite in the basal plane is 3–5 × 10^5 S/m (special quality graphite can reach values of electrical conductivity as high as 2.4 MS/m, for example, the thermal pyrolytic graphite [24]). On the other hand, some metal carbides show electrical conductivities as that of the metal [34]. This question, apart from the fact that some metal carbides inhibit basal planes slip through a pinning effect, which improves mechanical properties, makes reactive metals (carbides) interesting to improve the thermal–electrical properties of graphite. Within this context, metallic molybdenum shows values of electrical conductivity as high as 20 MS/m, and high thermal conductivity too (around 140 W/m K). These high values result in the great values of electrical and thermal conductivities of the composite, when sintered together graphite and molybdenum (transformed into carbide during the sintering), which makes it interesting for thermal management applications.

Molybdenum carbide should be adequately distributed within the graphite matrix. With this regard, Suárez et al. [26] have already demonstrated the influence of the colloidal processing technique on the properties of graphite–molybdenum–titanium composite. Colloidal processing is a suitable manner to obtain better mechanical properties than in the simple mechanic mixing of the constituents, precisely due to the more homogeneous distribution of the second phase [26]. However, if the influence of the molybdenum content is added, it is possible to see that values of electrical and thermal conductivities further improve. In the case of the first property, it is close to 1.1 MS/m in the in-plane direction (for 10 vol.% Mo), which is similar to that obtained by Guardia-Valenzuela et al. [24] (for 4.5 vol.% Mo), although using a SPS temperature 200 °C lower in the research presented in this manuscript. Additionally, the value of pressure required to obtain the green compacts is significantly lower, 15 MPa, which is 20 times lower than that used by Guardia-Valenzuela et al. [24] (300 MPa). The temperature compensates the influence of the pressure required to obtain the green compacts in terms of improvement of the properties. This way, better properties than in Suárez et al. [27], where the best were obtained for 60 MPa of uniaxial pressure to obtain green compacts (and SPS temperature at dwell time of 2000 °C), are obtained when using pressure of 15 MPa to obtain the green compacts if the temperature is increased up to 2400 °C. Thus, electrical conductivity is a 25% greater.

If the electrical conductivity is considered (and, therefore, the thermal conductivity), the composites obtained by colloidal synthesis and spark plasma sintering could be competitive in heat dissipation applications. They are, probably, not competitive with those proposed by Guardia-Valenzuela et al. [24] for extreme conditions applications of the Large Hadron Collider at CERN installations, but they might be applied in less demanding applications, i.e. heat dissipation, as it was already reported. In the case indicated in the manuscript, the temperature is 200 °C lower and the pressure required to obtain the green compacts is 20 times lower. Therefore, composites might be easily scaled up and used in less demanding thermal management applications.

Conclusions

Graphite–molybdenum carbide–titanium carbide composites were manufactured by spark plasma sintering from powders prepared by colloidal route. The influence of the molybdenum content (2.5, 5.0 and 10.0 vol.%) was studied on green compacts at 2400 °C. Molybdenum content has a significant influence on the electrical and thermal properties, as well as on mechanical properties. This way, the composite with 10.0 vol.% Mo content exhibits mechanical, electrical, and thermal properties 1.5, 7.8 and 18 times greater than those of the composite with 2.5 vol.% Mo and, 1.2, 5.1 and 3.2 times greater than those of the composite with 5.0 vol.% Mo. Within this context, it is possible to obtain graphite–10 vol.% Mo composites, using pressures to obtain green compacts 20 times lower than other researchers and sintering temperatures 200 °C lower. Therefore, graphite–molybdenum carbide–titanium carbide composites might be produced under less severe conditions of processing to be used in thermal management applications.

Authors' contribution

Conceptualization: A. Fernández, R. Torrecillas; **Data curation:** Marta Suárez, Daniel Fernández-González, Juan Piñuela-Noval; **Formal analysis:** Marta Suárez, Daniel Fernández-González, Juan Piñuela-Noval, José Serafín Moya; **Funding acquisition:** A. Fernández, R. Torrecillas, Daniel Fernández-González, Juan Piñuela-Noval; **Investigation:** Marta Suárez, Daniel Fernández-González, Juan Piñuela-Noval, Luis Antonio Díaz, Amparo Borrell; **Methodology:** Marta Suárez, Daniel Fernández-González, Juan Piñuela-Noval; **Project administration:** A. Fernández, R. Torrecillas; **Resources:** Marta Suárez, Daniel Fernández-González; **Supervision:** A. Fernández, R. Torrecillas; **Validation:** Marta Suárez, Daniel Fernández-González, Juan Piñuela-Noval; **Visualization:** Marta Suárez, Luis Antonio Díaz, Amparo Borrell; **Roles/Writing – original draft:** Marta Suárez, Daniel Fernández-González; **Writing – review & editing:** Marta Suárez, Daniel Fernández-González, Juan Piñuela-Noval, José Serafín Moya.

Acknowledgements

This research was funded by the Spanish Ministry of Science and Innovation. Call Programa Estatal de I+D+i Orientada a los Retos de la Sociedad (RTI2018-102269-BI00).

Daniel Fernández-González acknowledges the grant (Juan de la Cierva-Formación program) FJC2019-041139-I funded by MCIN/AEI/ 10.13039/501100011033 (Ministerio de Ciencia e Innovación, Agencia Estatal de Investigación).

Amparo Borrell acknowledges for her RYC-2016-20915.

Juan Piñuela Noval acknowledges the Programa "Severo Ochoa" of Grants for Research and Teaching of the Principality of Asturias for the funds received for the elaboration of the Ph.D. Thesis (Ref: BP20 041).

Authors are grateful to Ainhoa Macías San Miguel from Nanomaterials and Nanotechnology Research Center (CINN) for providing excellent technical assistance.

REFERENCES

[1] M. Humenik, D.W. Hall, R.V. Alsten, Graphite-base cermets: a new material for bearing, electrical and high-temperature applications, Met. Progr. 81 (1962) 101–108.

[2] J. White, R. Price, Hot-working of graphite for graphite-matrix nuclear fuels, Carbon 2 (1965) 327–330, http://dx.doi.org/10.1016/0008-6223(65)90001-1.

[3] R. Staffler, G. Kneringer, E. Kny, N. Reheis, Metal/graphite-composites in fusion engineering, in: IEEE Thirteenth Symposium on Fusion Engineering, Knoxville, TN, USA, 1989, pp. 955–958.

[4] D. John, G.M. Jenkins, Hot-working and strengthening in metal carbide-graphite composites, J. Mater. Sci. 21 (1986) 2941–2958, http://dx.doi.org/10.1007/BF00551515.

[5] T. Etter, J. Kuebler, T. Frey, P. Schulz, J.F. Löffler, P.J. Uggowitzer, Strength and fracture toughness of interpenetrating graphite/aluminium composites produced by the indirect squeeze casting process, Mater. Sci. Eng. A 386 (2004) 61–67, http://dx.doi.org/10.1016/j.msea.2004.06.066.

[6] J.K. Chen, I.S. Huang, Thermal properties of aluminum–graphite composites by powder metallurgy, Compos, Part B-Eng. 44 (2013) 698–703, http://dx.doi.org/10.1016/j.compositesb.2012.01.083.

[7] T. Etter, P. Schulz, M. Weber, J. Metz, M. Wimmler, J.F. Löffler, P.J. Uggowitzer, Aluminium carbide formation in interpenetrating graphite/aluminium composites, Mater. Sci. Eng. A 448 (2007) 1–6, http://dx.doi.org/10.1016/j.msea.2006.11.088.

[8] V. Oddone, B. Boerner, S. Reich, Composites of aluminum alloy and magnesium alloy with graphite showing low thermal expansion and high specific thermal conductivity, Sci. Technol. Adv. Mat. 18 (2017) 180–186, http://dx.doi.org/10.1080/14686996.2017.1286222.

[9] M. Byun, D. Kim, K. Sung, J. Jung, Y.S. Song, S. Park, I. Son, Characterization of copper–graphite composites fabricated via electrochemical deposition and spark plasma sintering, Appl. Sci.-Basel 9 (2019) 2853, http://dx.doi.org/10.3390/app9142853.

[10] M.M. Dewidar, J.K. Lim, Manufacturing processes and properties of copper—graphite composites produced by high frequency induction heating sintering, J. Compos. Mater. 41 (2007) 2183–2194, http://dx.doi.org/10.1177/0021998307074145.

[11] J. Kovacik, S. Emmer, Cross property connection between the electric and the thermal conductivities of copper graphite composites, Int. J. Eng. Sci. 144 (2019) 103130, http://dx.doi.org/10.1016/j.ijengsci.2019.103130.

[12] J. Liu, K. Sun, L. Zeng, J. Wang, X.P. Xiao, J. Liu, C.J. Guo, Y. Ding, Microstructure and properties of copper–graphite composites fabricated by spark plasma sintering based on two-step mixing, Metals 10 (2020) 1506, http://dx.doi.org/10.3390/met10111506.

[13] A. Mazloum, J. Kovacik, S. Emmer, I. Sevostianov, Copper–graphite composites: thermal expansion, thermal and electrical conductivities, and cross-property connections, J. Mater. Sci. 51 (2016) 7977–7990.

[14] A. Mazloum, J. Kovacik, A. Zagrai, I. Sevostianov, Copper-graphite composite: shear modulus, electrical resistivity, and cross-property connections, Int. J. Eng. Sci. 149 (2020) 103232, http://dx.doi.org/10.1007/s10853-016-0067-5.

[15] F. Nazeer, Z. Ma, L. Gao, F. Wang, M.A. Khan, A. Malik, Thermal and mechanical properties of copper-graphite and copper-reduced graphene oxide composites, Compos. Part B-Eng. 163 (2019) 77–85, http://dx.doi.org/10.1016/j.compositesb.2018.11.004.

[16] Z. Xiao, R. Chen, X. Zhu, Z. Li, G. Xu, Y. Jia, Y. Zhang, Microstructure, and physical and mechanical properties of copper–graphite composites obtained by in situ reaction method, J. Mater. Eng. Perform. 29 (2020) 1696–1705, http://dx.doi.org/10.1007/s11665-020-04646-8.

[17] J. White, J. Pontelandolfo, Graphite–carbide materials prepared by hot-working with the carbide phase in the liquid state, Nature 209 (1966) 1018–1019, http://dx.doi.org/10.1038/2091018a0.

[18] J. White, J. Pontelandolfo, Graphite–carbide materials prepared by hot-working with a dispersed liquid-carbide phase, Carbon 4 (1966) 305–314, http://dx.doi.org/10.1016/0008-6223(66)90043-1.

[19] J. White, J. Pontelandolfo, HWLC graphites prepared by hot-working extruded stock, Carbon 6 (1968) 1–2, http://dx.doi.org/10.1016/0008-6223(68)90043-2.

[20] Y. Harada, G.A. Rubin, Fabrication and characterization of metal carbide-graphite composites, in: Presented at the 68th Annual Meeting of The American Ceramic Society, May 9, Washington, D.C., 1966.

[21] R. Matthews, Deformation and Strengthening in Molybdenum Carbide – Natural Graphite Composite Materials (Ph.D. thesis), University of Wales, 1970.

[22] N. Mariani, Development of Novel, Advanced Molybdenum-based Composites for High Energy Physics Applications (Ph.D. Thesis), Milan Polytechnic, 2014.

[23] A. Bertarelli, S. Bizzaro, A molybdenum carbide/carbon composite and manufacturing method, Int. Pat. Appl. (2016), PCT/EP2013/072818.

[24] J. Guardia-Valenzuela, A. Bertarelli, F. Carra, N. Mariani, S. Bizzaro, R. Arenal, Development and properties of high thermal conductivity molybdenum carbide – graphite composites, Carbon 135 (2018) 72–84, http://dx.doi.org/10.1016/j.carbon.2018.04.010.

[25] K. Huang, K.C. Bi, C.S. Liang, S. Lin, W.J. Wang, T.Z. Yang, J. Liu, R. Zhang, D.Y. Fan, WangYG, M. Lei, Graphite carbon-supported Mo_2C nanocomposites by a single-step solid state reaction for electrochemical oxygen reduction, PLOS ONE 18 (2015) 1–11, http://dx.doi.org/10.1371/journal.pone.0138330.

[26] M. Suárez, D. Fernández-González, L.A. Díaz, A. Borrell, J.S. Moya, A. Fernández, Synthesis and processing of improved graphite–molybdenum–titanium composites by coloidal route and spark plasma sintering, Ceram. Int. 47 (2021) 30993–30998, http://dx.doi.org/10.1016/j.ceramint.2021.07.267.

[27] M. Suárez, D. Fernández-González, D.F. Gutiérrez-González, L.A. Diaz, A. Borrell, J.S. Moya, R. Torrecillas, A. Fernández, Effect of green body density on the properties of graphite–molybdenum–titanium composite sintered by spark plasma sintering, J. Eur. Ceram. Soc. 42 (2022) 2048–2052, http://dx.doi.org/10.1016/j.jeurceramsoc.2021.12.073.

[28] B. Schultrich, W. Poeβnecker, Thermal conductivity of cemented carbides, J. Therm. Anal. 33 (1988) 305–310, http://dx.doi.org/10.1007/bf01914616.

[29] R.W. Powell, F.H. Schofield, The thermal and electrical conductivities of carbon and graphite to high temperatures, Proc. Phys. Soc. 51 (1939) 153–172, http://dx.doi.org/10.1088/0959-5309/51/1/317.

[30] J. Kováčik, S. Emmer, J. Bielek, Cross-property connections for copper–graphite composites, Acta Mech. 227 (2016) 105–112, http://dx.doi.org/10.1007/s00707-015-1411-6.

[31] P. Buerger, D. Nurkowski, J. Akroyda, M. Kraft, A kinetic mechanism for the thermal decomposition of titanium tetraisopropoxide, Proc. Combust. Inst. 36 (2017) 1019–1027, http://dx.doi.org/10.1016/j.proci.2016.08.062.

[32] R.B. Matthews, G.M. Jenkins, The high temperature interaction between molybdenum and graphite, J. Mater. Sci. 10 (1975) 1976–1990, http://dx.doi.org/10.1007/BF00754489.

[33] J.A. Aguiar, S. Kwon, B.D. Coryell, E. Eyerman, A.A. Bokov, R.H.R. Castro, D. Burns, H.T. Hartmann, E.P. Luther, Densification of graphite under high pressure and moderate temperature, Mater. Today Commun. 22 (2020) 100821, http://dx.doi.org/10.1016/j.mtcomm.2019.100821.

[34] E. Parthe, V. Sadagopan, The structure of dimolybdenum carbide by neutron diffraction technique, Acta Crystallogr. 16 (1963) 202–205, http://dx.doi.org/10.1107/S0365110X63000487.

Artículo 2: Characterization of graphite–chromium carbide composites manufactured by spark plasma sintering.

Received: 8 December 2022 | Revised: 10 March 2023 | Accepted: 22 March 2023

DOI: 10.1111/jace.19145

Journal of the American Ceramic Society

RESEARCH ARTICLE

Characterization of graphite–chromium carbide composites manufactured by spark plasma sintering

Juan Piñuela-Noval[1] | **Daniel Fernández-González**[1] | **Marta Suárez**[1] | **Luis Antonio Díaz**[1] | **Luis Felipe Verdeja**[2] | **Adolfo Fernández**[1]

[1]Centro de Investigación en Nanomateriales y Nanotecnología (CINN), Consejo Superior de Investigaciones Científicas (CSIC), Universidad de Oviedo (UO), Principado de Asturias (PA), El Entrego, Asturias, Spain

[2]Departamento de Ciencia de Los Materiales e Ingeniería Metalúrgica, Escuela de Minas, Energía y Materiales, Universidad de Oviedo, Calle Independencia, Oviedo, Asturias, Spain

Correspondence

Daniel Fernández-González, Centro de Investigación en Nanomateriales y Nanotecnología (CINN), Consejo Superior de Investigaciones Científicas (CSIC), Universidad de Oviedo (UO), Principado de Asturias (PA), Avda de la Vega 4-6, 33940 El Entrego, Asturias, Spain.
Email: d.fernandez@cinn.es

Funding information

Spanish Ministry of Science and Innovation; Call Programa Estatal de I+D+i Orientada a los Retos de la Sociedad, Grant/Award Number: RTI2018-102269-BI00; Juan de la Cierva-Formación Program, Grant/Award Number: FJC2019-041139; Government of the Principality of Asturias; Call Programa“Severo Ochoa” of Grants for Research and Teaching of the Principality of Asturias, Grant/Award Number: BP20041

Abstract

This manuscript contains an investigation about the influence of the chromium content on the properties of novel graphite–chromium composites obtained by spark plasma sintering (SPS), with great potential application in heat dissipation. Green compacts of 40 mm in diameter were first obtained by uniaxial pressing at 60 MPa, and then the composite was sintered at 1800°C in SPS under vacuum conditions and a pressure of 30 MPa. These sintering conditions involved local liquid phase, which promoted the densification of the composite up to values close to 90%. Different chromium contents were studied, 0, 1, 2, 5, 7, and 10 vol.%, where the best properties (densification, young modulus, electrical conductivity, thermal conductivity, and flexural strength) were obtained in the case of the composite with 7 vol.% Cr: 86.22%, 52.7 GPa, 0.79 MS/m, 264 W/m K, and 38.97 MPa, respectively, measured in the in-plane direction due to the anisotropic behavior of the composite.

KEYWORDS

chromium, composites, electrical conductivity, graphite, mechanical properties, nanomaterials, spark plasma sintering, thermal conductivity

1 | INTRODUCTION

Heat sinks have as objective to transfer thermal energy from a higher-temperature source to a lower-temperature source (generally air). The development of these devices (and the corresponding materials used for their manufacture) has accompanied the progress of equipment, which is more and more small, light, and efficient, particularly not only in the field of electronic devices or mobile phones, but also in other fields where the lightness and performance are more important than the size, as aerospace applications, high-speed trains, and so on. Metals have been traditionally used in applications where high thermal conductivity was required, for instance, copper and alloys (around 400 W/m K) or aluminum (around 250 W/m K). Nevertheless, the problem arises when metallic materials must operate at high temperatures as some of them melt at temperatures <1000°C, although some other difficulties, as creep, appear at temperatures well-below the melting point. Moreover, the requirements of capacity for heat dissipation are more and more demanding and, sometimes, the thermal conductivity of the metal itself is not sufficient. Therefore, composites metal–metal (copper–tungsten[1]) or metal–diamond (diamond/Cu composites[2]; Cu–0.2% Ti/diamond[3]; Cu–0.3 wt.% B/diamond[4]; Cu–0.5 wt.% Zr/diamond[5,6]) with high thermal conductivity are gaining interest. In some cases, as in Kim et al.,[1] for the Cu–W composites, the value of thermal conductivity is high even at high temperatures (>300 W/m °C at 1000°C, although the best values were measured at around 500°C), which overcomes some of the problems identified in metallic materials, as copper, for instance, which melts at 1085°C. Anyway, those composites with diamond, even when it is one of the highest thermal conductivity materials (2000 W/m K), will be probably difficultly scaled up for wide utilization in thermal management applications due to the price.

Graphite-based composites might be an alternative to the abovementioned materials in thermal management solutions due to the competing advantage of the low density combined with a good thermal conductivity in-plane. In this line, several researchers have investigated high thermal conductivity and low expansion coefficient graphite–copper,[7,8] graphite–aluminum,[9,10] or graphite–magnesium[10] composites with particular interest in the field of electronic industry. Also within the carbon materials, graphene has also attracted interest as additive to improve the thermal conductivity of metals. In this way, Nazeer et al. reported that the addition of 1 wt.% graphene oxide in copper-reduced graphene composites resulted in 80% greater thermal conductivity than in the case of pure copper.[11]

Anyway, graphite matrix composites are the most promising to be used in extreme conditions applications, as rocket nozzles, collimators, or particle accelerators,[12] whether they contain some additive or second phase (molybdenum, copper, diamond, carbon fibers, silicon, silicon carbide, titanium, or tungsten), resulted from the low density and high thermal conductivity. In this line, the addition of reactive metals (particularly niobium, molybdenum, hafnium, tantalum, etc.) to improve the thermal and mechanical properties of the graphite has been studied for at least 50 years,[13,14] although it was not until the last decade when the investigation in this line has received a special attention, particularly in the case of graphite–molybdenum composites due to their potential application as collimators in the CERN (Conseil Européen pour la Recherche Nucléaire) facilities. The interest of graphite–molybdenum composites comes from the excellent mechanical properties conferred by the graphite and molybdenum carbides, which are formed when sintered together, combined with a low density (around 2.5 g/cm^3), refractory character, high thermal stability, and good thermal and electrical conductivities. These graphite–molybdenum composites (and variable amounts of a third phase as titanium, carbon fibers, silicon, silicon carbide or tungsten added to avoid crystallographic transformations, promote the thermal conductivity, increase the resistance to oxidation at high temperatures or improve the mechanical properties) were manufactured by fast novel sintering techniques as rapid hot-pressing of powders mixture[15,16] or spark plasma sintering (SPS),[12,17,18] due to the potential advantages of these techniques regarding high temperatures under a simultaneous application of pressure. Apart from the application in the field of collimators, these graphite–molybdenum composites have been proposed as heat sinks by other authors,[12,18] although their main disadvantage is the sintering temperature, which is above 2000°C. However, other families of graphite–metal composites, that is, graphite–chromium, can solve this problem because this material can provide properties for heat dissipation comparable with those of the graphite–molybdenum–titanium system using sintering temperatures of around 1800°C. Up to now, research within the graphite–chromium system is to be reported, so it is worth studying it. Thus, this manuscript proposes research about the thermal, electrical, and mechanical properties of novel graphite–chromium composites, using SPS technique, for different chromium contents (0, 1, 2, 5, 7, and 10 vol.%).

2 | EXPERIMENTAL PROCEDURES

2.1 | Materials and experimental

Graphite and chromium powders were used as starting materials to prepare graphite–(0, 1, 2, 5, 7, and 10 vol.%) chromium composites.

Graphite (purity of 99%) from Asbury Carbons Company was one of the raw materials used to obtain the samples. The morphology of this crystalline natural graphite was spheroidal flake. The mean particle size, d_{50}, was 6 μm. Spheroidal–flake morphology is useful to promote the compaction of the final composite and, therefore, improve the properties of the sintered composite.[17] Figure 1 provides an image of the graphite powders.

Chromium (purity ≥99%) from Sigma-Aldrich was employed in the experiments. The particles had a spherical–irregular morphology and a mean particle size, d_{50}, of <100 μm. Figure 2 provides an image of the chromium powders used in the composites.

The powder mixtures were prepared in a roller mill (Astursinter S. L. R., Asturias, Spain) using 3 mm alumina balls and a rate of 100 rpm for 24 h to promote the homogenous mixing. Graphite and chromium mixtures (1, 2, 5, 7, and 10 vol.%) were prepared using isopropyl alcohol. This procedure was employed to promote the mixing and ensure a homogeneous material for subsequent steps of

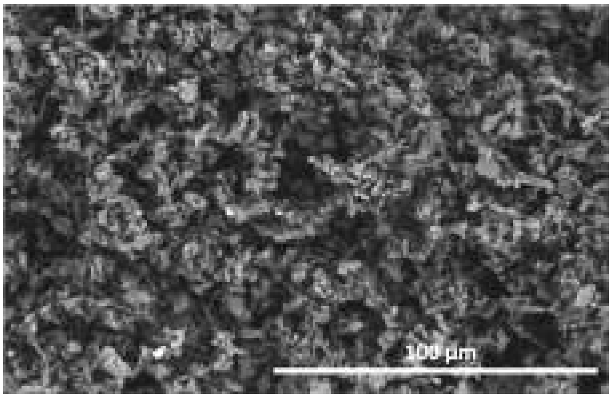

FIGURE 1 Spheroidal–flake morphology graphite used in the experiments.

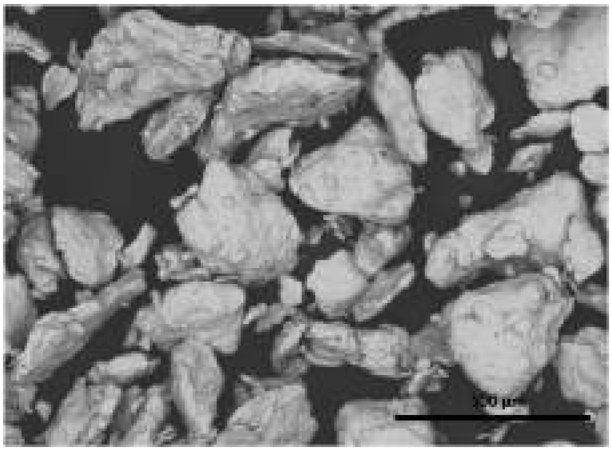

FIGURE 2 Spheroidal–irregular morphology chromium used in the experiments.

the process. Finally, the material was dried at 120°C and sieved through a mesh of 180 μm. Figure 3 corresponds to the powders mixed using the above-reported procedure.

A uniaxial pressure of 60 MPa in metallic mold was used to obtain green compacts that were later placed into a graphite die (40 mm inner diameter) for SPS. The heating cycle up to the sintering temperature had two steps: heating at a rate of 100°C/min from room temperature to 1600°C and heating at 25°C/min from 1600°C to sintering temperature (1800°C). Then, samples were sintered for 20 min of dwell time at 1800°C. A uniaxial pressure of 25 MPa was applied from 1700°C. The temperature was controlled above the sample center using an axial pyrometer focused on the upper graphite punch.

2.2 | Characterization techniques

Field emission scanning electron microscopy on a Quanta FEG 650 was used for the microstructural characterization of the initial raw materials and sintered samples. The microstructure of the sintered samples was analyzed on specimens of fracture surface.

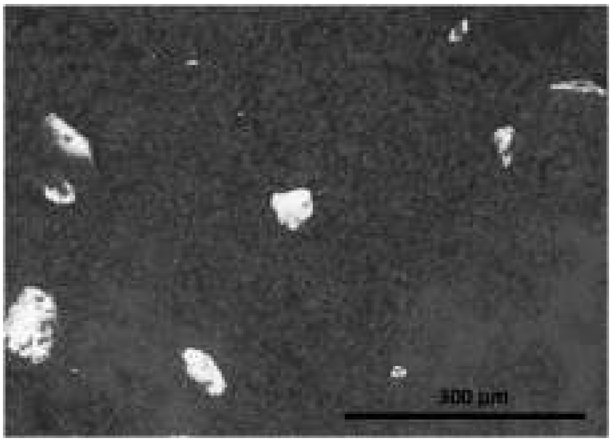

FIGURE 3 Micrograph of the mixed powders, in the image, graphite–10 vol.% chromium.

Mineralogical phases were identified using X-ray diffraction technique with a Bruker Advanced Powder X-ray diffractometer model D8 with Cu-k_α radiation ($\lambda = 0.15406\,\text{nm}$). Copper anticathode water cooled with an intensity of 40 mA and a voltage of 40 kV, a swept between 10 and 70° with a step of 0.02° and a step time of 0.2 s were the working conditions. Crystalline phases were determined with the diffraction pattern files of the JCPDS (International Centre for Diffraction Data).

The relative density of the sintered samples was calculated using the following equation:

$$\rho\ (\%) = \frac{d}{d_{th}} \cdot 100 \qquad (1)$$

where d is the apparent density determined from measurements of mass and volume (diameter and height) and d_{th} is the theoretical density, determined by helium pycnometer (AccuPyc 1330 V2.04N) on powdered samples (<63 μm) of the sintered composite.

Properties were measured in the in-plane direction of samples, except thermal conductivity. The in-plane direction corresponds to the direction perpendicular to the applied pressure. Thermal parameters were measured in the through-plane direction, and the value in the in-plane direction was indirectly calculated by the modified Wiedemann–Franz law ($\lambda/\sigma = L \cdot T$, where λ is the thermal conductivity, σ is the electrical conductivity, L is the modified Lorenz number, assumed to be the same in the in-plane and through-plane directions, and T is the temperature). The other properties in the through-plane direction cannot be measured because the thickness of the sample (3 mm) obtained in the SPS is not sufficient to machine specimens. Electrical conductivity in the through-plane direction is assumed to be <0.1 MS/m, which is supported by the experimental results[12,17,18] for other highly oriented graphite–metal composites, and it is very conservative because the values in this direction are usually 20%–40% lower.[16,17] Values in the through-plane direction are usually between 0.05 and 0.08 MS/m.[17] Wiedemann–Franz law can be applied with sufficient accurateness in graphite–metal composites although with a modified number of Lorenz. In fact, the Wiedemann–Franz law has been applied in other materials different to the metals as carbides,[19,20] polymers,[21] and even graphite.[22,23] The application of the Wiedemann–Franz law in graphite–molybdenum composites provides values of the modified Lorenz number for the in-plane and through-plane directions that do not differ in more than 10% (habitually around 4%–5%).

Samples of 3 mm × 4 mm × 20 mm were prepared to measure the bending strength using the Shimadzu-Series AGS-IX tests machine. Bending strength (σ_f, in MPa) of material after the three-point bending test was evaluated using the following equation:

$$\sigma_f = \frac{3 \cdot P \cdot L}{2 \cdot w \cdot b^2} \tag{2}$$

where P is the failure load in N, L is the distance between supports (span, 12.5 mm) in mm, w is the width of the sample in mm, and b is the thickness of the sample in mm.

Four-point probe measurement technique in the in-plane direction using the equipment PSM1735—NumetriQ—Newtons fourth was employed to determine the electrical conductivity.

Young's modulus was determined on sintered samples of 3 mm × 4 mm × 20 mm (in-plane) with the equipment GrindoSonic (MK, Belgium).

Thermal conductivity was indirectly calculated from the thermal diffusivity (α, mm^2/s), the specific heat (c_p, J/g K), and the density (d, g/cm^3) using the following equation:

$$\lambda = \alpha \cdot d \cdot c_p \tag{3}$$

where λ is the thermal conductivity (W/m K). The measurement of the thermal diffusivity was carried out in the equipment LFA 457 MicroFlash from Netzsch at 25°C on specimens of 10 mm × 10 mm × 3 mm. Specific heat was determined using a C80 (Setaram Instrumentation) calorimeter, equipped with stainless steel cells (S60/1413), in continuous mode, using a heating ramp of 0.1°C/min from 20 to 40°C, with 2 h of stabilization at the start and end temperatures. The data processing was carried out using the Calisto Software.

Coefficient of thermal expansion (CTE) of the graphite–chromium composite was measured in the temperature range from 30 to 150°C in dilatometer equipment (Netzsch DIL402C, Germany). The sample was measured in the in-plane direction (specimen of 5 mm in length, 3 mm in thickness, and 4 mm in width) and in the through-plane direction (specimen of 3 mm in length, 5 mm in thickness, and 4 mm in width).

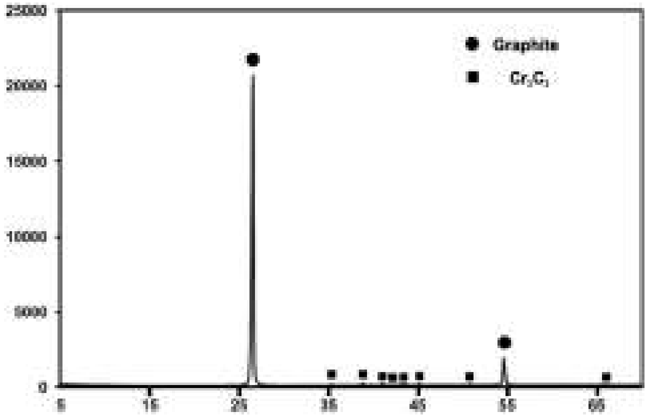

FIGURE 4 X-ray diffraction pattern of the sample graphite–7 vol.% Cr previously uniaxially pressed at 60 MPa and then spark plasma sintering (SPS) sintered at 1800°C–20 min. X-ray diffraction patterns are analogous for the other compositions with changes only in the intensity of the peaks.

3 | RESULTS

3.1 | Phase composition

Figure 4 corresponds to the X-ray diffraction analysis of the sintered specimen, where graphite and chromium (II) carbide are identified.

3.2 | Microstructure

Figure 5a,b corresponds to a sample graphite–7 vol.% Cr, where the chromium (II) carbide appears homogeneously distributed within the matrix of graphite. The disposition of graphite lamellae in the perpendicular direction to the pressure can be seen in Figure 5a. Moreover, it is also possible to identify that chromium (II) carbide appears filling empty spaces in the composite (Figure 5b).

3.3 | Properties

3.3.1 | Density

Relative density of the sintered powders was calculated using Equation (1) and the values are collected in Table 1. Relative density grows as the chromium content in the

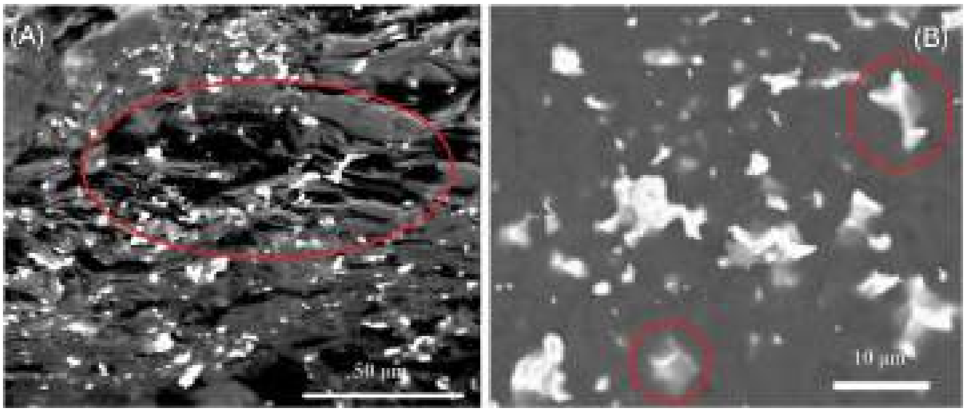

FIGURE 5 Scanning electron microscopy (SEM) images of the sample graphite–7 vol.% Cr previously uniaxially pressed at 60 MPa and then spark plasma sintering (SPS) sintered at 1800°C–20 min: (a) graphite lamellae oriented perpendicular to the pressing visible on fracture surface; (b) chromium carbides appear filling the spaces between grains.

TABLE 1 Density values of the green compacts, apparent density, real and relative density.

Sample	Theoretical density, d_{th} (g/cm^3)s	Apparent density, d (g/cm^3)	Relative density (%)
Graphite	2.2661	1.7337	76.51
Graphite–1 vol.% Cr	2.3101	1.8675	80.84
Graphite–2 vol.% Cr	2.3567	1.9247	81.67
Graphite–5 vol.% Cr	2.5205	2.0987	83.26
Graphite–7 vol.% Cr	2.6422	2.2932	86.79
Graphite–10 vol.% Cr	2.7381	2.3533	85.95

TABLE 2 Electrical conductivity values of the spark plasma sintering (SPS)-samples.

Sample	Electric conductivity (MS/m) (in-plane)
Graphite	0.04 ± 0.01
Graphite–1 vol.% Cr	0.06 ± 0.01
Graphite–2 vol.% Cr	0.12 ± 0.01
Graphite–5 vol.% Cr	0.20 ± 0.02
Graphite–7 vol.% Cr	0.79 ± 0.14
Graphite–10 vol.% Cr	0.45 ± 0.10

composite increases, except for the greatest chromium content (10 vol.% Cr).

3.3.2 | Electrical conductivity

Electrical conductivity values are collected in Table 2. Values of electrical conductivity increase as the chromium content increases except for the sample graphite–10 vol.% Cr.

TABLE 3 Values of the thermal conductivity in the through-plane direction.

Sample	Thermal conductivity (W/m K) (through-plane)	Thermal conductivity (W/m K) (in-plane)
Graphite	13.78	5.25
Graphite–1 vol.% Cr	15.72	9.56
Graphite–2 vol.% Cr	18.44	22.05
Graphite–5 vol.% Cr	29.02	58.94
Graphite–7 vol.% Cr	33.63	264.13
Graphite–10 vol.% Cr	26.06	131.90

3.3.3 | Thermal conductivity

Thermal conductivity values are collected in Table 3, both for the through-plane and in-plane directions. Values in the in-plane direction are significantly greater than in the through-plane direction for chromium contents above 5 vol.%. The values of thermal conductivity in-plane and through-plane directions for chromium content below 5 vol.% are on the same order of magnitude due to the poor densification. The differences in the values in Table 3 are consequence of the assumptions and mathematical calculations indicated in Section 2.2.

3.3.4 | Young's modulus

Young's modulus values are collected in Table 4, where the behavior of the value is similar to that observed in the case of other properties.

TABLE 4 Values of the young modulus of the spark plasma sintering (SPS)-samples.

Sample	Young modulus (GPa)
Graphite	22.53 ± 0.10
Graphite–1 vol.% Cr	23.34 ± 0.12
Graphite–2 vol.% Cr	27.09 ± 0.52
Graphite–5 vol.% Cr	45.50 ± 0.29
Graphite–7 vol.% Cr	52.73 ± 0.46
Graphite–10 vol.% Cr	46.39 ± 0.57

TABLE 5 Values of the bending strength.

Sample	Bending strength (MPa)
Graphite	23.93 ± 3.63
Graphite–1 vol.% Cr	18.95 ± 1.26
Graphite–2 vol.% Cr	21.36 ± 1.51
Graphite–5 vol.% Cr	30.87 ± 2.17
Graphite–7 vol.% Cr	38.97 ± 2.27
Graphite–10 vol.% Cr	42.71 ± 0.72

3.3.5 | Bending strength

Values of the bending strength appear in Table 5. The best results were obtained, as opposed to other cases, for the graphite–10 vol.% Cr (42.71 MPa), although without significant differences with the composite graphite–7 vol.% Cr (38.97 MPa).

4 | DISCUSSION

Graphite–metal composites have found interest in different fields, particularly for extreme conditions applications, as collimators for CERN.[15,16,17] However, these graphite–metal composites might be used in heat dissipation. The great advantage of graphite–metal composites is the refractory character, the high thermal stability, the physical and mechanical properties as well as the thermal and electrical conductivities. Despite the potential interest of graphite–metal composites in the above-reported applications, researchers focused only on the graphite–molybdenum system. Nevertheless, there are other graphite–metal systems with promising possibilities in this line. This is the case of the graphite–chromium system, which has never been reported in the literature. Sintering in the graphite–chromium system, as opposed to the graphite–molybdenum, requires from lower temperatures. Sintering temperatures of 1800°C are sufficient to consolidate the starting powders in presence of liquid, which is at least 200°C lower than that required for the sintering of graphite–molybdenum composites.[12,17] Time is also shorter, as the sintering cycle (heating + dwell time + cooling in SPS) takes 44 min + cooling in SPS equipment in front of the 131 min + cooling in the SPS apparatus required in the graphite–molybdenum system.[12] The competitive advantage of the C–Cr system, in comparison with the C–Mo system, is precisely the temperature required for the liquid phase sintering. In the C–Cr binary diagram, there is a phase transformation at a temperature of 1811°C, whereas in the C–Mo binary diagram, the phase transformation that involves liquid phase takes place at 2584°C, for the compositions studied in this system. These temperatures required for the appearance of liquid phase are slightly lower in the SPS due to both the vacuum conditions and the pressure applied in the process. Therefore, sintering in this research occurred in presence of liquid phase as it is clearly visible in Figure 5b, where liquid chromium appears in triple points and grain boundaries. In fact, it is not chromium but chromium (II) carbide, as it was identified in the X-ray diffraction analysis in Figure 4. This is consistent with the carbon–chromium diagram, which for the compositions studied in this manuscript, indicates that graphite and Cr_3C_2 are the stable phases at room temperature. The Cr_3C_2 is formed by reaction of the solid (graphite) and liquid (chromium), where carbon atoms dissolve in the liquid phase and diffuse, and eventually carbon structures are built to sinter together the graphite powders into solid graphite. The solidification of the liquid phase results into $Cr_7C_3 + Cr_3C_2$, but with excess carbon composition and unimpeded carbon diffusion, the system moves to the $Cr_3C_2 + C$ zone.[24] The presence of the liquid phase promotes the densification of the composite, with a maximum of relative density for the composite with 7 vol.% Cr (Table 1). This can be explained because there is an excess of liquid phase for greater chromium contents (10 vol.%), for the conditions of pressure and temperature in the SPS, that migrates in minor quantities to the borders of the sample and appears deposited in the walls of the mold after the sintering process. This leads to a reduction in the densification (and material losses), which is translated later into the thermal, electrical, and mechanical properties of the composite. Values of relative density do not significantly exceed the 85%, which is consistent with the information provided by Aguiar et al.[25] that indicates that densification above 85% is difficulty reached in the case of graphite materials. Within the graphite–metal composites, it is necessary to apply relatively high pressures to obtain the green compacts. Guardia-Valenzuela et al.,[17] for the graphite–molybdenum–titanium system employed a pressure of 300 MPa to obtain the green compacts, although Suárez et al.[18] observed that using pressures >60 MPa did not translate into a significant increase in the value of the density of the green compacts. Therefore, considering the similitude between the graphite–Mo and graphite–Cr systems, a pressure of 60 MPa was applied, and it was seen sufficient to see an alignment of the graphite in the direction perpendicular to the pressing, as it is observed in Figure 5a. Later, the applied pressure in the SPS machine produces a further alignment of the graphite flakes in the basal direction, which ensures a directional behavior with the best properties being measured in the in-plane direction. In this way, liquid chromium–chromium carbides migrate throughout the lamellae of graphite preferentially in the in-plane direction, filling spaces as in Figure 5b, which enhances further the anisotropic behavior of these composites.

The anisotropic behavior of graphite regarding electrical conductivity was already reported in the forties of the last century.[26] For instance, thermal pyrolytic graphite in the in-plane direction exhibits an electrical conductivity of 2.4 MS/m. Other research studies for graphite with metal additions (molybdenum, titanium) have reported values of the electrical conductivity approaching 1 MS/m in the in-plane direction: 0.88–1.01 MS/m in-plane by Guardia-Valenzuela et al.[17]; 0.86 MS/m in-plane by Suárez et al.[18]; or, 0.99 MS/m in-plane by Suárez et al.[12] The greatest value reported in this manuscript measured in the in-plane direction is 0.79 MS/m, which is not far from these values. The influence of the chromium carbide in the promotion of the electrical conductivity is clearly observed in Table 2, which is also consistent with the trend of the relative density indicated in Table 1 and the problems of chromium losses by extrusion identified in the sample with 10 vol.% Cr. The high electrical conductivity in the sample with 7 vol.% Cr can be explained by the initial graphite flakes bonded together in a highly oriented matrix with chromium carbides being the main responsible of the high electrical conductivity. This behavior is translated into the thermal conductivity due to the parallelism between the electrical and thermal behaviors. In this line, the electrical conductivity of the chromium (II) carbide is 13.33 MS/m[27] while that of the graphite in the basal plane approaches 1 MS/m,[28] although it is possible to see that the value of the electrical conductivity of the graphite sintered in the SPS apparatus is well-below this value (0.04 MS/m) whether second phases are not added. Therefore, it is the chromium carbide the responsible of the electrical (and thermal) conductivity of the composite. Densification also plays an important role in the electrical (thermal and mechanical properties), as electrical conductivity is directly related to the densification of the composite, according to the results in Tables 1 and 2. Thus, in this line, it is possible to find works of researchers who studied what would be the critical volume that leads the graphite–air being insulating[29] and determined how the orientation of the graphite is important for the electrical conductivity of graphite-based composites.[30] Phenomena that explain the difficulty of reaching high values of electrical conductivity without employing metallic or metal carbide additives. So, liquid chromium (II) carbide can more easily displace in the in-plane direction due to both the orientation of the graphite planes produced by the pressure applied to obtain the green compacts and the pressure during the sintering process in the SPS. This, apart from the promotion of the densification of the composite, provides more metallic continuity in the in-plane direction, which apart from the influence on the thermal and electrical properties of the composite reflects into the mechanical properties of the composite. Reducing the chromium content decreases the importance of this mechanism. The values of thermal conductivity are comparable with those proposed by Guardia-Valenzuela et al.[17] (in-plane, 647—740 W/m K; through-plane, 56—50 W/m K), Suárez et al.[12] (in-plane, 136.68 W/m K; through-plane, through-plane, 22.09 W/m K), and Suárez et al.[18] (in-plane, 201.49 W/m K; through-plane, 23.43 W/m K) for graphite–molybdenum–titanium composites, which indicates that the graphite–chromium composites could be used in the field of heat sinks with similar behavior regarding thermal conductivity but with lower sintering temperature. Graphite itself, even when it can reach very high thermal conductivity values in highly oriented thermal pyrolytic graphite (up to 1900 W/m K[31]), does not exhibit such values of thermal conductivity in this case. Thermal conductivity is very far from these values in the graphite sintered with the SPS apparatus, which suggests that the increase of the thermal conductivity is directly related to not only the improvement of the densification produced when the chromium content increases but also by the own chromium, which has a thermal conductivity of around 190 W/m K.[32]

Regarding the mechanical properties of the composite, these follow a trend like that of the thermal and electrical properties. Values of the young's modulus are in clear correlation with the relative density values collected in Table 1, and also with chromium content in the sample. It is important to consider that chromium (II) carbide has a young's modulus of around 373 GPa according to Powell and Schofield,[22] whereas that of graphite sintered using the SPS apparatus is 22.53 GPa (for a relative density of 76%). Therefore, chromium carbide is responsible for the increasing value of the young modulus, although the densification has a relevant role that explains the deterioration of the young modulus for the composite with 10 vol.% Cr (together with the potential chromium (II) carbide losses produced by extrusion during the sintering process). The increase of the resistance as the chromium content increases is the result of chromium (II) carbide that improves the mechanical resistance of the composite. The mechanical resistance, as in the case of the graphite–molybdenum composites, is thought to be conferred by the strong carbide–graphite bond, which provides bridges not only in the in-plane direction but also in the perpendicular direction and limits the basal plane slip (shear) and the delamination.

Results suggest that the best composite is that formed by graphite and 7 vol.% Cr, which provides the greatest values of electrical and thermal conductivities with a bending strength comparable with that of the composite with 10 vol.% Cr, which is the composite with the greatest value in this parameter. The CTE is important for the materials that are going to be used in heat dissipation because they should be cooperative with the rest of the structure of the device. The CTE was determined for this sample graphite–7 vol.% Cr in the in-plane direction and in the through-plane direction. The values are $3.21{\cdot}10^{-6}$ and $12.82{\cdot}10^{-6}$ K^{-1}, respectively. Apart from the low values, whether compared with those of other conventional materials used in heat dissipation as the aluminum ($25.5{\cdot}10^{-6}$ K^{-1}) or copper ($16.7{\cdot}10^{-6}$ K^{-1}), they are comparable with other competing composite alternatives including diamond, that is, Al-diamond or Cu-diamond, although the advantage of the graphite–chromium composite is the lower weight. The coefficients of thermal expansion allow defining an isotropy ratio, by relation between the property in the in-plane direction and the value in the through-plane direction, which is:

$$\mathrm{IR} = \frac{\mathrm{CTE}_{\perp}}{\mathrm{CTE}_{||}} = \frac{3.21 \cdot 10^{-6}\ \mathrm{K}^{-1}}{12.82 \cdot 10^{-6}\ \mathrm{K}^{-1}} = 0.2504 \qquad (4)$$

where $\mathrm{CTE}_{\perp}$ is the CTE in the in-plane direction (perpendicular direction to the applied pressure), whereas $\mathrm{CTE}_{||}$ is the CTE in the through-plane direction (parallel direction to the applied pressure). A value equal or close to 1 indicates an isotropic material,[33] whereas the smaller the IR, the more anisotropic the composite is. Considering the criteria of Seehra et al.,[34] this composite with a ratio $\mathrm{CTE}_{\perp}/\mathrm{CTE}_{||}$ closer to zero is very anisotropic.

The anisotropic behavior of the composite was studied in detail with the support of the X-ray diffraction technique. X-ray spectra were obtained in the in-plane and through-plane directions using 2θ continuous scanning method at a scanning rate of 1°/min, within the range 10°–60° as in Lee et al.[35] A parameter called Da was obtained by using the values of the intensity of the peaks corresponding to the planes (0 0 2) and (1 0 0) as follows:

$$Da = \frac{I_{100}}{I_{100} + I_{002}} \qquad (5)$$

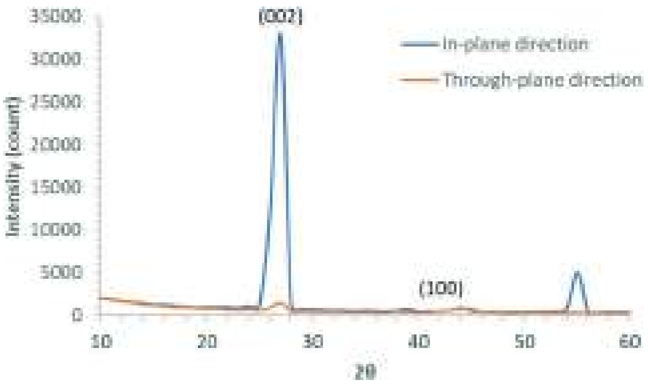

FIGURE 6 X-ray diffractometer spectra of the sintered specimen graphite–7 vol.% Cr in the in-plane (blue) and through-plane (orange) directions.

The X-ray spectra in the in-plane and through-plane directions are collected in Figure 6. The peaks corresponding to the planes (0 0 2) and (1 0 0) appear in the angles 27° (32 942 counts in the in-plane direction and 1469 counts in the through-plane direction) and 42° (548 counts in the in-plane direction and 562 counts in the through-plane direction).

Using Equation (5), the values of the $\mathrm{Da}_{\perp}$, corresponding to the in-plane X-ray diffractogram, and $Da_{||}$, corresponding to the through-plane diffractogram, are 0.2767 and 0.0164, respectively. The anisotropy ratio is calculated as the relation between the $\mathrm{Da}_{\perp}$ and $Da_{||}$ as $\mathrm{Da}_{\perp}/\mathrm{Da}_{||}$. The value is 16.87, which indicates the clear anisotropic behavior of graphite–chromium composites, because the greater the value the more anisotropic the material is.

5 | CONCLUSIONS

A family of graphite-matrix composite material containing chromium particles (chromium carbide, $\mathrm{Cr_3C_2}$, after sintering) has been successfully developed for heat management applications. Composites are produced by SPS assisted by molten metal–carbon liquid phase. Different chromium contents were studied (0, 1, 2, 5, 7, and 10 vol.%) to evaluate the influence of this element in the thermal, electrical, and mechanical properties of the composite (densification, young's modulus, electric conductivity, thermal conductivity, and flexural strength).

As the composite mainly consists of oriented graphite, the material exhibits anisotropic properties with in-plane properties comparable to those of the already investigated graphite–molybdenum composites. In fact, the anisotropy of the composite was studied using CTE and X-ray diffraction technique, which confirm this behavior. As the sintering temperature (1800°C) is well-bellow that required for the graphite–molybdenum composites (up to 2600°C), the production of graphite–chromium composites might be a competing alternative that could be easier scaled up to industrial level and being a competitor for thermal management applications.

The best values of thermal, electrical, and mechanical properties were obtained in the case of graphite–7 vol.% Cr (densification, young modulus, electric conductivity, thermal conductivity, and flexural strength): 86.22%, 52.7 GPa, 0.79 MS/m, 264 W/m K, and 38.97 MPa, respectively. Greater chromium content resulted in liquid metal losses during the sintering process, which is detrimental for the properties of the composite, particularly for the thermal and electrical conductivities, whose values are a 40% lower.

ACKNOWLEDGMENTS

This research was funded by the Spanish Ministry of Science and Innovation, Call Programa Estatal de I+D+i Orientada a los Retos de la Sociedad (RTI2018-102269-B-I00). Daniel Fernández-González acknowledges the grant (Juan de la Cierva-Formación Program) FJC2019-041139-I funded by MCIN/AEI/10.13039/501100011033 (Ministerio de Ciencia e Innovación, Agencia Estatal de Investigación). Juan Piñuela Noval acknowledges the Programa "Severo Ochoa" of Grants for Research and Teaching of the Principality of Asturias for the funds received for the elaboration of the Ph. D. Thesis (Ref: BP20 041). Authors are grateful to Ainhoa Macías San Miguel from Nanomaterials and Nanotechnology Research Center (CINN) for providing technical assistance.

REFERENCES

1. Kim YDo, Oh NL, Oh S-T, Moon In-H. Thermal conductivity of W–Cu composites at various temperatures. Mater Lett. 2001;51:420–4.
2. Shen X-Y, He X-B, Ren S-B, Zhang H-M, Qu X-H. Effect of molybdenum as interfacial element on the thermal conductivity of diamond/Cu composites. J Alloys Compd. 2012;529:134–9.
3. Yang L, Sun L, Bai W, Li L. Thermal conductivity of Cu-Ti/diamond composites via spark plasma sintering. Diamond Relat Mater. 2019;94:37–42.
4. Bai G, Li N, Wang X, Wang J, Kim MJ, Zhang H. High thermal conductivity of Cu-B/diamond composites prepared by gas pressure infiltration. J Alloys Compd. 2018;735:1648–53.
5. Li J, Wang X, Qiao Yi, Zhang Y, He Z, Zhang H. High thermal conductivity through interfacial layer optimization in diamond particles dispersed Zr-alloyed Cu matrix composites. Scr Mater. 2015;109:72–5.
6. Wang L, Li J, Bai G, Li N, Wang X, Zhang H, Wang J, Kim MJ. Interfacial structure evolution and thermal conductivity of Cu-Zr/diamond composites prepared by gas pressure infiltration. J Alloys Compd. 2019;781:800–9.
7. Yang W, Zhou L, Peng K, Zhu J, Wan L. Effect of tungsten addition on thermal conductivity of graphite/copper composites. Composites B: Eng. 2013;55:1–4.
8. Byun M, Kim D, Sung K, Jung J, Song Y-S, Park S, Son I. Characterization of copper–graphite composites fabricated via electrochemical deposition and spark plasma sintering. Appl Sci (Basel). 2019;9:2853.
9. Chen JK, Huang IS. Thermal properties of aluminum–graphite composites by powder metallurgy. Composites B: Eng. 2013;44:698–703.
10. Oddone V, Boerner B, Reich S. Composites of aluminum alloy and magnesium alloy with graphite showing low thermal expansion and high specific thermal conductivity. Sci Technol Adv Mater. 2017;18:180–6.
11. Nazeer F, Ma Z, Gao L, Wang F, Khan MA, Malik A. Thermal and mechanical properties of copper-graphite and copper-reduced graphene oxide composites. Composites B: Eng. 2019;163:77–85.
12. Suárez M, Fernández-González D, Díaz LA, Borrell A, Moya JS, Fernández A. Synthesis and processing of improved graphite-molybdenum-titanium composites by colloidal route and spark plasma sintering. Ceram Int. 2021;47:30993–8.
13. White JL, Pontelandolfo JM. Graphite-carbide materials prepared by hot-working with a dispersed liquid-carbide phase. Carbon. 1966;4:305–14.
14. Harada Y, Rubin GA. Fabrication and characterization of metal carbide-graphite composites. In: Paper presented at the 68th Annual Meeting of the American Ceramic Society. 1966 May 9. Washington, D C, USA. (https://ntrs.nasa.gov/api/citations/19680009751/downloads/19680009751.pdf)
15. Bertarelli A, Bizarro S. A molybdenum carbide/carbon composite and manufacturing method. World Patent PCT/EP2013/072818. Oct. 2013.
16. Mariani N. Development of novel. In: Advanced molybdenum-based composites for high energy physics applications. Ph.D. Thesis. Milan (Italy): Milan Polytechnic; 2014.
17. Guardia-Valenzuela J, Bertarelli A, Carra F, Mariani N, Bizzaro S, Arenal R. Development and properties of high thermal conductivity molybdenum carbide – graphite composites. Carbon. 2018;135:72–84.
18. Suárez M, Fernández-González D, Gutiérrez-González CF, Díaz LA, Borrell A, Moya JS, et al. Effect of green body density on the properties of graphite-molybdenum-titanium composite sintered by spark plasma sintering. J Eur Ceram Soc. 2022;42:2048–54.
19. Schultrich B, Poeβnecker W. Thermal conductivity of cemented carbides. J Therm Anal. 1988;33(1):305–10. https://doi.org/10.1007/bf01914616
20. Jiang Q, Zeng X, Hu C. A promising layered thermoelectric metallic ceramic with ultra-high temperature stability: Mo2Ti2AlC3, J Alloys Compd. 2022;922:166212. https://doi.org/10.1016/j.jallcom.2022.166212
21. Upadhyaya M, Boyle CJ, Venkataraman D, Aksamija Z. Effects of disorder on thermoelectric properties of semiconducting polymers. Sci Rep, 2019;9:5820. https://doi.org/10.1038/s41598-019-42265-z
22. Powell RW, Schofield FH. The thermal and electrical conductivities of carbon and graphite to high temperatures. Proc Phys Soc. 1939;51(1):153–72. https://doi.org/10.1088/0959-5309/51/1/317
23. Cermak M, Perez N, Collins M, Bahrami M. Material properties and structure of natural graphite sheet. Sci Rep. 2020;10:18672. https://doi.org/10.1038/s41598-020-75393-y

24. Guardia-Valenzuela J. Optimisation of graphite matrix composites for collimators in the LHC upgrade. Ph.D. Thesis. Zaragoza (Spain): University of Zaragoza; 2019.
25. Aguiar JA, Kwon S, Coryell BD, Eyerman E, Bokov AA, Castro RHR, et al. Densification of graphite under high pressure and moderate temperature. Mater Today. 2020;22:100821.
26. Krishnan KS, Ganguli N. Large anisotropy of the electrical conductivity of graphite. Nature. 1939;144:667.
27. Tulhoff H. Carbides. In: ULLMANN'S encyclopedia of industrial chemistry. Weinheim: Wiley-VCH Verlag GmbH & Co; 2012. p. 565–82.
28. Yemata TA, Ye Q, Zhou H, Kyaw AKK, Chin WS, Xu J et al. 6 – Conducting polymer-based thermoelectric composites: principles, processing, and applications. In: Thakur VK, Thakur MK, Pappu A, editors. Hybrid polymer composite materials. Kidlington: Woodhead Publishing; 2017. p. 169–95.
29. Deprez N, Mclachlan DS. The analysis of the electrical conductivity of graphite conductivity of graphite powders during compaction. J Phys D: Appl Phys. 1988;21:101.
30. Marinković S, Sužnjević C, Djordjević M. Pressure dependence of the electrical resistivity of graphite powder and its mixtures. Phys Status Solidi A: App Mater Sci. 1971;4:743–54.
31. Klemens PG, Pedraza DF. Thermal conductivity of graphite in the basal plane. Carbon. 1994;32:735–41.
32. Shackelford JF, Han Y-H, Kim S, Kwon S-H et al. CRC Materials science and engineering handbook. London: CRC Press; 2015.
33. Lee S-M, Kang D-Su, Roh J-S. Bulk graphite: materials and manufacturing process. Carbon Lett. 2015;16:135–46.
34. Seehra MS, Pavlovic AS, Babu VS, Zondlo JW, Stansberry PG, Stiller AH. Measurements and control of anisotropy in ten coal-based graphites. Carbon. 1994;32:431–5.
35. Lee S-M, Kang D-Su, Kim W-S, Roh J-S. Fabrication of isotropic bulk graphite using artificial graphite scrap. Carbon Lett. 2014;15:142–15.

How to cite this article: Piñuela-Noval J, Fernández-González D, Suárez M, Díaz LA, Verdeja LF, Fernández A. Characterization of graphite–chromium carbide composites manufactured by spark plasma sintering. J Am Ceram Soc. 2023;106:5157–5166. https://doi.org/10.1111/jace.19145

Artículo 3: Spark plasma sintering of graphite-chromium carbide composites: Influence of the sintering temperature and powder synthesis method.

Ceramics International 49 (2023) 33891–33900

Contents lists available at ScienceDirect

Ceramics International

journal homepage: www.elsevier.com/locate/ceramint

Spark plasma sintering of graphite-chromium carbide composites: Influence of the sintering temperature and powder synthesis method

J. Piñuela-Noval [a], D. Fernández-González [a,*], M. Suárez [a], C. Gómez-Rodríguez [b], A. Fernández [a]

[a] *Nanomaterials and Nanotechnology Research Center (CINN-CSIC), Universidad de Oviedo (UO), Principado de Asturias (PA), Avda. de la Vega, 4-6, 33940, El Entrego, Spain*

[b] *Departamento de Mecánica, Facultad de Ingeniería, Campus Coatzacoalcos, Universidad Veracruzana, Av. Universidad Km 7.5 Col. Santa Isabel, Coatzacoalcos, 96535, Veracruz, Mexico*

ARTICLE INFO

Handling Editor: Dr P. Vincenzini

Keywords:
Graphite
Spark plasma sintering
Colloidal processing route
Thermal properties
Mechanical properties
Electrical properties
Nanomaterials
Composites

ABSTRACT

Carbon-metal carbide composites are a novel family of materials with potential application in heat dissipation due to the lightness and thermal-mechanical properties. Within these composites, those of graphite-chromium carbide have been still few studied. Therefore, this research focuses on both the influence of the powder preparation method (mechanical mixing (MM) and colloidal synthesis (CS)) and the spark plasma sintering (SPS) temperature (1600, 1700, 1800, 1900 and 2000 °C) in the properties of the composite graphite-7 vol. Cr. Results indicate that the composites sintered from powders processed by CS exhibit better properties, which can be explained by the better dispersion of the chromium carbide, formed during the sintering process, in the matrix of composite. Apart from the powder preparation method, sintering temperature has influence on the properties of the composite: 1900 °C is the best in the case of the route CS + SPS, while 2000 °C is the best option in the route MM + SPS. The thermal conductivity in-plane is 1.75 times greater in the CS than in the MM route, which suggests a better performance in the composite processed by colloidal route in heat dissipation applications.

1. Introduction

Heat dissipators are passive elements that transfer the heat generated by an electronic or mechanic device to a fluid, which is habitually air, or any liquid or gas coolant, that allows regulating the temperature of the equipment. Within this line, heat dissipation is an important issue in different sectors (including the great importance of the miniaturization of devices, where heat dissipation could be a problem), due to the aim of extending the lifespan of equipment and avoiding its soon deterioration (due to an increase of the temperature) and requirement of replacement or removal, which involves significant costs [1]. Therefore, if the Arrhenius equation is considered, the lifespan of a device could be reduced to a half when the temperature increases 10 °C [2]. For that reason, heat dissipators must be adequately designed to ensure the correct heat transfer and, therefore, the selection of the correct material is highly important [3]. The suitable material, apart from high thermal and electrical conductivities, must have a low coefficient of thermal expansion, or at least similar to that of the other components of the device [4], and low density is expected to not increase the weight of the equipment.

Conventional heat exchangers are usually manufactured with monolithic metals and metallic alloys, which include ferrous alloys and, aluminium and copper alloys [4–8]. Within this context, aluminium (and alloys) is currently used due to the lightness, low cost, and easy machinability despite the limitations related with its low melting point and high coefficient of thermal expansion ($25.5 \cdot 10^{-6}$ K^{-1}). On the other hand, copper has a greater thermal conductivity and can be used at higher temperatures, although it has also a great coefficient of thermal expansion ($16.7 \cdot 10^{-6}$ K^{-1}) and it is heavier and more expensive. Novel composites are being developed to overcome some of the problems observed in the copper composites used for heat dissipation, as the copper-silicon carbide [9], copper-molybdenum [10], copper-titanium [11], copper-tungsten [12] and copper-aluminium nitride [13] composites. Additionally, carbon materials are being incorporated to copper or aluminium (composites) to improve the thermal conductivity and reduce the relative density: copper-diamond [14], copper-carbon fibres [15], copper-boron-diamond [16], copper-zirconium-diamond [17], or graphite-aluminium [18]. Within carbon materials, diamond has great interest for thermal applications, particularly in the microelectronics industry due to the high electrical resistivity and thermal conductivity

---

* Corresponding author.
E-mail address: d.fernandez@cinn.es (D. Fernández-González).

https://doi.org/10.1016/j.ceramint.2023.08.083
Received 16 December 2022; Received in revised form 22 July 2023; Accepted 6 August 2023

[19,20], being diamond the known material with the highest thermal conductivity [21,22] (>2200 W/m·K). Nevertheless, the high cost of the diamond as well as the scarceness makes not viable its massive utilization in electronics or heat dissipation. As alternative, synthetic diamond is used and different metal matrix composites with diamond have been proposed as copper-, aluminium-, silver- and silicon carbide-diamond composites [23,24]. Recently, investigation is being conducted with other carbon allotrope, graphene, because of its high thermal conductivity [25–28], although it is not completely clear whether this material improves the thermal conductivity [29] or not [2] when used in metal matrix composites.

The most promising material in heat dissipation is graphite due to the low density, good chemical stability, excellent thermal and electrical conductivities, low coefficient of thermal expansion and acceptable mechanical properties, combined with a low cost whether compared with the other carbon allotropes. Pyrolytic graphite is very popular in the electronic industry due to the high thermal conductivity in the in-plane direction despite the high temperatures (>3000 °C) required for graphitization [30]. However, the incorporation of metals (Nb, Mo, Hf, Ta, Cu, or others) to the graphite matrix allows obtaining, at lower temperatures, composites with high thermal conductivity to be used in heat dissipation. The first investigations in this line date from the sixties [31] although it was not until the 2010s when research in this line resulted attractive again due to the potential utilization of the graphite-molybdenum-titanium composites in collimators of the Large Hadron Collider in the CERN installations (*Conseil Européen pour la Recherche Nucléaire*, European Organization for Nuclear Research in English) [32]. Sintering temperature is high (>2500 °C) to obtain the composites with the suitable properties, but it is possible to obtain them at lower temperature (without presence of liquid phase) without significantly impairing the thermal-mechanical properties required for heat dissipation [33–35]. Nevertheless, the high sintering temperatures required to obtain high values of relative density are still a challenge for the competitiveness of the graphite-molybdenum-titanium composites. For that reason, other graphite-metal systems with potential lower sintering temperature are being explored as, for instance, the graphite (carbon)-chromium system [36], whose binary phase diagram exhibits transformations that involve liquid phase at temperatures well below of those of the graphite(carbon)-molybdenum system. Therefore, this manuscript proposes a detailed study about the properties of graphite-chromium carbide composites when considering two variables of study: the sintering temperature and the powder processing method (mechanical mixing of powders and colloidal processing route).

2. Experimental procedure

2.1. Materials and methodology

Graphite-7 vol. % chromium composites were prepared. The chromium content in the initial mixture was chosen based on the results obtained in previous research of Piñuela-Noval et al. [36]. Two routes of preparation of the powders were followed:

- *Mechanical mixing in a roller mill* (MM). As raw materials, graphite (crystalline natural graphite, grade 93,004, Asbury Carbons Company, flake morphology, d_{50} = 6.007 μm) and chromium (Sigma Aldrich, CAS: 7440-47-3, purity ≥99%, spherical particles with a mean particle size (d_{50}) of <45 μm) were used. Powders were mixed in a roller mill (Astursinter S. L. R., Asturias, Spain) with 3 mm alumina balls in a rate of 1:4 and isopropyl alcohol to improve the homogeneous chromium distribution in the carbonaceous matrix. After 24 h at 100 rpm, the compound was dried in a stove at 120 °C and sieved by 180 μm.
- *Colloidal synthesis* (SC). As raw materials, graphite (crystalline natural graphite, grade 93,004, Asbury Carbons Company, flake morphology, d_{50} = 6.007 μm), as matrix constituent, and hexahydrate chromium (III) chloride (Fluka, CAS: 10,060-12-5), as the precursor of chromium, were used. The colloidal processing route consisted of adding dropwise a solution of $CrCl_3·6H_2O$ in ethanol into a dispersion of graphite in ethanol. The slurry was then heated under magnetic stirring at 60 °C and subsequently dried in stove at 120 °C for 24 h to start the nucleation of the chromium precursor and remove any traces of alcohol. Dried powder was grounded and sieved by 180 μm. Finally, the powders were thermally treated in a furnace at 450 °C for 2 h in air with a heating rate of 5 °C/min to eliminate chloride and water traces, while chromium (III) oxide is formed at this stage.

The following step consisted in the preparation of green compacts in metallic mould by uniaxial pressing at 60 MPa in the form of discs of 40 mm in diameter and >3 mm in thickness. Later, green compacts were sintered in the spark plasma sintering equipment. Samples were placed inside of the graphite mould and sintered at a heating rate of 100 $°C·min^{-1}$ up to 1600 °C and 25 $°C·min^{-1}$ to the sintering temperature in a spark plasma sintering apparatus (FCT-HP D25/1) under an applied pressure of 30 MPa during all sintering process and in a vacuum condition (10^{-1} mbar). The sintering temperatures were 1600, 1700, 1800, 1900 and 2000 °C and holding time of 20 min.

2.2. Characterization techniques

Microstructural characterization of the sintered samples was carried out by means of scanning electron microscope (MEB JEOL-6610LV with microanalysis) and maximum resolution of 3 nm.

Mineralogical phases identification was carried out in a Bruker Advanced Powder X-ray diffractometer model D8 with Cu-kα radiation (λ = 0.15406 nm). Copper anticathode water cooled with an intensity of 40 mA and a voltage of 40 kV, a swept between 10 and 70° with a step of 0.02° and a step time of 0.2 s were the working conditions. Peak fitting of the crystalline phases was performed by diffraction pattern files provided by JCPDS (International Centre for Diffraction Data), using XPowder Software.

Relative density or densification was determined by means of Eq. (1).

$$\rho(\%) = \frac{d}{d_{th}} \cdot 100 \tag{1}$$

where d is the apparent density which was obtained from measurements of mass and volume (diameter and height) and d_{th} is the theoretical density, determined by helium pycnometer (AccuPyc 1330 V2.04 N) on powdered samples (<63 μm) of the sintered composite.

Except thermal conductivity, properties were measured in the in-plane direction of the samples due to the thickness of the sintered specimens (3 mm). The in-plane direction is identified with the perpendicular direction to the applied pressure. Thermal parameters were, on the contrary, measured in the through-plane direction also due to the thickness of the specimens. The value of the thermal conductivity in the in-plane direction was indirectly calculated by the modified Wiedemann-Franz law ($\lambda/\sigma = L \cdot T$, where λ is the thermal conductivity, σ is the electrical conductivity, L is the modified Lorenz number, assumed to be the same in the in-plane and through-plane directions, and T is the temperature). Specimens cannot be machined from the sintered samples due to the thickness of the sample (3 mm) and the other properties were non measured in the through-plane direction, which is unfavorable.

3 mm x 4 mm x 20 mm samples were used to determine the flexural strength using the Shimadzu-Serie AGS-IX test machine. Flexural strength (σ_f, in MPa) of the samples measured by means of the three-point bending test was evaluated using Eq. (2).

$$\sigma_f = \frac{3 \cdot P \cdot L}{2 \cdot w \cdot b^2} \tag{2}$$

where P is the failure load in N, L is the distance between supports (span, 12.5 mm) in mm, w is the width of the sample in mm and b is the thickness of the sample in mm.

Four-point probe measurement in the in-plane direction was used to determine the electrical conductivity of the samples. The equipment PSM1735 - NumetriQ - Newtons 4th was used.

Grindsonic (MK, Belgium) was used to measure the Young's modulus on samples of 3 mm x 4 mm x 20 mm in-plane direction.

Thermal conductivity is an indirect measurement, and it is calculated from the thermal diffusivity and the specific heat using Eq. (3).

$$\lambda = \alpha \cdot d \cdot c_p \quad (3)$$

where λ is the thermal conductivity (W/m K, α is the thermal diffusivity (mm^2/s), d is the density (g/cm^3) and c_p is the specific heat (J/g K). The measurement of the thermal diffusivity was carried out in the equipment LFA 457 MicroFlash from Netzsch at 25 °C on specimens of 10 mm x 10 mm x 3 mm. Specific heat was determined using a C80 (Setaram Instrumentation) calorimeter, equipped with stainless steel cells (S60/1413), in continuous mode, using a heating ramp of 0.1 °C/min from 20 to 40 °C, with 2 h of stabilization at the start and end temperatures. The data processing was carried out using the Calisto Software.

The coefficient of thermal expansion (CTE) was determined in Netzsch DIL402C dilatometer equipment in the temperature range from 30 °C to 150 °C for the samples with the best properties.

3. Results and discussion

3.1. Densification and microstructure

Values of relative density are reported in Table 1. There is an evident improvement of the densification when using the colloidal processing route as values of relative density exceed 90% when the sintering temperatures were as high as 1900 and 2000 °C.

It is well known that colloidal processing technique allows improving the density of ceramic materials [37]. This technique is a suitable method to prepare powders with more adequate distribution of the second phase in the matrix without tendency to agglomerate, which at the end has influence in the sintering and densification of the composites. This way, lower density may be attributed to the presence of pores in the sintered samples, which is controlled in the colloidal processing route by eliminating agglomerates. Therefore, agglomerates in suspension cause the non-homogenous densification of grains during sintering and result in pore and crack formation after sintering [38]. Other mechanisms as the shortening of diffusional paths [39,40] also promote the densification as well as the stronger bonding of the chromium (carbide) with the graphite during the sintering, which results in better mechanical properties but also thermal and electrical properties. Researchers suggest that densification rates >85% are difficultly attained in the case of graphitic materials [41]. The presence of liquid phase is other mechanism that leads to an improvement of the densification rate above this 85%, while the colloidal synthesis allowed a further improvement resulted from the more suitable distribution of the chromium carbide within the graphite matrix.

Microstructural characterization using scanning electron microscope was carried out on fracture surface, where chromium carbide appears in white colour while graphite appears in black/dark grey colour. Images of sintered samples at the five temperatures of sintering (1600, 1700, 1800, 1900 and 2000 °C) are collected in Fig. 1 for the specimens of mechanical mixing of powders in roller mill and in Fig. 2 for the samples obtained by colloidal processing route. These images allow anticipating the subsequent properties of the composite. It is possible to see in Fig. 1

Table 1
Values of the relative density for the composites obtained by mechanical mixing of powders and colloidal processing route.

Temperature (°C)	MM-relative density (%)	SC-relative density (%)
2000	89.46	91.40
1900	87.42	93.57
1800	85.44	88.31
1700	82.33	85.06
1600	80.10	80.42

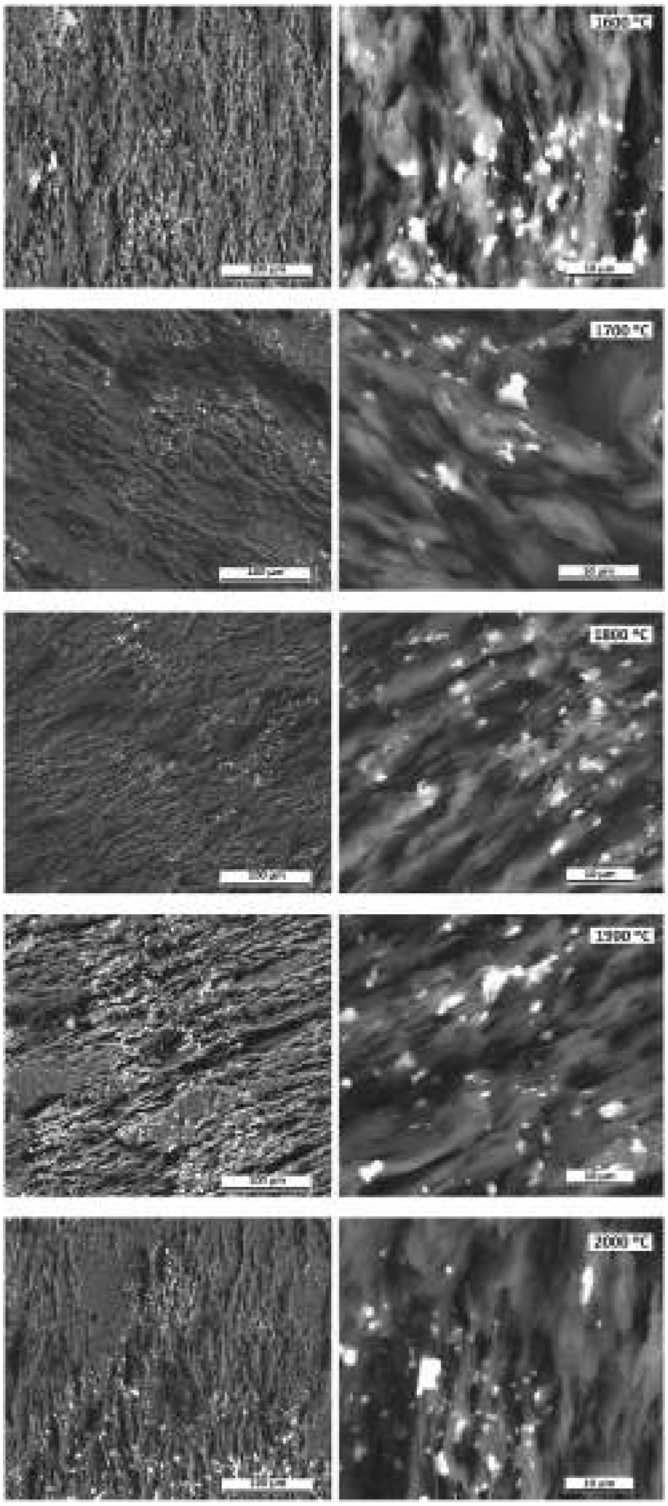

Fig. 1. Micrographs of sintered samples at different temperatures obtained by mechanical mixing of powders of chromium and graphite in roller mill. Micrographs were taken at 800x and 6000x magnification on surface of fracture specimens.

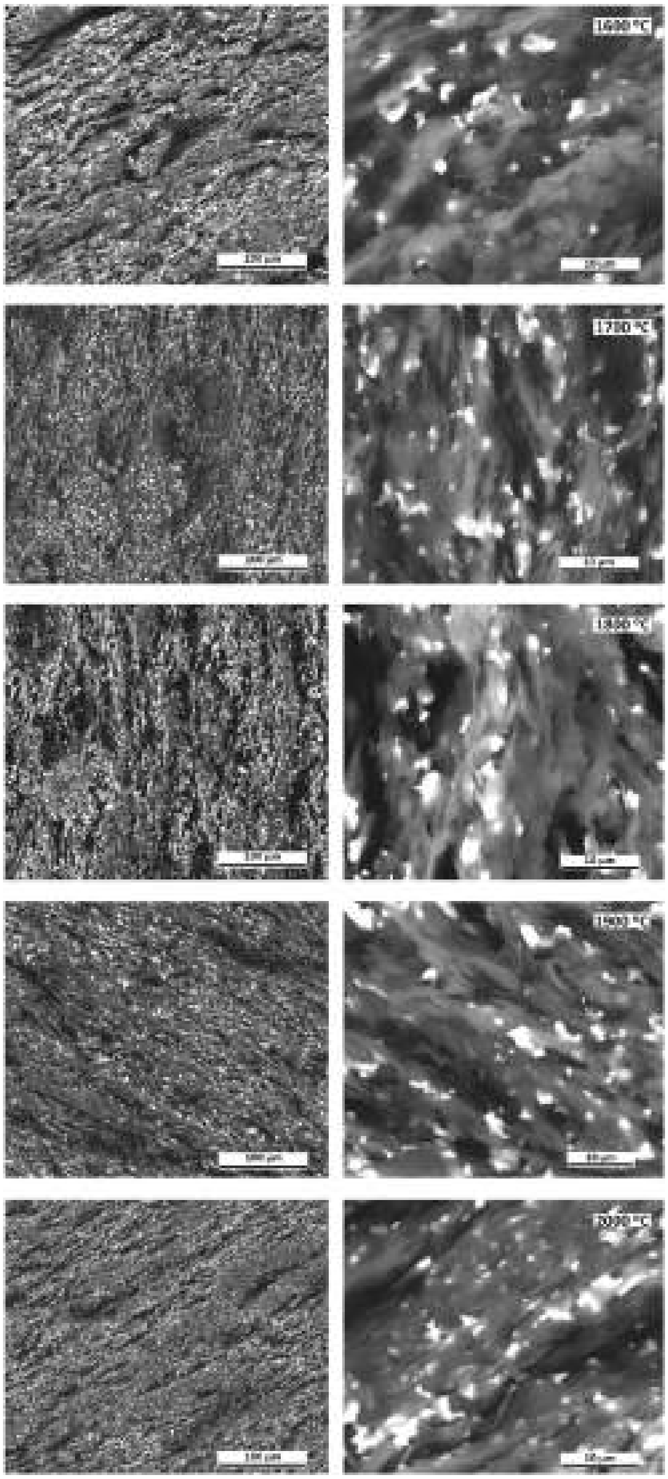

Fig. 2. Micrographs of sintered samples at different temperatures obtained by colloidal processing route from graphite and hexahydrate chromium (III) chloride as precursor of chromium. Micrographs were taken at 800x and 6000x magnification on surface of fracture specimens.

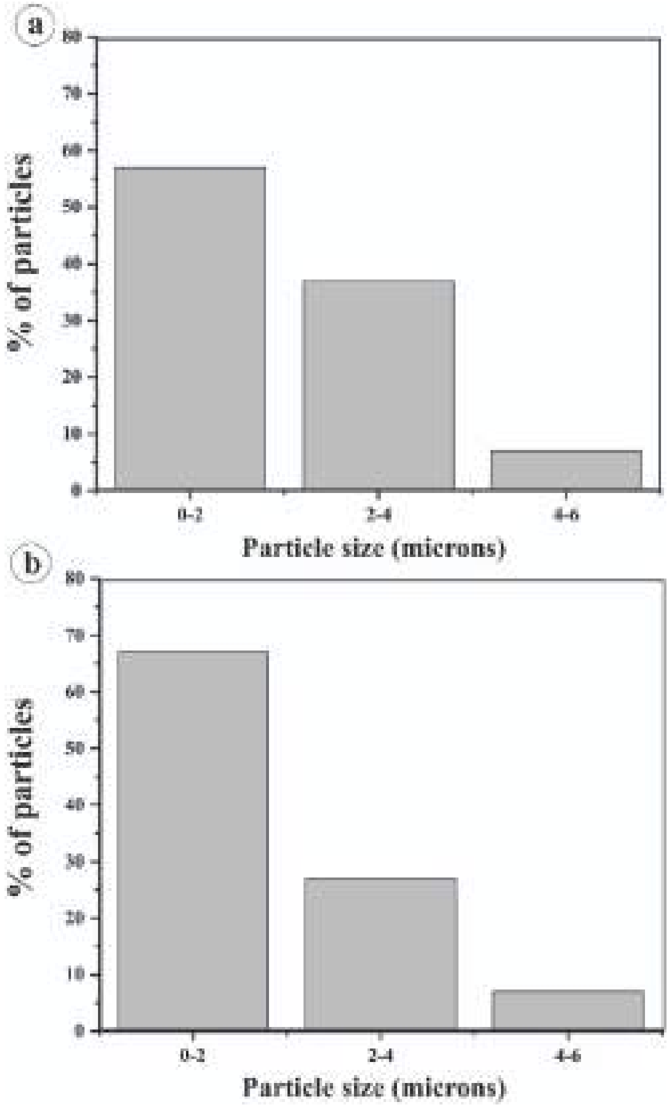

Fig. 3. Particle size distribution once sintered: (a) mechanical mixing of powders; (b) colloidal route.

that mechanical mixing in roller mill did not allow a suitable mixing of the original components since there are zones with more concentration of chromium carbide particles and others depleted in the carbide. On the contrary, Fig. 2, corresponding to powders obtained by colloidal processing route ensured that chromium (chromium carbides once sintered) appears homogeneously distributed within the matrix of graphite (there are neither zones with a greater concentration of chromium carbide nor other zones depleted in this phase). Micrographs are also useful to corroborate the formation of liquid phase during the sintering process. It is possible to see that chromium carbides appear surrounding the graphite grains, located at triple points and grain boundaries, particularly visible in the right column of Figs. 1 and 2. The orientation of graphite planes in the perpendicular direction to the pressing is also anticipated in these images. Moreover, the size distribution was analysed using image analysis software and distribution of the particles according to the size was elaborated (Fig. 3). It is possible to check that the chromium carbide particle size is homogeneous, mostly <4 μm in both routes, although the colloidal route allows obtaining a greater number of particles in the range <2 μm. Nevertheless, it is possible to see in Fig. 1 that there is not a smooth distribution of the particles within the matrix, which tend to concentrate in certain zones of the composite. The distribution of the particles in the matrix was analysed using imageJ software. Results are collected in Table 2 for each sintering temperature in samples obtained by colloidal processing route and by mechanical mixing of powders. Each micrograph was divided into three slides of the same dimensions to count the number of particles (each slide should account for 33.33% of the particles). It is numerically observed that the number of particles is more homogeneous in the samples processed by colloidal synthesis (mean standard deviation: 2.8) than in those

Table 2
Number of particles depending on the powder processing method, micrographs taken at the same magnification.

Temperature of sintering	Mechanical mixing			Colloidal synthesis		
1600 (total)	1589			1887		
1600 (slides)	398 (25.04%)	628 (39.52%)	563 (35.43%)	672 (35.61%)	634 (33.60%)	581 (30.79%)
1700 (total)	516			3404		
1700 (slides)	69 (13.37%)	202 (39.15%)	248 (48.06%)	1223 (35.93%)	1136 (33.37%)	1045 (30.70%)
1800 (total)	478			3518		
1800 (slides)	74 (15.48%)	215 (44.98%)	189 (39.54%)	1170 (33.26%)	1250 (35.53%)	1098 (31.21%)
1900 (total)	2409			2604		
1900 (slides)	631 (26.19%)	903 (37.48%)	875 (36.32%)	794 (30.49%)	808 (31.03%)	1002 (38.48%)
2000 (total)	1140			5292		
2000 (slides)	252 (22.11%)	576 (50.53%)	312 (27.37%)	1790 (33.82%)	1870 (35.34%)	1632 (30.84%)

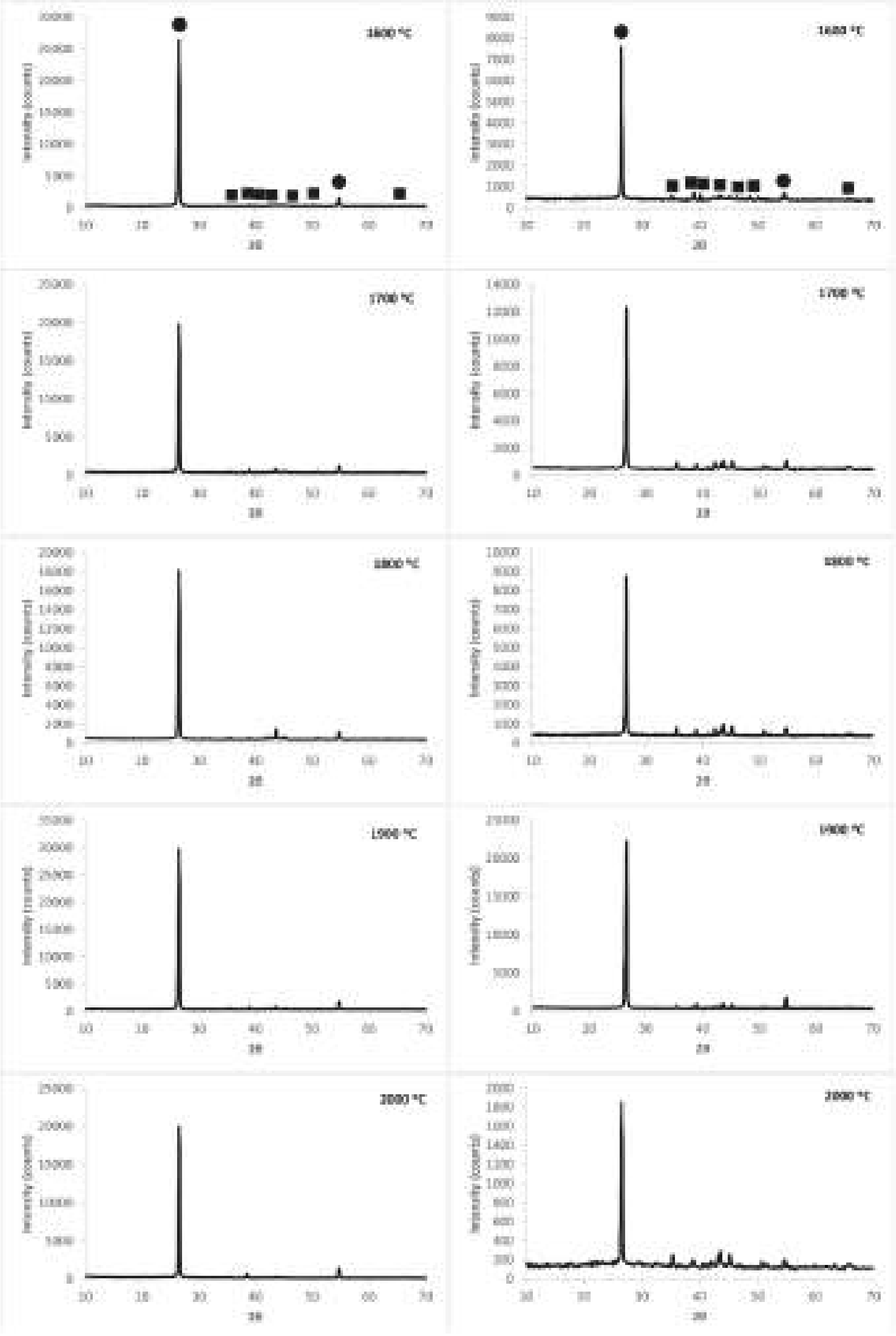

Fig. 4. X-ray diffraction patterns of the samples consisting of graphite-7 vol. % Cr previously uniaxially pressed at 60 MPa and then SPS sintered at different temperatures. Left column corresponds to the route involving mechanical mixing of powders and right column belongs to the route of colloidal synthesis.

obtained by mechanical mixing of powders (mean standard deviation: 12.5), thus corroborating that the colloidal route is more adequate in terms of improving the distribution of the particles of carbide in the matrix of graphite.

3.2. X-ray diffraction

Samples were subjected to X-ray diffraction analyses. The X-ray diffraction patterns are collected in Fig. 4(a) for the samples obtained by the route mechanical mixing and sintering in the spark plasma sintering apparatus, while Fig. 4(b) collects the samples of the route involving the colloidal processing technique to process the powders. There are not differences in one or other route in terms of composition. Therefore, the sintering temperature does not have an evident influence on the phase composition after the sintering process since the phases after the sintering process in the SPS are in all the cases graphite and Cr_3C_2. It is possible to see that carbides are formed by reaction of the graphite (solid) and chromium (liquid), as there is a peritectic reaction at 1811 °C in the chromium-carbon diagram (chromium carbide is also formed when sintering at 1600 °C due to the influence of the combined application of pressure and vacuum conditions). During this process, atoms of carbon dissolve in the liquid phase and diffuse and react with the chromium to form chromium carbides that during the solidification result, according to the peritectic reaction in the carbon-chromium diagram, into Cr_7C_3+Cr_3C_2, although the excess of carbon composition and unimpeded diffusion of the carbon leads the system to move towards the Cr_3C_2+C zone. For that reason, Cr_3C_2 and carbon are the main constituents that can be identified during the X-ray diffraction analyses.

The process is different in the case of the powders prepared by colloidal processing route. X-ray diffraction patterns are collected in Fig. 5. The sample before the treatment in muffle furnace does not experience any chemical transformation: it consists of graphite and hexahydrate chromium (III) chloride. After heating in the muffle furnace at 450 °C, it is possible to find chromium oxide and graphite (Fig. 5(a)). The formation of the chromium oxide from the precursor was described by Carthers [42], and reactions are those indicated below:

$$2CrCl_3{\cdot}6H_2O\ (l) \rightarrow (CrCl_3)_2{\cdot}3H_2O\ (s) + 9H_2O\ (g) \tag{4}$$

$$(CrCl_3)_2{\cdot}3H_2O\ (s) \rightarrow Cr_2OCl_4{\cdot}2H_2O\ (s) + 2HCl\ (g) \tag{5}$$

$$Cr_2OCl_4{\cdot}2H_2O\ (s) \rightarrow Cr_2O_3\ (s) + 4HCl\ (g) \tag{6}$$

Later, during the sintering process in the spark plasma sintering apparatus, chromium (III) oxide is reduced in presence of the graphite. The mechanism of reduction and formation of chromium carbide is complex as it involves numerous intermediate reactions that can be summarized in the following:

$$6Cr_2O_3\ (s) + 17C\ (s) \rightarrow 4Cr_3C_2\ (s) + 9CO_2\ (g) \tag{7}$$

Once formed the chromium, the process progresses as in the other case, and finally there is Cr_3C_2 after the sintering process. Gases formed during the process in the spark plasma apparatus are released due to the pressure and vacuum applied during the process that allows the gas to flow out of the sample.

X-ray diffraction technique is a useful technique to determine the anisotropy of the composite. Therefore, the X-ray spectra were obtained in the in-plane and through-plane directions using 2θ continuous scanning method at a scanning rate of 1°/min, within the range 5°–70° [43] (Fig. 6). A parameter called D_α was calculated by means of equation (8) with the values of intensity of the peaks corresponding to the planes (0 0 2) (2θ) and (1 0 0).

$$D_\alpha = \frac{I_{100}}{I_{100} + I_{002}} \tag{8}$$

The peaks corresponding to the planes (0 0 2) and (1 0 0) appear in the angles 27° (19,821 counts in the in-plane direction and 424 counts in the through-plane direction, for mechanical mixing; 21,979 counts in the in-plane direction and 1036 counts in the through-plane direction, for colloidal route) and 42° (261 counts in the in-plane direction and 198 counts in the through-plane direction, for mechanical mixing; 596 counts in the in-plane direction and 460 counts in the through-plane direction, for colloidal route).

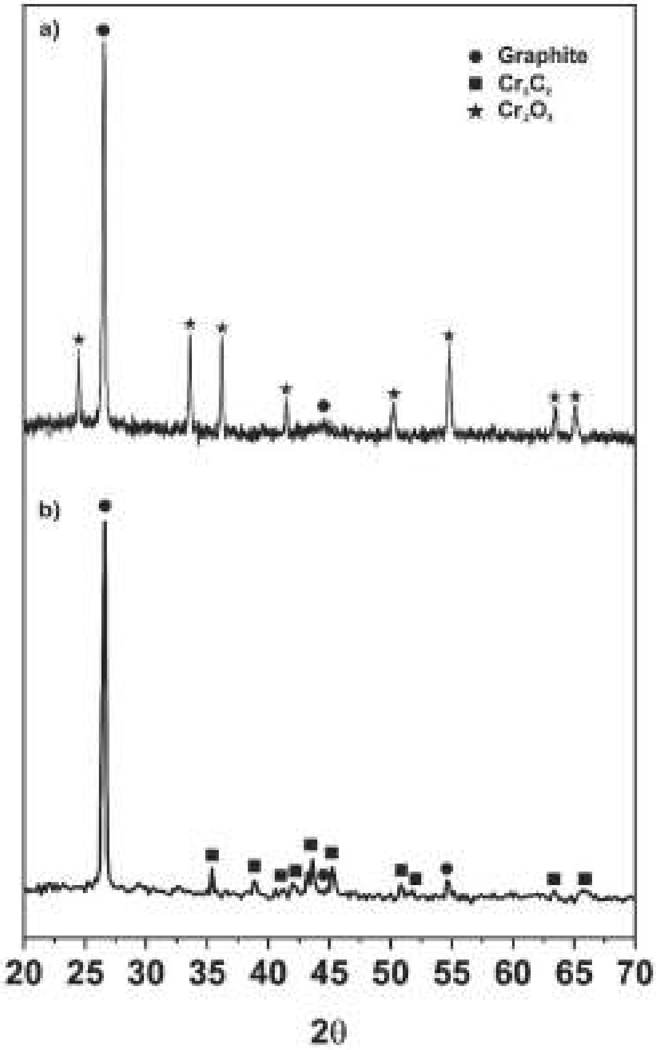

Fig. 5. X-ray diffraction pattern of the sample graphite-7 vol. % Cr: (a) after treatment at 450 °C in muffle; (b) sintered sample at 1900 °C-20 min, from colloidal synthesis powders.

The values of the D_α (⊥), corresponding to the in-plane X-ray diffractogram, and D_α (‖), corresponding to the through-plane diffractogram, are 0.3183 and 0.0123 (MM) and 0.3074 and 0.0264 (SC), respectively. The anisotropy ratio is calculated as the relation between the D_α (⊥), and D_α (‖), as D_α (⊥)/ D_α (‖). The values are 25.88 and 11.64 for the mechanical mixture of powders and colloidal synthesis routes, which indicates the clear anisotropic behaviour of graphite–chromium composites, because the greater the value the more anisotropic the material is.

3.3. Electrical conductivity

Electrical conductivity was measured in the in-plane direction. Results are collected in Fig. 7. As electrical conductivity in the through-plane direction cannot be measured, it is assumed that in this direction the value is < 0.1 MS/m, which is supported by other experimental works in composites of the graphite-metal system [33,34]. Oriented

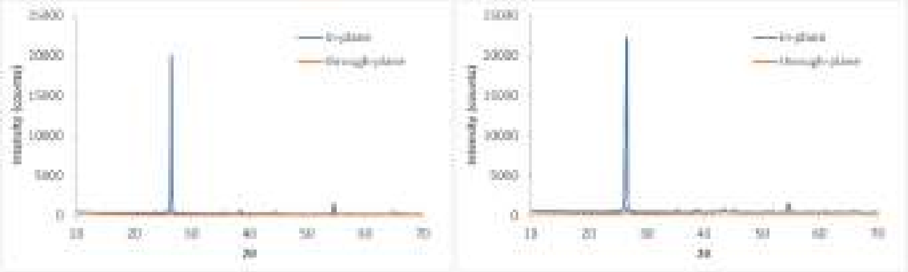

Fig. 6. X-ray diffractometer spectra of the sintered specimen graphite–7 vol% Cr in the in-plane (blue) and through-plane (orange) directions: (a) mechanical mixing of powders; (b) colloidal processing route. (For interpretation of the references to colour in this figure legend, the reader is referred to the Web version of this article.)

graphite exhibit, as it was already reported, anisotropic behaviour with respect to the electrical conductivity, i. e. natural graphite crystals can manifest values of electrical conductivity as high as 2.4 MS/m in the basal plane while in the perpendicular direction the value is usually 1 or 2 orders of magnitude smaller [44]. Other researchers indicate that the electrical conductivity in-plane of the graphite is around 1 MS/m [45]. However, the addition of metals does not allow reaching values as high as those obtained for the crystal of graphite, but other researchers have observed that sintering graphite without the addition of metals do not report values > 0.1 MS/m [33,34] it does not matter the direction. This is related with the sintering of graphite. Graphite has a very high melting point, and this involves that the sintering of this material without the support of a second phase is very complex as it should take place by solid-state sintering, by diffusion mechanisms. This explains that low values of relative density are obtained, while in common ceramics, it is possible to reach values of relative density approaching 100%. The sintering of graphite is usually accompanied by a second metallic phase, which bonds together the graphite particles with the second phase (metal or metal carbides) and provides continuity (referred to less pores and greater homogeneity, and stronger bonding of particles) of properties to the composite, which is translated into the characteristics of the composite. In the case of sintering only graphite particles, there is not this strong bond and continuity in the composite, which impedes to reach the values of electrical, thermal, and mechanical properties measured in the crystal of graphite.

Considering the case of the electrical conductivity, that of the chromium (II) carbide is 13.33 MS/m [46], while that of the graphite crystals in the in-plane direction was around 1-2.4 MS/m [41,42]. Thus, the electrical conductivity of the composite is close to that of the crystal of graphite (it is necessary to consider that the effect of the applied pressure is to promote the orientation of the graphite lamellae in the in-plane direction) with the continuity to the composite provided by the carbide and reduced by interfacial resistance in the points where there is not graphite-carbide contact, as the graphite-air interface is insulating [47]. Therefore, it was possible to find in the case of composites of the same family (graphite-molybdenum) composites with values of the electrical conductivity of around 1 MS/m: 0.88–1.01 MS/m in-plane by Guardia-Valenzuela et al. [32]; 0.86 MS/m in-plane by Suárez et al. [33]; or, 0.99 MS/m in-plane by Suárez et al. [34]. In the case of graphite-chromium composites with 7 vol % chromium obtained by spark plasma sintering, the electrical conductivity is as high as 0.75 MS/m. There are significant differences in the electrical conductivity depending on the method of processing powders, as for the same temperature, in the case of SC-1900 °C (0.75 MS/m) and MM-1900 °C (0.58 MS/m), the electrical conductivity is a 30% greater (Table 2). This difference is only evident at this temperature while for the rest of the temperatures, the values are slightly better for the composites prepared by colloidal processing route, probably associated to the slightly better densification. This better electrical conductivity for the composite SC-1900 °C is consistent with the excellent distribution of the chromium carbide within the graphite matrix, but particularly by the greatest value of relative density in this case. It is necessary to take into account that the zones with few chromium in Fig. 1 represent areas with few strong graphite-carbide bonds, which are those that provide the continuity for the electrical conductivity of the composite.

3.4. Thermal conductivity

Thermal conductivity was calculated by means of Eq. (3) in the

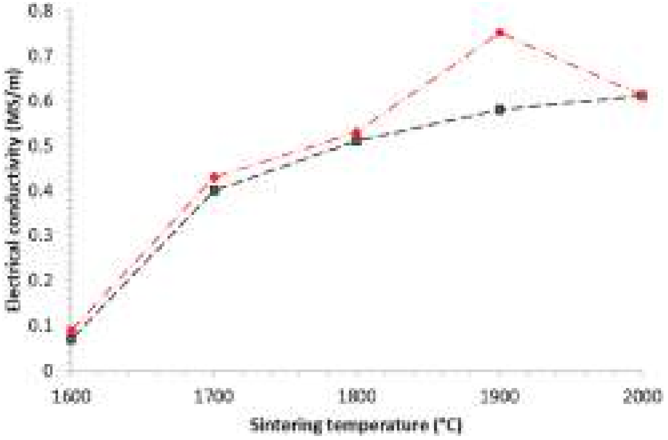

Fig. 7. Electrical conductivity of the composites obtained by mechanical mixing of powders (black) and colloidal processing route (red) (measured in the in-plane direction) (±5%, maximum deviation from the mean value). (For interpretation of the references to colour in this figure legend, the reader is referred to the Web version of this article.)

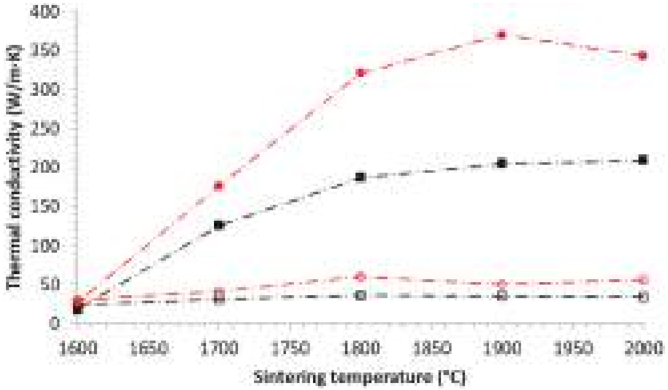

Fig. 8. Thermal conductivity of the composites obtained by mechanical mixing of powders (black: in-plane, square; through-plane, empty square) and colloidal processing route (red: in-plane, circle; through-plane, empty square) (±5%, maximum deviation from the mean value). (For interpretation of the references to colour in this figure legend, the reader is referred to the Web version of this article.)

through-plane direction. Results are collected in Fig. 8. The values of the thermal conductivity in the in-plane direction were indirectly determined by the Wiedemann-Franz law, with the best values of thermal conductivity for the SC-1900 °C of 370 W/m K and MM-2000 °C of 209 W/m K (analogous to that of the MM-1900 °C of 205 W/m K). Values of the thermal conductivity are comparable to those obtained by Guardia-Valenzuela et al. [32] (in-plane, 647−740 W/m K; through-plane, 56−50 W/m K), Suárez et al. [33] (in-plane, 136.68 W/m K; through-plane, 22.09 W/m K) and Suárez et al. [34] (in-plane, 201.49 W/m K; through-plane, 23.43 W/m K) for graphite-molybdenum-titanium composites, which are composites of the same family (graphite-transition metal of the group VI). There are clear differences in the thermal conductivity, apart from the measured direction, between powders obtained by mechanical mixing in the roller mill and by colloidal processing route. This difference can be attributed first to the densification of the composites. Within this line, it is possible to see that the tendency followed by the thermal conductivity is the same that the densification. Besides, it was already reported that the densification improves with the powder processing method supported by the more homogeneous distribution of the chromium carbides within the graphite matrix, which contributes to tightly bound the graphite lamellae in a denser composite. Literature reports that chromium (II) carbide has a thermal conductivity of 189.77 W/m·K [48] while highly oriented pyrolytic graphite can exhibit values of thermal conductivity as high as 1910 W/m·K [49] in-plane direction or within 1500 and W/m·K according to other authors [50]. Here the situation is the same than that observed in the case of the electrical conductivity. The presence of graphite-graphite contacts inadequately bonded as a result of the solid phase sintering at these points produce a resistance in the conduction of heat, which translates to the values of the thermal conductivity collected in Fig. 8. As the chromium (II) carbide is more homogeneously distributed in the case of the samples obtained by colloidal processing route, there are less graphite-graphite contacts and, on the contrary, stronger graphite-chromium (II) carbide-graphite contacts are observed, which provide continuity for the heat flow and greater values of thermal conductivity.

3.5. Young's modulus

Young's modulus values are collected in Fig. 9. The young's modulus of the graphite sintered in the spark plasma sintering apparatus is around 22 GPa with relative densities that do not reach the 80%, which in the case of full compacts will reach around 30 GPa. On the other hand, the young modulus of the chromium (II) carbide is 373 GPa according to the reference [43]. Thus, the responsible of the higher young modulus of the composites (with respect to the graphite) is the chromium (II) carbide. The best value was obtained in the case of SC-1900 °C with 51.4 GPa, although there are not significant differences in this route for the samples SC-1800 °C and SC-2000 °C. In the case of the mechanical mixing of powders, the best value is obtained a 1900 °C, although there is not a significant difference when the sintering temperature is > 1700 °C, with changes mainly associated with the measurement method. The improvement in the value of this parameter in the case of the composites obtained by colloidal processing technique is related at certain extent with the relative density of the composite, as the values of the young modulus follow the same trend that the values of the relative density. In order to explain the differences between the composites obtained by mechanical mixing of powders and those obtained by colloidal processing technique, it is necessary to consider the microstructural differences, mainly related with the segregation, with zones clearly enriched in chromium carbide and others depleted of this phase. The simultaneous application of pressure and temperature in the SPS machine produces a segregation (by extrusion) of the second phase towards periphery of the samples, leading to further loses of chromium carbides in the samples processed at higher temperature due to the increased fluidity of this liquid phase during the sintering process. Therefore, when extracting specimens for measurement of young's modulus, the value of this property, which increases with the chromium carbide content, decreases as further chromium carbide is lost as the fluidity of the sample increases. This change is small due to the small differences in the chromium carbide content produced as the temperature of sintering is increased. As it is possible to check in Fig. 9, there is a plateau in 50 GPa for the sample obtained by colloidal synthesis and 40 GPa for the sample processed by mechanical mixing of powders when the temperature is increased above 1700 °C.

3.6. Flexural strength

The values of the flexural strength are collected in Fig. 10. It is possible to see an evident improvement of the bending strength when the powders are processed by colloidal processing route (the best value is obtained in the sample SC-1900 °C with 117.5 MPa, while in the other route is measured in the sample MM-2000 °C with 55.8 MPa). If the microstructural analysis is considered here, the presence of zones enriched in chromium carbide and other zones depleted in this compound lead to zones where there is not the strong bonding provided by the chromium carbides and the material can fail in these zones more easily. This is consistent with the literature as, for instance, graphite exhibits a flexural strength of around 25-50 MPa without additives [51,

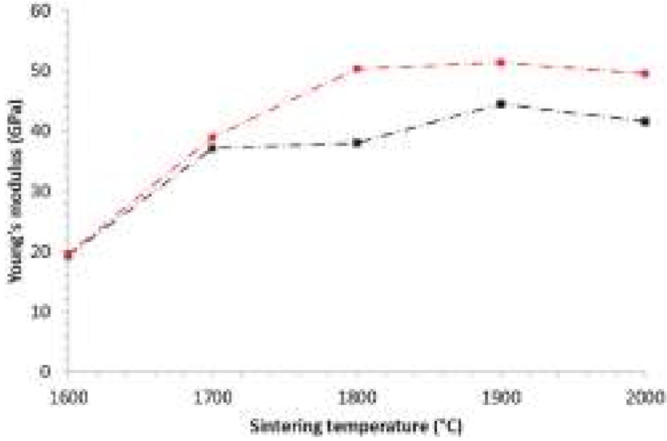

Fig. 9. Young's modulus of the composites obtained by mechanical mixing of powders (black) and colloidal processing route (red) (±10%, maximum deviation from the mean value). (For interpretation of the references to colour in this figure legend, the reader is referred to the Web version of this article.)

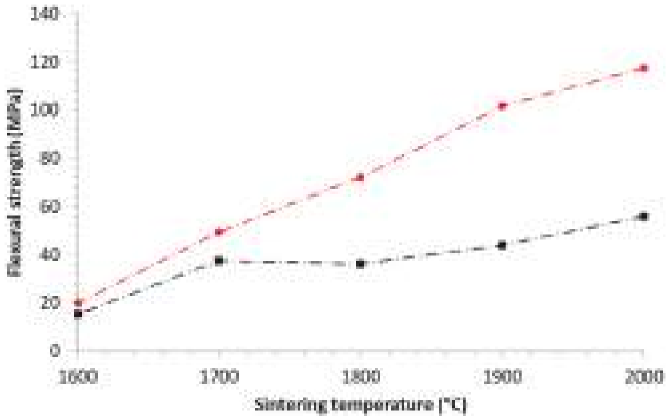

Fig. 10. Flexural strength of the composites obtained by mechanical mixing of powders (black) and colloidal processing route (red) (±12%, maximum deviation from the mean value). (For interpretation of the references to colour in this figure legend, the reader is referred to the Web version of this article.)

52] and can reach 100 MPa in the case of using a reinforcing metal [53].

3.7. Potential use of the composite in heat sinks: Coefficient of thermal expansion

The composite of this paper could find potential application in heat dissipation. Ekpu and colleagues pointed out in 2011 [54] four criteria for the selection of the suitable composites for heat sinks in electronic devices: thermal conductivity (some researchers remark the importance of values > 300 W/m·K for future electronic devices [55]), density, cost, and coefficient of thermal expansion (low value is expected for materials used in heat dissipation [55]). Nowadays, heat dissipation is habitually carried out using aluminium and copper, which provide values of thermal conductivity (W/m·K), density (g/cm^3), coefficient of thermal expansion (K^{-1}) and cost (€/ton, although the cost of the composite will depend, apart from the material price, on the process and some other variables as the material quality), respectively: 247, 2.7, 21-24 and around 2500, for the aluminium, and 398, 8.96, 16-16.7 and around 8000, for the copper. These values are sufficient for certain heat dissipation applications, although aluminium and copper have certain limitations, so research is carried out in diamond-copper [56], diamond-aluminium [57] composites (due to the great thermal conductivity of the diamond, around 2200 W/m·K, the high cost and availability are serious concern), or graphite-aluminium [58] and graphite-copper [59], which overcome the problem of the diamond cost. The best composite obtained in this research, graphite-7 vol. % Cr, which is that obtained by colloidal processing route (pressed at 60 MPa to obtain green compacts and sintered in SPS at 1900 °C under an applied pressure of 30 MPa and vacuum conditions), has a thermal conductivity in the in-plane direction of 370.1 W/m·K and a density of 2.48 g/cm^3, with a cost that could be competitive with that of the copper- and aluminium-based composites because the graphite price depends on the quality but is lower than 3000 €/ton, although the use of spark plasma sintering technique in the manufacture process could increase the price. The coefficient of thermal expansion is important and, in this case, the values in the in-plane and through-plane directions are $3.20 \cdot 10^{-6}$ K^{-1} and $8.85 \cdot 10^{-6}$ K^{-1}, respectively. These values of coefficient of thermal expansion are at least half that of the copper and 1/3 that of the aluminium, which would make this composite adequate for the demanding requirements of coefficient of thermal expansion in miniaturized electronic devices. Therefore, results suggest that graphite-chromium composites could be an interesting alternative in the manufacture of heat sinks for electronic devices or other equipment used with the aim of dissipating heat energy.

4. Conclusions

This manuscript has reported a study of novel graphite-chromium composites. The research evaluated the influence of the powder processing method on the thermal, electrical, and mechanical properties of the composite graphite-7 vol. % chromium: mechanical mixing of raw materials powders in roller mill and colloidal processing route. Moreover, the influence of the sintering temperature in the spark plasma sintering apparatus was also studied for both methods: 1600, 1700, 1800, 1900 and 2000 °C.

Results are different for both types of powders' processing techniques regarding the relative density, electrical conductivity, thermal conductivity, young modulus, and flexural strength (measured in the in-plane direction). These properties strongly depend on the microstructure of the composites, that is to say, on the distribution of the second phase (chromium (III) carbide) on the matrix of graphite. It appears more homogeneously distributed in the case of the colloidal synthesis than in the case of the simple mechanical mixing of the powders in a roller mill. This reflects on the properties of the composite, which are always better in the composites obtained by colloidal synthesis at each temperature. The composite with the best properties was obtained by colloidal synthesis and sintering at 1900 °C in the spark plasma sintering apparatus, with 93.57%, 0.7509 MS/m, 370.1 W/m·K, 51.4 GPa and 117.5 MPa, respectively. Regarding the coefficient of thermal expansion, which is important for the integration of the heat dissipator in the device, it takes values in-plane and through-plane directions of $3.20 \cdot 10^{-6}$ K^{-1} and $8.85 \cdot 10^{-6}$ K^{-1}, respectively. Sintering samples obtained by colloidal synthesis at 1800 °C provides properties even better than the best sample obtained by mechanical mixing of powders (at 2000 °C), which suggests that sintering temperature could be reduced in the case of using colloidal processing technique.

Considering all the above, colloidal processing route used to obtain powders emerges as the best alternative to obtain graphite-chromium composites with excellent properties for heat dissipation applications.

Declaration of competing interest

The authors declare that they have no known competing financial interests or personal relationships that could have appeared to influence the work reported in this paper.

Acknowledgements

This research was funded by the Spanish Ministry of Science and Innovation. Call Programa Estatal de I+D+i Orientada a los Retos de la Sociedad [RTI2018-102269-B-I00].

This research was also supported by a Juan de la Cierva Formación grant from the Spanish Ministry of Science and Innovation (MCINN) to Daniel Fernández-González [FJC2019-041139-I].

Juan Piñuela Noval acknowledges the Programa “Severo Ochoa” of Grants for Research and Teaching of the Principality of Asturias for the funds received for the elaboration of the Ph. D. Thesis (Ref: BP20 041).

Authors are grateful to Ainhoa Macías San Miguel from Nanomaterials and Nanotechnology Research Center (CINN) for providing technical assistance.

References

[1] H.Y. Li, M.H. Chiang, C.I. Lee, W.J. Yang, Thermal performance of plate-fin vapor chamber heat sinks, Int. Commun. Heat Mass Tran. 37 (7) (2010) 731–738, https://doi.org/10.1016/j.icheatmasstransfer.2010.05.015.

[2] H. Rho, Y.S. Jang, H. Bae, A.-N. Cha, S.H. Lee, J.-S. Ha, Fanless porous Graphene-copper composite heat sink for micro devices, Sci. Rep. 11 (2021), 17607, https://doi.org/10.1038/s41598-021-97165-y.

[3] J.A. Pero-Sanz, D. Fernández-González, L.F. Verdeja, Structural Materials: Properties and Selection, first ed., Springer, Cham, Switzerland, 2019 https://doi.org/10.1007/978-3-030-26161-0.

[4] Th Schubert, T. Ciupinski, J. Morgiel, H. Weidmuller, T. Weissgarber, B. Kieback, Advanced Composite Materials for Heat Sink Applications, EuroPM, 2007.

[5] J.A. Pero-Sanz, D. Fernández-González, L.F. Verdeja, Physical Metallurgy of Cast Irons, first ed., Springer, Cham, Switzerland, 2018 https://doi.org/10.1007/978-3-319-97313-5.

[6] J.I. Verdeja, D. Fernández-González, L.F. Verdeja, Physical Metallurgy and Heat Treatment of Steel, first ed., Springer, Cham, Switzerland, 2023 https://doi.org/10.1007/978-3-031-05702-1.

[7] L.F. Verdeja, D. Fernández-González, J.I. Verdeja González, Operations and Basic Processes in Steelmaking, first ed., Springer, Cham, Switzerland, 2021 https://doi.org/10.1007/978-3-030-68000-8.

[8] J.I. Verdeja, D. Fernández-González, L.F. Verdeja, Operations and Basic Processes in Ironmaking, first ed., Springer, Cham, Switzerland, 2020 https://doi.org/10.1007/978-3-030-54606-9.

[9] Th Schubert, A. Brendel, K. Schmid, Th Koeck, L. Ciupinski, W. Zielinski, T. Weiβgärber, B. Kieback, Interfacial design of Cu/SiC composites prepared by powder metallurgy for heat sink applications, Composites Part A-Appl. S. 38 (2007) 2398–2403, https://doi.org/10.1016/j.compositesa.2007.08.012.

[10] X.-Y. Shen, X.-B. He, S.-B. Ren, H.-M. Zhang, X.-H. Qu, Effect of molybdenum as interfacial element on the thermal conductivity of diamond/Cu composites, J. Alloys Compd. 529 (2012) 134–139, https://doi.org/10.1016/j.jallcom.2012.03.045.

[11] L. Yang, L. Sun, W. Bai, L. Li, Thermal conductivity of Cu-Ti/diamond composites via spark plasma sintering, Diam. Relat. Mater. 94 (2019) 37–42, https://doi.org/10.1016/j.diamond.2019.02.014.

[12] Y.D. Kim, N.L. Oh, S.-T. Oh, I.-H. Moon, Thermal conductivity of W–Cu composites at various temperatures, Mater. Lett. 51 (5) (2001) 420–424, https://doi.org/10.1016/S0167-577X(01)00330-5.

[13] K.-M. Lee, D.-K. Oh, W.-S. Choi, T. Weissgärber, B. Kieback, Thermomechanical properties of AlN-Cu composite materials prepared by solid state processing, J. Alloys Compd. 434–435 (2007) 375–377, https://doi.org/10.1016/j.jallcom.2006.08.176.

[14] K. Chu, Z. Liu, Ch Jia, H. Chen, X. Liang, W. Gao, W. Tian, H. Guo, Thermal conductivity of SPS consolidated Cu/diamond composites with Cr-coated diamond particles, J. Alloys Compd. 490 (2010) 453–458, https://doi.org/10.1016/j.jallcom.2009.10.040.

[15] M. Prakasam, A. Morvan, C. Azina, L. Constantin, G. Goglio, A. Largeteau, S. Bordère, J.-M. Heintz, Y. Lu, J.-F. Silvain, Ultra-low temperature fabrication of copper carbon fibre composites by hydrothermal sintering for heat sinks with enhanced thermal efficiency, Comps. Part A-Appl. S. 133 (2020), 105858, https://doi.org/10.1016/j.compositesa.2020.105858.

[16] G. Bai, N. Li, X. Wang, J. Wang, M.J. Kim, H. Zhang, High thermal conductivity of Cu-B/diamond composites prepared by gas pressure infiltration, J. Alloys Compd. 735 (2018) 1648–1653, https://doi.org/10.1016/j.jallcom.2017.11.273.

[17] J. Li, X. Wang, Y. Qiao, Y. Zhang, Z. He, H. Zhang, High thermal conductivity through interfacial layer optimization in diamond particles dispersed Zr-alloyed Cu matrix composites, Scripta Mater. 109 (2015) 72–75, https://doi.org/10.1016/j.scriptamat.2015.07.022.

[18] V. Oddone, B. Boerner, S. Reich, Composites of aluminum alloy and magnesium alloy with graphite showing low thermal expansion and high specific thermal conductivity, Sci. Technol. Adv. Mater. 18 (1) (2017) 180–186, https://doi.org/10.1080/14686996.2017.1286222.

[19] E. Jansen, O. Dorsch, E. Obermeier, W. Kulisch, Thermal conductivity measurements on diamond films based on micromechanical devices, Diam. Relat. Mater. 5 (1996) 644–648, https://doi.org/10.1016/0925-9635(95)00404-1.

[20] B.J.M. Hausmann, M. Khan, Y. Zhang, T.M. Babinec, K. Martinick, M. McCutcheon, P.R. Hemmer, M. Lončar, Fabrication of diamond nanowires for quantum information processing applications, Diam. Relat. Mater. 19 (2010) 621–629, https://doi.org/10.1016/j.diamond.2010.01.011.

[21] J.E. Graebner, Thermal conductivity of diamond, in: L.S. Pan, D.R. Kania (Eds.), Diamond: Electronic Properties and Applications. The Kluwer International Series in Engineering and Computer Science, Springer, Boston, MA, 1995, https://doi.org/10.1007/978-1-4615-2257-7_7.

[22] S.V. Kidalov, F.M. Shakhov, Thermal conductivity of diamond composites, Materials 2 (2009) 2467–2495, https://doi.org/10.3390/ma2042467.

[23] K. Yoshida, H. Morigami, Thermal properties of diamond/copper composite material, Microelectron. Reliab. 44 (2004) 303–308, https://doi.org/10.1016/S0026-2714(03)00215-4.

[24] M. Battabyal, O. Beffort, S. Kleiner, S. Vaucher, L. Rohr, Heat transport across the metal-diamond interface, Diam. Relat. Mater. 17 (2008) 1438–1442, https://doi.org/10.1016/j.diamond.2008.01.023.

[25] A.A. Balandin, S. Ghosh, W. Bao, I. Calizo, D. Teweldebrhan, F. Miao, C.N. Lau, Superior thermal conductivity of single-layer graphene, Nano Lett. 8 (2008) 902–907, https://doi.org/10.1021/nl0731872.

[26] H. Malekpour, K.-H. Chang, J.-C. Chen, C.-Y. Lu, D.L. Nika, K.S. Novoselov, A. A. Balandin, Thermal conductivity of graphene laminate, Nano Lett. 14 (2014) 5155–5161, https://doi.org/10.1021/nl501996v.

[27] S. Ghosh, I. Calizo, D. Teweldebrhan, E.P. Pokatilov, D.L. Nika, A.A. Balandin, W. Bao, F. Miao, C.N. Lau, Extremely high thermal conductivity of graphene: prospects for thermal management applications in nanoelectronic circuits, Appl. Phys. Lett. 92 (2008), 151911, https://doi.org/10.1063/1.2907977.

[28] S. Chen, Q. Wu, C. Mishra, J. Kang, H. Zhang, K. Cho, W. Cai, A.A. Balandin, R. S. Ruoff, Thermal conductivity of isotopically modified graphene, Nat. Mater. 11 (2012) 203–207, https://doi.org/10.1038/nmat3207.

[29] F. Nazeer, Z. Ma, L. Gao, F. Wang, M.A. Khan, A. Malik, Thermal and mechanical properties of copper-graphite and copper-reduced graphene oxide composites, Compos. Part. B-Eng. 163 (2019) 77–85, https://doi.org/10.1016/j.compositesb.2018.11.004.

[30] M. Inagaki, F. Kang, M. Toyoda, H. Konno, Chapter 16 – highly oriented graphite with high thermal conductivity, in: Advanced Materials Science and Engineering of Carbon, Butterworth-Heinemann, London, 2014, pp. 363–386.

[31] J. White, J. Pontelandolfo, Graphite-carbide materials prepared by hot-working with the carbide phase, Carbon 4 (1966) 307–314, https://doi.org/10.1016/0008-6223(66)90043-1.

[32] J. Guardia-Valenzuela, A. Bertarelli, F. Carra, N. Mariani, S. Bizzaro, R. Arenal, Development and properties of high thermal conductivity molybdenum carbide - graphite composites, Carbon 135 (2018) 72–84, https://doi.org/10.1016/j.carbon.2018.04.010.

[33] M. Suárez, D. Fernández-González, L.A. Díaz, A. Borrell, J.S. Moya, A. Fernández, Synthesis and processing of improved graphite-molybdenum-titanium composites by colloidal route and spark plasma sintering, Ceram. Int. 47 (21) (2021) 30993–30998, https://doi.org/10.1016/j.ceramint.2021.07.267.

[34] M. Suárez, D. Fernández-González, C.F. Gutiérrez-González, L.A. Díaz, A. Borrell, J. S. Moya, R. Torrecillas, A. Fernández, Effect of green body density on the properties of graphite-molybdenum-titanium composite sintered by spark plasma sintering, J. Eur. Ceram. Soc. 42 (5) (2022) 2048–2054, https://doi.org/10.1016/j.jeurceramsoc.2021.12.073.

[35] M. Suárez, D. Fernández-González, L.A. Díaz, J. Piñuela-Noval, A. Borrell, J. S. Moya, R. Torrecillas, A. Fernández, Effect of Mo content on the properties of graphite–MoC composites sintered by spark plasma sintering, Bol. Sc. Esp. Ceram. V. (2023), https://doi.org/10.1016/j.bsecv.2023.02.005. In press.

[36] J. Piñuela-Noval, D. Fernández-González, M. Suárez, L.A. Díaz, L.F. Verdeja, A. Fernández, Characterization of graphite-chromium carbide composites manufactured by Spark Plasma Sintering, J. Am. Ceram. Soc. 106 (9) (2023) 5157–5166, https://doi.org/10.1111/jace.19145.

[37] R. Moreno, Better ceramics through colloid chemistry, J. Eur. Ceram. Soc. 40 (3) (2020) 559–587, https://doi.org/10.1016/j.jeurceramsoc.2019.10.014.

[38] C.H. Chin, A. Muchtar, C.H. Azhari, M. Razali, M. Aboras, Improvement of colloidal stability in colloidal processing for highly translucent, nanosized zirconia, Sains Malays. 47 (7) (2018) 1591–1597, https://doi.org/10.17576/jsm-2018-4707-30.

[39] L. Jiang, Y. Liao, Q. Wan, W. Li, Effects of sintering temperature and particle size on the translucency of zirconium dioxide dental ceramic, J. Mater. Sci. Mater. Med. 22 (11) (2011) 2429–2435, https://doi.org/10.1007/s10856-011-4438-9.

[40] J.R. Groza, Nanosintering. Nanostruct. Mater. 12 (5–8) (1999) 987–992, https://doi.org/10.1016/S0965-9773(99)00284-6.

[41] J.A. Aguiar, S. Kwon, B.D. Coryell, E. Eyerman, A.A. Bokov, R.H.R. Castro, D. Burns, H.T. Hartmann, E.P. Luther, Densification of graphite under high pressure and moderate temperature, Mater. Today 22 (2020), 100821, https://doi.org/10.1016/j.mtcomm.2019.100821.

[42] R.E. Cathers, A Study of the Carbothermal Decomposition of Some Hydrated Coordination Compouds, Dissertation in Chemistry for the Degree of Doctor of Philosophy, Faculty of Texas Technological College, May 1966. https://ttu-ir.tdl.org/bitstream/handle/2346/21404/31295015067852.pdf?sequence=1. (Accessed 25 November 2022).

[43] S.-M. Lee, D.S. Kang, W.-S. Kim, J.-S. Roh, Fabrication of isotropic bulk graphite using artificial graphite scrap, Carbon Lett 15 (2014) 142.

[44] W. Primak, L.H. Fuchs, Electrical conductivity of natural graphite crystal, Phys. Rev. 95 (1) (1954) 22–30, https://doi.org/10.1103/PhysRev.95.22.

[45] T.A. Yemata, Q. Ye, H. Zhou, A.K.K. Kyaw, W.S. Chin, J. Xu, 6 - conducting polymer-based thermoelectric composites: principles, processing, and applications, in: V.K. Thakur, M.K. Thakur, A. Pappu (Eds.), Hybrid Polymer Composite Materials, Woodhead Publishing, Kidlington, 2017, pp. 169–195, https://doi.org/10.1016/B978-0-08-100785-3.00006-1.

[46] H. Tulhoff, Carbides, in: ULLMANN'S Encyclopedia of Industrial Chemistry, Wiley-VCH Verlag GmbH & Co, Weinheim, 2012, pp. 565–582, https://doi.org/10.1002/14356007.a05_061.

[47] N. Deprez, D.S. McLachlan, The analysis of the electrical conductivity of graphite conductivity of graphite powders during compaction, J. Phys. D Appl. Phys. 21 (1988) 101, https://doi.org/10.1088/0022-3727/21/1/015.

[48] J.F. Shackelford, Y.-H. Han, S. Kim, S. H, CRC Materials Science and Engineering Handbook, fourth ed., CRC Press, London, 2015, p. 279.

[49] P.G. Klemens, D.F. Pedraza, Thermal conductivity of graphite in the basal plane, Carbon 32 (1994) 735–741, https://doi.org/10.1016/0008-6223(94)90096-5.

[50] Z. Lu, T. Jiang, Z. Min, S. Ke, A review of the coefficient of thermal expansion and thermal conductivity of graphite, N. Carbon Mater. 37 (3) (2022) 544–555, https://doi.org/10.1016/S1872-5805(22)60603-6.

[51] M. Mostafavi, S.A. McDonald, H. Centinel, P.M. Mummery, T.J. Marrow, Flexural strength and defect behaviour of polygranular graphite under different states of stress, Carbon 59 (2013) 325–336, https://doi.org/10.1016/j.carbon.2013.03.025.

[52] N. Guo, M.C. Leu, Effect of different graphite materials on the electrical conductivity and flexural strength of bipolar plates fabricated using selective laser sintering, Int. J. Hydrogen Energy 37 (4) (2012) 3558–3566, https://doi.org/10.1016/j.ijhydene.2011.11.058.

[53] T. Etter, P. Schulz, M. Weber, J. Metz, M. Wimmler, J.F. Löffler, P.J. Uggowitzer, Aluminium carbide formation in interpenetrating graphite/aluminium composites, Mat. Sic. Eng. A-Struct. 448 (1–2) (2007) 1–6, https://doi.org/10.1016/j.msea.2006.11.088.

[54] M. Ekpu, R. Bhatti, N. Ekere, S. Mallik, Advanced thermal management materials for heat sinks used in microelectronics, in: 18th European Microelectronics & Packaging Conference, 2011, pp. 1–8.

[55] E. Neubauer, P. Angerer, Advanced composite materials with tailored thermal properties for heat sink applications, in: 2007 European Conference on Power Electronics and Applications, 2007, pp. 1–8, https://doi.org/10.1109/EPE.2007.4417778.

[56] T. Schubert, L. Ciupinski, J. Morgiel, H. Wedmuller, T. Weissgarber, B. Kieback, Advanced Composite Materials for Heat Sink Applications, October 15-17, EuroPM2007, Toulouse, France, 2007. paper 587.

[57] I.E. Monjea, E. Louis, J.M. Molina, Optimizing thermal conductivity in gas-pressure infiltrated aluminum/diamond composites by precise processing control, Composites Part A-Appl. S. 48 (2013) 9–14, https://doi.org/10.1016/j.compositesa.2012.12.010.

[58] J.K. Chen, I.S. Chen, Thermal properties of aluminum–graphite composites by powder metallurgy, Composites Part B-Eng. 44 (1) (2013) 698–703, https://doi.org/10.1016/j.compositesb.2012.01.083.

[59] S.H. Lee, S.-H. Son, J.S. Kim, J. Yesuraj, K. Kim, S.-H. Rhi, Heat conduction and thermal expansion of copper–graphite composite as a heat sink, Int. J. Energy Res. 46 (8) (2022) 10907–10918, https://doi.org/10.1002/er.7891.

Artículo 4: Metal carbide additives in graphite-silicon composites for Lithium-Ion batteries

ChemElectroChem

Research Article
doi.org/10.1002/celc.202300339

Chemistry Europe
European Chemical Societies Publishing

www.chemelectrochem.org

Metal Carbide Additives in Graphite-Silicon Composites for Lithium-Ion Batteries

Juan Piñuela-Noval,[a] Daniel Fernández-González,[a] Sergio Brutti,[b] Marta Suárez,[a] Franco Mazzei,[c] Maria Assunta Navarra,[b] Luis Felipe Verdeja,[d] Adolfo Fernández,[a] and Marco Agostini*[c]

The pathway for improving lithium-ion batteries' energy density strongly depends on finding materials with enhanced performance. Although great efforts have been done, on the anode-side, graphite is still the best choice. In the last decade, silicon elements are attracting growing attention as anode since their use can theoretically increase specific capacity of the negative electrode side. However, as the electrochemical mechanism involves the alligation of a large amount of Li, the silicon electrode experiences huge volume changes (more than 300% of its initial volume), leading to fractures and pulverizations of the electrode. Herein, we propose for the first time using Molybdenum and Chromium Carbides as additive to stabilize graphite/silicon composites. Spark plasma sintering technology is used to sinter the electrode powders. We demonstrated that the presence of molybdenum or chromium carbides promotes the performance of C/Si electrodes, improving the cycling stability compared to pristine graphite/silicon electrodes.

Introduction

Lithium-ion batteries are today widely employed in portable electronic markets as the possibility to get a fast charging rate with good durability. Recently, the need to reduce fossil fuels paved the attention to employing such devices in powering electric vehicles, with the final goal of going zero emission in a short period. However, several reasons hinder the widespread of such technology in electric cars.[1] Among the others is the low energy density limited by using electrodic materials with low specific capacity.[2,3] One of that is the anode side, today commercially constituted by graphite-based electrodes, with Lithium storage thermodynamically limited by the intercalation-deintercalation mechanism of Li^+ in graphene layers (372 mAh g^{-1}).[1,4–6] As an alternative to graphite anode, silicon attracted growing attention due to its high theoretical capacity (3579 mAh g^{-1}) thanks to the alloying chemistry during lithiation ($Li_{15}Si_4$), the low working potential (about 0.4 V vs. Li^+/Li), the natural abundance and the non-toxicity.[1] However, the development of commercial silicon anodes is still a big challenge as massive volume changes of silicon particles (more than 300%) during the (de)lithiation process, which leads to fracture of the silicon and deformation of the electrode, pulverization and delamination.[1,7]

Furthermore, Si particles catalyze the decomposition of the electrolyte with the uncontrollable growth of solid electrolyte interface while being semi-conductor with low electronic conductivity of 6.7×10^{-1} S cm^{-1} which limits the rate charge.[7–10] To address the problems above, different approaches have been proposed in the last decade; one of these is to employ nanostructured Si (nanoparticles, yolk-shell, nanowires etc.),[11–13] composites,[14–16] polymer binders,[17–19] and additives[19,20] to improve Si-electrode performance in Li-cells. Involving metal carbides in silicon anodes is an additional strategy not yet explored to increase the capacity and cycle-life. Firstly, composite silicon/wolfram carbide@graphene with a particular microstructure has been reported to maintain high initial coulombic efficiency and long cycle life, alleviating structural changes.[21] In contrast, metal carbides (Mo_2C, Cr_2C_3, etc.) in the form of Si–Cr_3C_2@few-layer graphene and Si–Mo_2C@few-layer graphene electrodes were also reported with good electrochemical performance.[22] Furthermore, carbides, in general, can also provide an excellent conductive skeleton to improve the electronic conductivity of Si, thanks to the presence of nano-conductive channels that reduce electron transfer resistance.[23,24]

---

[a] J. Piñuela-Noval, Dr. D. Fernández-González, Dr. M. Suárez, Dr. A. Fernández
Nanomaterials and Nanotechnology Research Center (CINN-CSIC)
Universidad de Oviedo (UO)
Principado de Asturias (PA), Avda. de la Vega, 4–6, 33940, El Entrego (Spain)

[b] Prof. Dr. S. Brutti, Prof. Dr. M. A. Navarra
Department of Chemistry
"Sapienza" University of Rome
P.le Aldo Moro 5, 00185 Rome (Italy)

[c] Prof. Dr. F. Mazzei, Dr. M. Agostini
Department of Chemistry and Technology of Drugs
"Sapienza" University of Rome
P.le Aldo Moro 5, 00185 Rome (Italy)
E-mail: marco.agostini@uniroma1.it

[d] Prof. Dr. L. F. Verdeja
Departamento de Ciencia de los Materiales e Ingeniería Metalúrgica
Escuela de Minas, Energía y Materiales
Universidad de Oviedo
Calle Independencia, s/n, 33004, Oviedo/Uviéu, Asturias (Spain)

Supporting information for this article is available on the WWW under https://doi.org/10.1002/celc.202300339

This paper reports on using carbides (Mo and Cr based) in graphite-silicon composites for lithium-ion batteries. A simple to scale two-step process, consisting first in the formation of metallic carbides (molybdenum or chromium) in the matrix of graphite using spark plasma sintering technology and then in mixing graphite/carbides with Si nanoparticles (<250 nm) by ball milling was reported. Electrochemical performance is investigated and compared with standard graphite/Si nanoparticle electrodes. The results demonstrated how the presence of carbides stabilized the electrochemical performance regarding coulombic efficiency and cycling stability.

Results and discussion

Starting from battery-grade graphitic powder, a first electrodic powder was synthesized by dispersing 20% Si nanoparticles in commercial graphite powder (see experimental section); the obtained material was called GHDR 15–4. A second material was synthesized using graphitic powder named Asbury, following dispersing of 20% Si. The third material was synthesized by including in the graphitic matrix of Asbury 5% MoC and 20% Si nanoparticles, named Asbury-MoC. A fourth material was obtained mixing in the graphite 5% Cr_3C_2 and 20% Si nanoparticles, called Asbury-Cr_3C_2. All materials were first characterized by the use of X-ray diffraction (XRD), Figure 1a. All samples showed the presence of typical graphite and Si peaks, moreover, with reduced intensity for the sample, MoC (green) and Cr_3C_2 (orange) peaks, respectively. Raman spectroscopy was also performed for all samples, Figure 1b; corresponding Raman spectra highlighted peaks related to crystalline silicon (around 520 cm^{-1}).[25,26] Furthermore, D- and G-bands (Figure 1c), typical of carbon-based materials, were detected close at 1350 and 1580 cm-1.[26,27] G-band intensity is higher than D-band for all samples because of an ordered graphitic matrix.[25] Intensity ratio between D and G peaks have been calculated and reported in Table S1; the derived values highlighted difference between GHDR 15–4 and Asbury graphite, with the last one more graphitic. Furthermore, the addition of Carbides additives, including the spark plasma synthetic pathway, brought to more ordered materials. The scanning electron microscopy (SEM) images, including energy dispersive spectroscopy (EDX) evidenced a uniform distribution of Si (green color) in the graphitic matrix (red color) for all samples. At the same time, also second phases of Mo (blue color) and Cr (blue color) were well dispersed, Figures 1d–g. All samples mechanical and electrical properties were also measured (Table S2). The results showed improved elastic modulus, flexural strength, and electrical conductivity in samples containing carbides, Asbury-MoC and Asbury-Cr_3C_2.[28–31] This is related to the fact that the presence of carbides chemically attached to graphite particles can provide bridges in all space directions (x,y,z)[28–32] positively impacting mechanical properties. Moreover, carbides are good electrical conductors, and their dispersion in the compound can increase electron transference, enhancing the electrical conductivity.[28–31,33]

Electrochemical performance in Li-half cells

The electrochemical cycling tests were performed using the four compounds, with and without the addition of Si-nano-

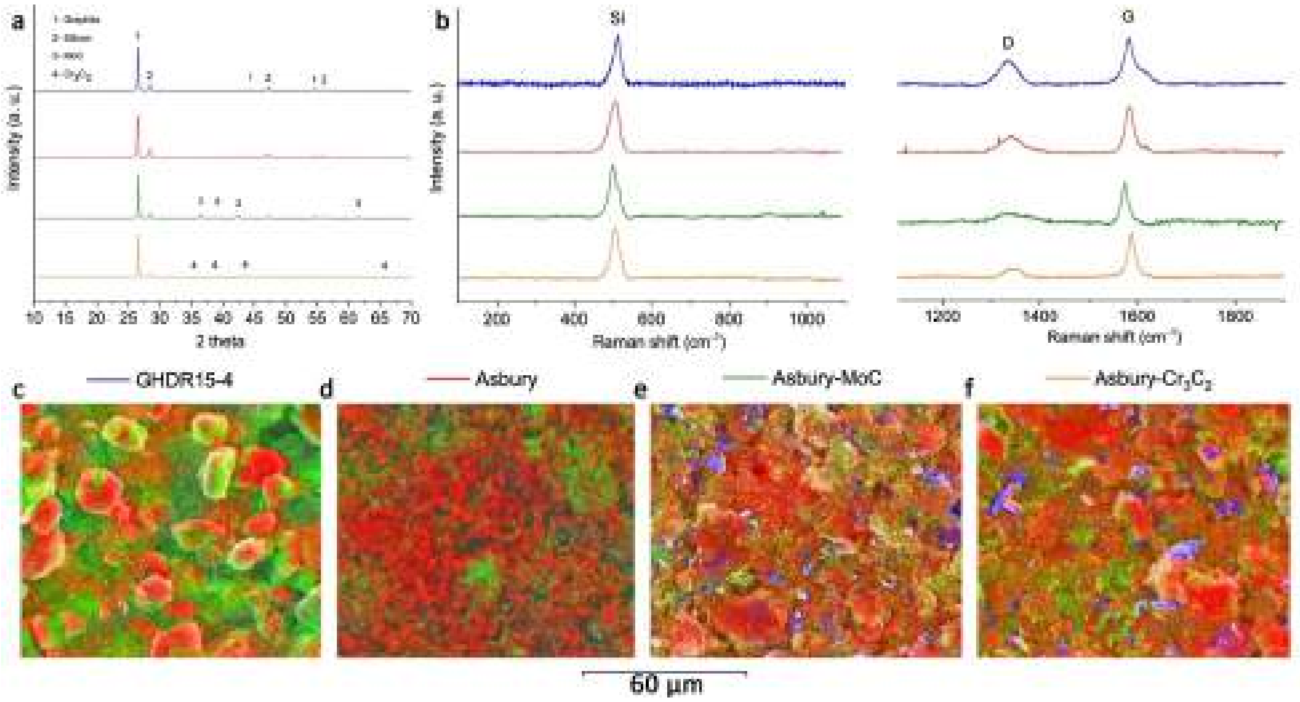

Figure 1. Pristine materials characterization: X-Ray diffraction patterns (**a**), Raman spectra (**b**) and SEM-EDX analysis for the GHDR15-4 (**c**, blue), Asbury (**d**, red), Asbury-MoC (**e**, green), Asbury-Cr_3C_2 (**f**, orange).

particles, as electrodes in Li-half cells; the cells were built using LP30 electrolyte (see the experimental section for composition). A first galvanostatic cycle is performed at C/10 rate (1 C = 3500 mA g^{-1}), to form a stable solid electrolyte interface at the surface of the particles and consequently stabilize the electrodes.[34–36] Following a current of C/3 is applied to evaluate the long-term performance of the compounds. The presence of Si improves the capacity for all materials, i.e., almost double, during the first cycle. Besides, the SEI formation occurs in the discharge process between 0.5–0.7 V, Figure 2;[37] in subsequent cycles, this slope change disappears (Figure S1). The first discharge involves in the range of potential below 0.2 V the lithiation process of Li^+ ion intercalation in the structure of the active material: $xLi^+ + 6\,C \rightarrow Li_xC_6$ $(0 < x \leq 1)$ and the Li-alloy formation: $yLi + Si \rightarrow Li_ySi$ $(1.71 < y \leq 4.4)$.[38, 39] In the following charge, the de-lithiation reaction of graphite, i.e., below 0.25 V, and de-alloying of Si, between 0.3 and 0.5 V, take place.[22,39–41] In this aspect, during the first cycle, the Li-cell using the pristine Asbury graphite and the Asbury-20%wt Si, Figure 2b, shows mostly the graphite intercalation and de-intercalation. The rest of the samples highlighted the graphite and silicon lithiation process.

After initial_activation, during the first 100 cycles (Figure S2), all the electrodes (with and without Si-nanoparticles) showed similar trends, with initial capacity decay in the first ten cycles and following stabilization. Focusing more in detail on the evolution of this up to 100 cycles, Figure S2, it is observed how GHDR15.4 sample (a) reaches the stability at around cycle 40, and its capacity goes, approximately, from 125 to 250 mAh/g and Asbury sample (b) reaches the stability at around cycle 25 and its capacity increases of more > 130% (from 90 mAh/g to 230 mAh/g). Finally, Asbury-MoC and Asbury-Cr_3C_2 samples (c and d) are stable above cycle 50, improving their capacity until ~200 mAh/g from less than 120 mAh/g. Therefore, the electrodes formed by active materials without carbides stabilize their capacity quickly, mainly because they are more sensitive to activation, and the gain in capacity is greater than those with carbides. Carbide presence causes the slower formation of stable SEI layer on particles, and stabilization up to running values,[39,42] apart from having lower theoretical specific capacity.[42,43] Asbury sample reaches stability sooner than the other, which can be the size and morphology of particles lower than the rest of the active materials and flakes.

Prolonged cycling performance were performed for over 400 cycles and reported in Figure 3. First, the cells were activated at C/20 current rate (Figure 3a), as the presence of carbides in the graphitic structure requires a longer time to form a stable SEI interface during the 1st cycle, with consequent activation of electrode particles upon cycling. Thus the formation of SEI is slowly, providing faster activation and stabilization of all materials, with improved delivered capacity: for GHDR15-4 above 300 mAh g^{-1}, Asbury around 275 mAh g^{-1}, Asbury-MoC to 250 mAh g^{-1} and Asbury-Cr_3C_2 above 200 mAh g^{-1}. A major improvement is on prolonged cyclic performance, where electrodes with carbides in their structure showed very high stability. The different Li_ySi phases formation

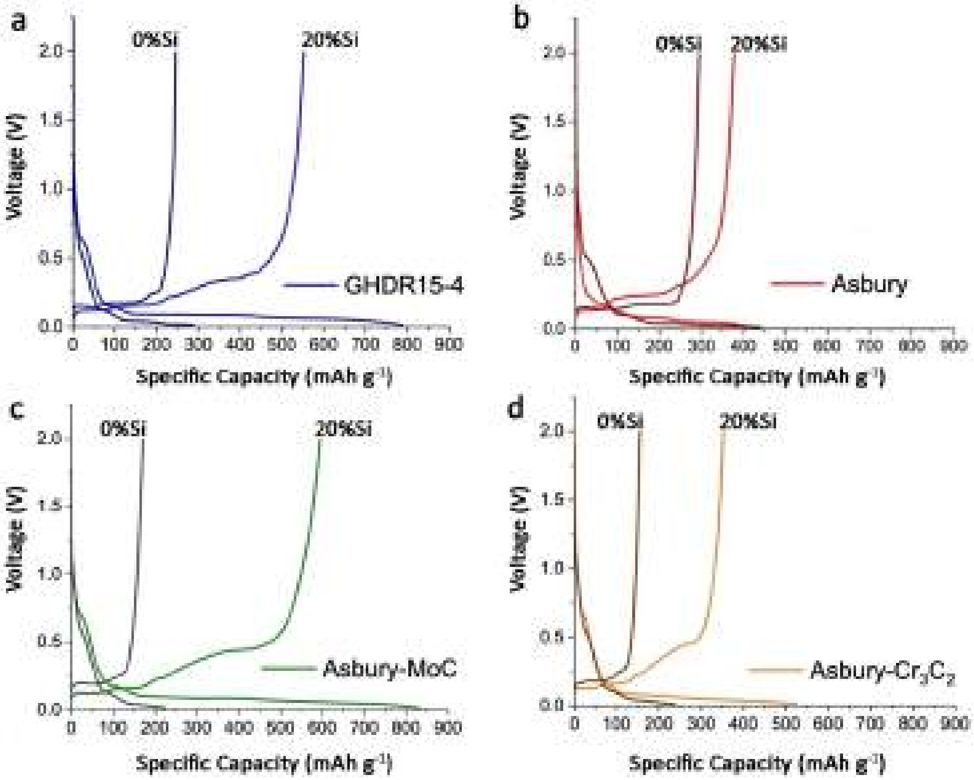

Figure 2. 1st cycle charge-discharge profile, C/10; cut off 0.01-2 V. Materials with and without 20% Si nanoparticles addition: GHDR15-4 **(a)**, Asbury **(b)**, Asbury-MoC **(c)**, Asbury-Cr_3C_2 **(d)**.

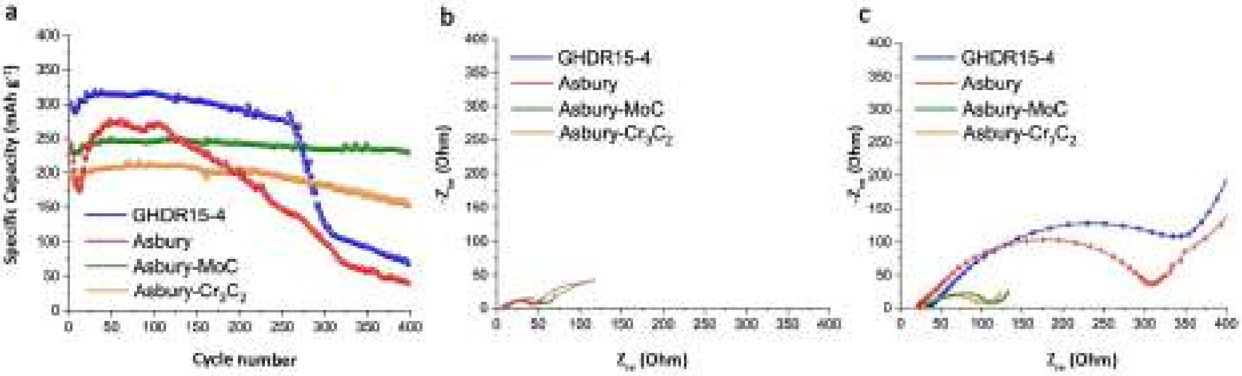

Figure 3. Cycle performance of the GHDR 15–4, Asbury, Asbury-MoC and Asbury-Cr3 C2 in Li-half cell using LP30 electrolyte **(a)**. Cut off 0.01-2 V; 1st cycle performed at C/20 and following C/3. Electrochemical impedance spectroscopy (EIS) of the Li-half cells using the four different electrodes at cycle 1st **(b)** and after 400th **(c)** cycles.

originates successive volume expansions in their internal structure during lithiation/delithiation processes.[44] This stress, generated by those sudden changes, leads to a fracture of the active material connections, producing a progressive disintegration of the electrode.[45] Consequently, the SEI layer is affected by Si cracking and pulverization, and part of the electrode surface is again exposed to the decomposition of the electrolyte through irreversible consumption of Li^+ ions to form a new SEI layer.[46–48] Since carbides were demonstrated to enhance the mechanical properties of the compound powder, see Table S1, the electrode and the associated SEI layer are more flexible, mitigating cracking due to huge volume changes, thus extending the cycle-life of the electrode.[22] Furthermore, adding Cr_3C_2 and MoC sintered with graphite can generate conductive channel networks that enormously improve the electrical conductivity (Table S1).[42] They provide stable morphology and conductive skeletons for the diffusion of Li^+ ions, increasing interfaces, and transfer of electrons.[22,49]

To investigate galvanostatic results, electrochemical impedance spectroscopy analysis (EIS) was carried out to evaluate the SEI interface resistance of electrodes at the 1st and after 400 cycles, Figure 3b and c.[50] The Li-ion half-cell system was modeled using a typical equivalent circuit,[50,51] represented in Figure S3. The overall resistance of electrodes containing carbides is maintained stable, Figures 3b and **c**, while the GHDR15-4 and Asbury electrodes highlighted a significant resistance increase.

All parameters resulting from the fitting analysis are reported in Table 1, where R1 corresponds to the Li-half cells bulk resistance, which includes the electrolyte, separator, and electrodes.[50] In all the cases after cycle 400, the R1 has the same range of values. R2 and Q1 are the resistance and capacitance of the SEI layer; R2 shows a significant increase in GHDR15-4 and Asbury cells after 400 cycles, indicating the SEI layer growing upon cycling. Q1 decreases for the graphite, specifying that the SEI layer is more compact and inorganic (Li_2O, LiF, Li_2CO_3, SiO_2). At the same time, Q1 slightly rises after 400 cycles in carbides, marking a porous and more organic SEI (lithium organic carbonates and carbon compounds). T1 is a time constant obtained by multiplying R1 and Q2; this indicates the time that Li^+ ions take to penetrate the SEI layer towards the active material surface. Lithium motion is shown slower in samples without carbides. Continuing with the analysis, R3 and Q2 represent the charge-transfer resistance and the related capacitance. R3 is stable in all samples and does not remarkably increase after 400 cycles. Carbides make electrochemical reactions easier, improving the charge transfer of electrons and Li^+ ions. Q2 refers to the electrochemically active area for the

Table 1. Electric parameters were obtained from the equivalent circuit fitted for the materials in the 1st and 400th cycles.

Parameter	Cycle 1 (error ±5 %)				Cycle 400 (error ±5 %)			
	GHDR15-4	Asbury	Asbury-MoC	Asbury- Cr_3C_2	GHDR15-4	Asbury	Asbury- MoC	Asbury- Cr_3C_2
R1 (elec.) [Ω]	5.8	8.0	8.6	10.1	33.9	24.9	26.9	25.3
R2 (SEI) [Ω]	35.6	41.2	50.1	36.2	340.9	304.5	81.3	73.1
Q1 [F]	6.5×10^{-5}	6.7×10^{-6}	2.9×10^{-5}	2.1×10^{-5}	1.9×10^{-5}	3.4×10^{-5}	$4.7*10^{-5}$	3.2×10^{-5}
T1 = R2*Q1 [s]	2.3×10^{-3}	2.8×10^{-3}	1.5×10^{-3}	1.1×10^{-3}	6.4×10^{-3}	10.4×10^{-3}	$3.8*10^{-3}$	2.3×10^{-3}
R3(Ch. Tr) [Ω]	13.6	20.1	13.1	14.7	15.3	23.7	13.3	15.1
Q2 [F]	2.5×10^{-3}	2.8×10^{-3}	1.2×10^{-3}	2.3×10^{-3}	8×10^{-4}	1.6×10^{-3}	5×10^{-3}	3.1×10^{-3}
T2 = R3*Q2 [s]	3.4×10^{-2}	5.6×10^{-2}	1.6×10^{-2}	1.1×10^{-2}	1.2×10^{-2}	3.8×10^{-2}	6.6×10^{-2}	4.7×10^{-2}
W1 [Ω]	5.1×10^{-2}	1.3×10^{-2}	3.7×10^{-2}	4.9×10^{-2}	1.2×10^{-4}	3.1×10^{-3}	6.7×10^{-2}	5.3×10^{-2}
W1 Change (%)	–	–	–	–	−99.8	−76.2	+81.1	+8.2

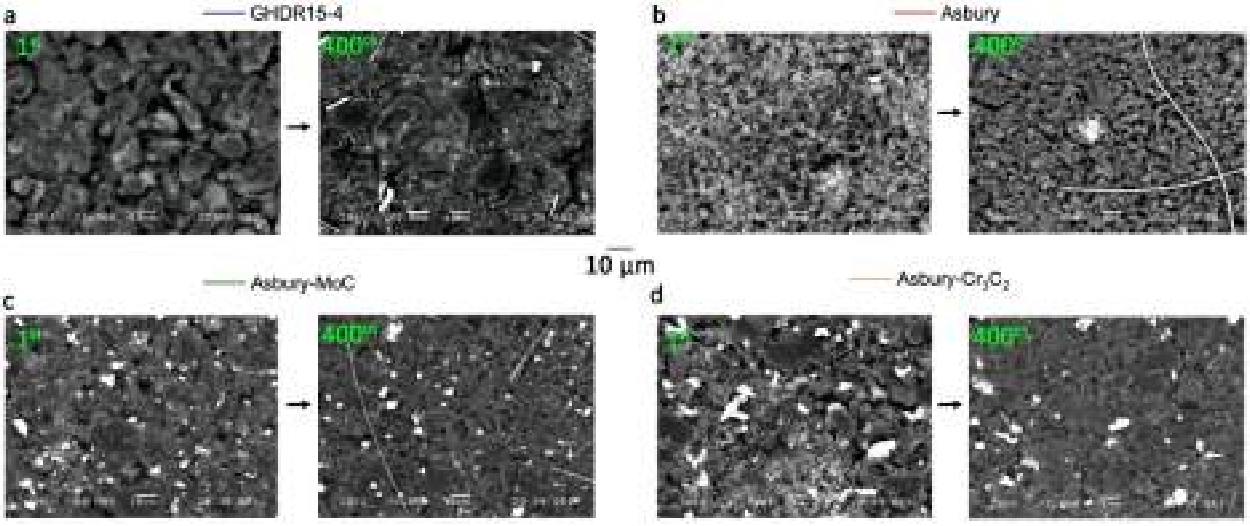

Figure 4. SEM images (BEI) of the materials after 1st and 400th cycles of discharge/charge. GHDR15-4 (a), Asbury (b), Asbury-MoC (c), Asbury-Cr_3C_2 (d).

redox reaction, which decreases in the samples composed only of graphite and silicon, while it remains stable when the material includes carbides. Finally, W1 is the Warburg impedance[50] and represents the Li^+ ions diffusion in the host material;[50] This is directly correlated with the diffusion coefficient. For the samples without carbides, W1 values strongly decrease, indicating a slower Li^+ ions motion inside the active material. The presence of carbides facilitates this transportation improving the diffusion. With this quantification, it can be affirmed that the presence of carbides helps the active material, specifically to the volume changes of silicon, providing structural integrity, more excellent electrical conductivity, and control of the side reactions to achieve an adequate capacity and spectacular stability for over 400 cycles.

To further support the Galvanostatic cycling performance and the SEI resistance improvements when including 5% carbides in the anodic powder, SEM images were collected on electrodes recovered after 1st and 400th cycles, Figure 4. SEM Images (BEI) give qualitative evidence of the cycling performance. In graphite without carbides (GHDR15-4: Figure 4a and Asbury: Figure 4b), it is plainly observed the degradation in the anode at cycle 400. There are big black zones evidencing the formation of a thick SEI layer, which limits the redox reactions with Li and cell operation. C, Si, O, and F content was also evaluated using SEM-EDX, see Table 1. For pristine commercial graphite, GHDR15-4 (Figure 4a) and Asbury graphite (Figure 4b) shows a strong degradation of the electrode surface between cycle 1st and 400th. The samples, including MoC, Figure 4c, and Cr_3C_2, Figure 4d, showed different surface images. In particular, the one including Cr_3C_2 shows a stable SEI layer but the presence of some holes in the surface, confirming the lower cycling stability of Figure 3, as SEI breaks down before than the one with molybdenum (IV) carbide (Figure 4c), which showed few signs of degradation. The ratio of C/Si, O/Si, and F/Si to confirm the aforementioned statements have been collected and reported in Table 2. In all cases, the percentages have increased as a consequence of electrolyte degradation on active material. However, materials with carbides experienced a lower rise.

The EDX analysis highlighted the composition of the SEI layer: silica (SiO_2), organic and inorganic lithium carbonates (Li_2CO_3), Li_2O, and LiF. The presence of oxygen, deriving from solvent decomposition, is an issue as it tends to oxidize metallic species, forming oxides, such as SiO_2, reducing the specific capacity, cycling stability, and reversibility of the electrochemical process. In this aspect, the presence of carbides acting as a scavenger for oxygen avoids the polarization of the surface and the formation of dangerous compounds such as silica. The white fibers appearing in the SEM images after 400 cycles are glass fibers derived from the separator used to build the Li-half cells.

Table 2. C/Si, O/Si, and F/Si ratio (considering wt. %) of the electrode materials recovered after 1st and 400th cycles.

Material	C/Si		O/Si		F/Si	
	Cycle 1	Cycle 400	Cycle 1	Cycle 400	Cycle 1	Cycle 400
GHDR15-4	10.32	12.71	0.54	3.61	0.56	4.08
Asbury	13.64	20.57	0.76	5.49	0.44	4.86
Asbury-MoC	8.37	9.26	0.14	2.51	0.31	1.96
Asbury-Cr_3C_2	9.10	10.86	0.21	2.53	0.38	2.99

Conclusions

We showed that the presence of carbides based on Mo and Cr in a graphitic matrix including Si-nano particles produces a beneficial effect in terms of mechanical properties, alleviating Si-particle cracking due to huge volume changes during the lithiation processes. The cycling performance of these materials in Li-half cells showed improvements in delivered capacity and cycle life. Despite a Coulombic efficency slightly lower than pristine materials, the carbides added Silicon/Carbon electrodes showed an improved efficency and capacity retention for prolonged cycling, see Figure S4. This was also due to optimizing the activation steps, reducing the cycling current during the first discharge/charge to C/20 current rate, thus favoring the formation of a less compact and thick SEI layer, avoiding particles breaking upon Li^+ storage. The presence of carbide additives strongly stabilized the electrochemical performance over 400 cycles, with no sign of capacity fading. Deterioration mechanism was studied in pristine electrodes and compared with carbides added; SEM images revealed few signs of carbide based electrode deterioration, while EIS showed stable interface resistance and Li^+ diffusion in the active material matrix. Thus, in conclusion, using metal carbides in Si-based anodic materials opens the path to improve electrochemical performance and cycling stability.

Experimental section

Processing of graphite/silicon composites

Raw materials for the preparation of the graphite-silicon and graphite-metal carbides (MoC or Cr_3C_2)-silicon materials for the anodes consisted of:

- Battery-quality graphite (C-NERGY Actilion GHDR15-4 supplied by Imerys): purity 99.95 %, with spheroidal morphology.
- Standard graphite (Asbury Carbons Company): purity 99 %, with spheroidal-flake morphology.
- Molybdenum (H. C. Starck): purity 99.5 %, with spheroidal morphology
- Chromium (Sigma Aldrich): purity $\geq$ 99 %, with spheroidal morphology.
- Titanium (Abcr GMbh): purity 99.5 %, with irregular morphology.
- Silicon (Ferroglobe): purity 99.9 %, with spheroidal morphology and mean particle size (d_{50}) of 250 nm.

Spark plasma sintering has been used to prepare composites of graphite-MoC and graphite-Cr_3C_2. The graphite employed to fabricate the composites was non-specific for batteries, from Asbury Carbons Company. First, molybdenum (or chromium) and titanium powders were mixed in a roller mill with alumina balls for 24 h. Then, the mixture has been charged into the high-energy attrition mill (Union Process Inc. USA) with the graphite and 3 mm in diameter alumina balls, and it was mixed for 3 hours at a rate of 45 Hz. Mixtures have been prepared using isopropyl alcohol to facilitate the mixing and ensure a homogeneous material for later operations. Finally, the material was dried at 100 °C and sieved by 125 μm. Two types of compositions have been prepared based on the results in terms of electrical, mechanical, and thermal properties studied in other research works:[28–31]

Graphite-5.5 vol. % molybdenum-0.6 vol. % titanium.

Graphite-5.5 vol. % chromium-0.6 vol. % titanium.

Titanium has been used to stabilize α-MoC_{1-x} carbide (cubic, unstable below 1960 °C).[28] In the case of chromium, the proportion of titanium has been maintained to avoid adding new compositional variables to the process.

Green compacts have been prepared by uniaxial pressing of the powder's mixtures at 20 MPa. Green specimens have been loaded into the graphite dies, and the heat treatment has been different depending on the composite to achieve the liquid phase sintering based on the carbon-molybdenum and carbon-chromium binary phase diagrams. This would lead a close contact between the graphite and the metal to promote the formation of the carbides:

Graphite-molybdenum system: dwell temperature of 2640 °C for 20 minutes under an applied pressure of 25 MPa.

Graphite-chromium system: dwell temperature of 2000 °C for 20 minutes under an applied pressure of 25 MPa.

The process has not been simple but a reactive sintering process, where the carbon has reacted with the metal to form the Carbide. The sintered discs, 170 mm in diameter and 20 mm in height with the already formed carbides were crushed and ground down to $<$ 75 μm. These powders have been used as raw materials for the anodes.

The mixtures of graphite-MoC, graphite-Cr_3C_2 and battery-quality graphite with 20 wt. % silicon nanoparticles have been prepared by low energy ball milling with 3 mm in diameter alumina balls and isopropyl alcohol at 100 rpm for 24 hours. Once dried and sieved by $<$ 180 μm, the powder was used to fabricate the anodes for electrochemical measurements.

Electrochemical performance

- Electrode preparation: The active material based on Si, carbon black (conducting agent) and polyvinylidene dyfluoride (PVDF, polymer binder) were thoroughly mixed in an agate mortar with a weight proportion of 8:1:1. Then, by adding N-methyl pyrrolidone (NMP) in a relation 0.5 ml to 100 mg of active material, a black paste was prepared. Following, this was deposited on a copper foil using a doctor blade. The layer of 250 μm was dried in a heating plate for 24 h at 100 °C, with complete evaporation of NMP and moisture. Electrodes with 10 mm diameter and 3–4 mg loading were cut and dried in a tubular glass oven at 100 °C with a vacuum for 6 hrs.
- Coin cell manufacture: Li half-cells were assembled using electrodes inside a controlled atmosphere of Ar, where moisture and oxygen were below 0.1 ppm. A Whatman fiberglass separator with 18 mm diameter and Li counter electrode has been employed. As an electrolyte, 120 μl of 1 M $LiPF_6$ in EC:DMC (ethylene carbonate /dimethyl carbonate volume 1:1, named LP30) were added to the separator. Finally, the coin cell was closed using a 50 kg/cm^2 pressure.
- Electrochemical testing: galvanostatic cycling tests were carried out to evaluate the performance of the electrode materials (capacity and cycle-life). The current is established considering the reversible specific capacity of the silicon (3500 mAh/g) and its mass, assuming 1 C = 3500 mA/g. To get the whole capacity, it must be referred to as the total mass of the active material. For all the materials, the discharge/charge performance is divided into two steps: 1) activation cycle at C/10 or C/20, voltage cut off 0.01–2 V, and 2) the rest of the cycles at C/3 with a voltage cut off 0.01–2 V. All electrochemical measurements were made at room temperature (25 °C). To carry out tests only with the graphite (without silicon) as active material, the same current

density (J [mA/g]) is imposed with the purpose of calculating the current and making a comparison with silicon.

EIS (electrochemical impedance spectroscopy) studied the interface resistances and electrode processes by applying a 10 mV AC amplitude signal to Li symmetrical cell in a 500 kHz to 100 mHz frequency range. The interface and charge transfer resistance were evaluated by the nonlinear least squares (NLLS) fit of the semicircles observed in the Nyquist plots. The Nyquist plots related to the Li cells stability show the semicircles associated with film formation and charge-transfer processes located at high and low-frequency regions, respectively. The equivalent circuit used for the NLLS fit was R(RQ)(RQ)W, where R represents the resistance, Q is the constant phase element (CPE), and W is the Warburg resistance.

To analyze postmortem electrodes, they must be processed inside the glovebox when the cells are disassembled. Afterward, the electrodes are cleaned with dimethyl carbonate (DMC, Merk) and tetrahydrofuran (THF, Merk) to remove soluble contaminants and the salt remains. Finally, they are dried for half an hour under vacuum conditions and saved inside vials in the glove box.

Characterization techniques

X-ray diffraction technique has been employed for the identification of the mineralogical phases. It consisted of a Bruker Advanced Powder X-ray diffractometer model D8 with Cu-kα radiation ($\lambda = 0.15406$ nm). Copper anticathode water cooled with an intensity of 40 mA and a voltage of 40 kV, a swept between 10–70° with a step of 0.02° and a step time of 0.2 s were the working conditions. Peak fitting of the crystalline phases was performed by diffraction pattern files provided by JCPDS (International Centre for Diffraction Data), using Xpowder Software.

Raman analysis was performed using a Dilor LabRam micro-Raman Spectrometer utilizing a HeNe 632.8 nm, 4.7 mW laser; 1800 grooves mm − 1 grating; and an X50 objective.

MEB JEOL-6610LV with microanalysis INCA Energy-350 has been employed for the microstructural characterization of the pristine material in cycles 1 and 400. The mapping of elements was provided by Energy-dispersive X-ray spectroscopy (EDX). The back-scattered electron imaging (BEI) mode has been employed in the Field Emission Scanning Electron Microscope (SEM) on a Quanta FEG 650.

The flexural strength was determined on specimens of 3 mm x 4 mm×20 mm. The equipment was a Shimadzu-Serie AGS-IX test machine. The flexural strength (σ_f, in Mpa) of the samples measured using the three-point bending test has been evaluated using equation (2).

$$\sigma_f = \frac{3 \cdot P \cdot L}{2 \cdot w \cdot b^2} \tag{2}$$

Where P is the failure load in N, L is the distance between supports (span, 12.5 mm) in mm, w is the width of the sample in mm, and b is the thickness of the sample in mm.

The Young's modulus was measured using a Grindsonic (MK, Belgium) equipment on 3 mm×4 mm×20 mm samples.

The electrical conductivity was measured by a four-point probe test in the in-plane direction using the equipment PSM1735 – NumetriQ – Newtons 4th.

Acknowledgements

Juan Piñuela Noval acknowledges the Programa "Severo Ochoa" of Grants for Research and Teaching of the Principality of Asturias for the funds received for the elaboration of the Ph. D. Thesis (Ref.: BP20 041). Juan Piñuela Noval also thanks the grant "Ayuda de Estancias Breves en otros Centros de Investigación" within the Programa "Severo Ochoa" for the training in research and teaching in 2022 (Ref.: EB22-11). Daniel Fernández-González acknowledges the grant (Juan de la Cierva-Formación program) FJC2019-041139-I funded by MCIN/AEI/10.13039/501100011033 (Ministerio de Ciencia e Innovación, Agencia Estatal de Investigación). This research was supported by the project Investigación industrial de materiales estratégicos para baterías de ión-litio de alta densidad energética y coste optimizado en electromovilidad sostenible LiOn-HD, promoted by Iniciativas Estratégicas Sectoriales de Innovación Empresarial (Programa "Misiones CDTI"), en el marco del Programa Estatal de Liderazgo Empresarial en 1+D+I, del Plan Estatal de Investigación Científica y Técnica y de Innovación 2017–2020. Science and Innovation Ministry of Spain. Authors are grateful to Ainhoa Macías San Miguel from Nanomaterials and Nanotechnology Research Center (CINN) for providing technical assistance.

Conflict of Interests

The authors declare no conflict of interest.

Data Availability Statement

The data that support the findings of this study are available from the corresponding author upon reasonable request.

Keywords: Li-ion batteries · silicon · molybdenum carbide · chromium carbide · anode · graphite

[1] H. J. Kim, T. N. V. Krishna, K. Zeb, V. Rajangam, C. V. V. M. Gopi, S. Sambasivam, K. V. G. Raghavendra, I. M. Obaidat, *Electronics.* **2020**, *9*, 1161.
[2] H. Gong, J. Sun, *Encyclopedia of Nanomaterials.* **2023**, *2*, 533–549.
[3] T. Kim, W. Song, D.-Y. Son, L. K. Ono, Y. Qi, *J. Mater. Chem. A* **2019**, *7*, 2942.
[4] C. Chaves, E. Pereira, P. Ferreira, A. G. Dias, *The Extractive Industries and Society.* **2021**, *8*, 100928.
[5] H. Vikström, S. Davidson, M. Höök, *Appl. Energy* **2013**, *110*, 252–266.
[6] S. Chae, S.-H. Choi, N. Kim, J. Sung, J. Cho, *Angew. Chem. Int. Ed.* **2019**, *59*, 110–135.
[7] T. Yoon, C. C. Nguyen, D. M. Seo, B. L. Lucht, *J. Electrochem. Soc.* **2015**, *162*, A2325-A2330.
[8] D. Aurbach, *J. Power Sources* **2020**, *89*, 206–218.
[9] C. K. Chan, R. Ruffo, S. S. Hong, Y. Cui, *J. Power Sources* **2009**, *189*, 1132–1140.
[10] P. Verma, P. Maire, P. Novak, *Electrochim. Acta* **2010**, *55*, 6332–6341.
[11] H. Wu, Y. Cui, *Nano Today* **2012**, *7*, 414–429.
[12] J.-Y. Li, Q. Xu, G. Li, Y.-X. Yin, L.-J. Wan, Y.-G. Guo, *Mater. Chem. Front.* **2017**, *1*, 1691–1708.
[13] N. P. Wagner, A. Tron, J. R. Tolchard, G. Noia, M. P. Bellmann, *J. Power Sources* **2019**, *414*, 486.
[14] P. Li, H. Kim, S.-T. Myung, Y.-K. Sun, *Energy Storage Mater.* **2021**, *35*, 550.

[15] E. Moyassari, T. Roth, S. Kücher, C.-C. Chang, S.-C. Hou, F. B. Spingler, A. Jossen, *J. Electrochem. Soc.* **2022** *169*, 010504.
[16] M. Otero, C. Heim, E. P. M. Leiva, N. Wagner, A. Friedrich, *Sci. Rep.* **2018**, *8*, 15851.
[17] N. Hamzelui, G. G. Eshetu, E. Figgemeier, *J. Energy Storage* **2021**, *35*, 102098.
[18] Z. Li, Y. Yang, Z. Wan, X. Zeng, L. Yan, S. Wu, M. Ling, C. Liang, K. N. Hui, Z. Lin, *Adv. Energy Mater.* **2022**, *12*, 2201197.
[19] G. G. Eshetu, E. Figgemeier, *ChemSusChem* **2019**, *12*, 2488–2828.
[20] Y. Zhou, H. Sun, M. H. Uddin, M. K. S. Barr, D. Wisser, P. Robmann, J. D. Esper, S. Tymek, D. Döhler, W. Peukert, M. Hartmann, J. Bachmann, *Electrochim. Acta* **2021**, *388*, 138522.
[21] W. Sun, R. Hu, H. Liu, H. Zhang, J. Liu, L. Yang, H. Wang, M. Zhu, *Electrochim. Acta* **2016**, *191*, 462.
[22] Y. Liu, W. Sun, X. Lan, R. Hu, J. Cui, J. Liu, J. Liu, Y. Zhang, M. Zhu, *ACS Appl. Mater. Interfaces* **2019**, *11*, 3872.
[23] W. Pan, X. Cai, C. Yang, L. Zhou, *J. Electron. Mater.* **2021**, *50*, 2584–2593.
[24] K. Xu, X. Li, X. Liu, Y. Yu, X. Zhang, W. Lei, Z. Xie, S. Zhang, Q. Jia, H. Zhang, *Sustain. Mater. Technol.* **2023**, *36*, e00583.
[25] S. Komaba, N. Yabuuchi, T. Ozeki, Z.-J. Han, K. Shimomura, H. Yui, Y. Katayama, T. Miura, *J. Phys. Chem. C* **2012**, *116*, 1380.
[26] J. Nanda, M. K. Datta, J. T. Remillard, A. O'Neill, P. N. Kumta, *Electrochem. Commun.* **2009**, *11*, 235.
[27] M. A. Cabañero, M. Hagen, E. Quiroga-González, *Electrochim. Acta* **2021**, *374*, 137487.
[28] M. Suárez, D. Fernández-González, C. F. Gutiérrez-González, L. A. Díaz, A. Borrell, J. S. Moya, R. Torrecillas, A. Fernández, *J. Eur. Ceram. Soc.* **2022**, *42*, 2048.
[29] M. Suárez, D. Fernández-González, L. A. Díaz, J. Piñuela-Noval, A. Borrell, J. S. Moya, R. Torrecillas, A. Fernández, *Boletín de la Sociedad Española de Cerámica y Vidrio.* **2023**, in press. https://doi.org/10.1016/j.bsecv.2023.02.005.
[30] M. Suárez, D. Fernández-González, L. A. Díaz, A. Borrell, J. S. Moya, A. Fernández, *Ceram. Int.* **2021**, *47*, 30993.
[31] J. Piñuela-Noval, D. Fernández-González, M. Suárez, L. A. Díaz, L. F. Verdeja, A. Fernández, *J. Am. Ceram. Soc.* **2023**, in press. https://doi.org/10.1111/jace.19145.
[32] J. Guardia-Valenzuela, A. Bertarelli, F. Carra, N. Mariani, S. Bizzaro, R. Arenal, *Carbon* **2018**, *135*, 72.
[33] N. Mariani, Development of Novel, Advanced Molybdenum-based Composites for High Energy Physics Applications, **2014**, Ph. D Thesis (Supervisor: A. Bertarelli), Politecnico di Milano, Milan, Italy.
[34] Y. Liu, W. Sun, X. Lan, R. Hu, J. Cui, J. Liu, J. Liu, Y. Zhang, M. Zhu, *ACS Appl. Mater. Interfaces* **2019**, *11*, 38727.
[35] W. Sun, R. Hu, H. Zhang, Y. Wang, L. Yang, J. Liu, M. Zhu, *Electrochim. Acta* **2016**, *187*, 1.
[36] Y. Zhou, H. Guo, Y. Yang, Z. Wang, X. Li, R. Zhou, W. Peng, *Mater. Lett.* **2016**, *168*, 138.
[37] C. Bongiorno, G. Mannino, U. D'Alessio, F. Monforte, G. G. Condorelli, C. Spinella, A. La Magna, S. Brutti, *Energy Technol.* **2021**, *10*, 2100791.
[38] B. A. Boukamp, G. C. Lesh, R. A. Huggins, *J. Electrochem. Soc.* **1981**, *128*, 725.
[39] K. Xu, X. Li, X. Liu, Y. Yu, X. Zhang, W. Lei, Z. Xie, S. Zhang, Q. Jia, H. Zhang, *Sustain. Mater. Technol.* **2023**, *36*, e00583.
[40] B. Fuchsbichler, C. Stangl, H. Kren, F. Uhlig, S. Koller, *J. Power Sources* **2011**, *196*, 2889.
[41] Q. Xu, Q. Wang, D. Chen, Y. Zhong, Z. Wu, Y. Song, G. Wang, Y. Liu, B. Zhong, X. Guo, *Green Chem.* **2021**, *23*, 4531.
[42] W. Pan, X. Cai, C. Yang, L. Zhou, *J. Electron. Mater.* **2021**, *50*, 2584.
[43] Y. Liu, W. Sun, X. Lan, R. Hu, J. Cui, J. Liu, J. Liu, Y. Zhang, M. Zhu, *ACS Appl. Mater. Interfaces* **2019**, *11*, 38727.
[44] N. Cuesta Pedrayes, Materiales anódicos alternativos para el desarrollo de baterías de ión-litio sostenibles, **2016**, Ph.D. Thesis (supervisors: I. Cameán Martínez and A. E. Ramos Alonso) Instituto Nacional del Carbón-Consejo Superior de Investigaciones Científicas (INCAR-CSIC)-Universidad de Oviedo, Oviedo/Uviéu, Asturias, Spain.
[45] M. N. Obrovac, L. Christensen, *Electrochem. Solid-State Lett.* **2004**, *7*, A93.
[46] M. T. McDowell, S. W. Lee, W. D. Nix, Y. Cui, *Adv. Mater.* **2013**, *25*, 4966–4985.
[47] N. Liu, H. Wu, M. T. McDowell, Y. Yao, C. Wang, Y. Cui, *Nano Lett.* **2012**, *12*, 3315.
[48] B. Scrosati, J. Garche, *J. Power Sources* **2010**, *195*, 2419.
[49] W. Sun, R. Hu, H. Liu, H. Zhang, J. Liu, L. Yang, H. Wang, M. Zhu, *Electrochim. Acta* **2016**, *191*, 462.
[50] W. Choi, H.-C. Shin, J. M. Kim, J.-Y. Choi, W.-S. Yoon, *J. Electrochem. Sci. Technol.* **2020**, *11*, 1–13.
[51] N. S. Zhai, M. W. Li, W. L. Wang, D. L. Zhang, D. G. Xu, *J. Phys. Conf. Ser.* **2006**, *48*, 1157.

Manuscript received: July 18, 2023
Revised manuscript received: September 26, 2023
Version of record online: October 12, 2023

Artículo 5: Modifying reduced graphene oxide substrate with Mo/MoO$_3$: benefits on Li/S cell performance.

Enhancement of Li/S battery performance by a modified reduced graphene oxide carbon host decorated with MoO_3.

Juan Piñuela-Noval,[1] Daniel Fernández-González,[1] Marta Suárez,[1] Luis Felipe Verdeja,[2] Arcangelo Celeste,[3] Adriano Pierini,[3] Franco Mazzei,[4] Maria Assunta Navarra,[3] Sergio Brutti,[3] Adolfo Fernández,[1] Marco Agostini[4].

[1]Nanomaterials and Nanotechnology Research Center (CINN-CSIC), Universidad de Oviedo (UO), Principado de Asturias (PA), Avda. de la Vega, 4-6, 33940, El Entrego, Spain.

[2]Departamento de Ciencia de los Materiales e Ingeniería Metalúrgica, Escuela de Minas, Energía y Materiales, Universidad de Oviedo, Calle Independencia, s/n, 33004, Oviedo/Uviéu, Asturias, Spain.

[3]Department of Chemistry, Università di Roma "La Sapienza", p.le Aldo Moro 5, 00185 Roma, Italy.

[4]Department of Chemistry and Drug Technologies, Sapienza University of Rome, P.le Aldo Moro 5, 00185 Rome, Italy.

Abstract

Electrochemical energy storage systems based on sulfur and lithium can theoretically delivery high energy with the further benefit of low cost. However, the working mechanism of this device involves the dissolutions of sulfur to high-molecular weight lithium polysulfides (LiPs with general formula Li_2S_n, $n \geq 4$) in the electrolyte during the discharge step. Therefore, the resulting migration of partially dissociated LiPs, by diffusion or under the effect of the electric field, to the lithium anode activates an internal shuttle mechanism, wastes the active material and in general leads to loss of performance and a reduced cycling stability. These drawbacks poses challenges to the commercialization of Li/S cells in the short term. In this study, we report on the decoration of reduced graphene oxide with MoO_3 particles to enhance interactions with LiPs and retain sulfur at the cathode side. The combination of experiments and density functional theory calculation demonstrated improvements in binding interactions between the cathode and sulfur species, enhancing the cycling stability of the Li/S half-cell.

1. Introduction

The world's growing demand for efficient and sustainable energy storage solutions, makes lithium-sulfur batteries (Li/S) a promising technology thank to their potential unique features, able to revolutionize the energy storage market [1]. Indeed, this battery chemistry offers several advantages over traditional lithium-ion systems, including higher energy density, and lower costs of production, with the additional benefit of sulfur being eco-friendly and abundant [2,3]. Li/S redox mechanism exploits a sequence conversion reactions that, through the formation of different Li_2S_x species, brings to the Li_2S solid phase as a final product [4]. This mechanism unavoidably implies the formation of different Li_2S_x polysulfide intermediates (Li_2S_x, where $3 \leq x \leq 8$) that are soluble in the typical organic liquid electrolyte used in batteries. This phenomenon leads to losses of the active material upon cycling while polysulfide "shuttle" to the lithium metal electrode where it reacts chemically and electrochemically.[5] To overcome problems related to sulfur dissolution, different strategies have been proposed to design electrodes by incorporating sulfur in micro and/or mesoporous carbon [6,7]. Different carbon morphologies have been reported as sulfur-host such as carbon aerogels [8,9], carbon nanotubes [10,11], graphene, etc. [12,13]. However, the effectiveness of sulfur confinement in carbon hosts depends not only on its porosity but also on its surface chemistry. Indeed, while elemental sulphur is non-polar and can be adsorbed well in the hydrophobic carbon matrix, Li_2S_x polysulphide and Li_2S are polar and adsorb poorly [14,15]. Thus, the formation of polysulphides and their consequent migration can not be totally hindered by a physical confinement within a porous carbon material. The retention of polar S-containing species at the positive electrode side upon cycling in batteries can be improved by implementing hydrophilic nanodomains on the host surface. This approach has the advantage to preserve the excellent affinity of elemental solfur with the hydrophobic carbon host, while polar species canabe confined locally by tailored moieties or nanophases. This approach can be realized *via* different methods, including doping with heteroatoms, functionalizing the surface by binding small polar groups as well as dispersing polar inorganic nano-material [16,17]. Among various carbon hosts, the decoration of graphene-based sulfur electrodes with different materials is widely reported in the state-of-art, exploring several functionalities and inorganic materials, such as metal oxides, metal sulfides, nitrides, metals and metal oxides, nitrogen, metal phosphides, metal carbides or hydroxides, amine groups and benzene-based groups [18–26]. Herein, we demonstrate for the first time in the literature the beneficial impact on the battery performance of the decoration of reduced graphene oxide by molybdenum oxides (MoO_3). This strategy allows an imporved LiPs absorption on the electrode surface and enhances the electrochemical performance in Li/S cells.

2. Results and discussion

2.1. Physico-chemical characterization of rGO and rGO/MoO_3

Reduced graphene oxide (rGO) and rGO decorated with MoO_3 nanoparticles (rGO/MoO_3) have been prepared by hydrothermal synthesis starting from Graphene oxide (GO): details of the syntheses are reported in the methodological section. Diffraction analysis has been performed to characterize rGo and the rGO/MoO_3 powders as shown in the **Figure 1a**. Both patterns show a broad peak between 15° to 35°, which is typical of disordered carbonaceous materials [27]. After reduction with $NaBH_4$, this peak is reduced in intensity while additional peaks at 38.4° and 65° appear, confirming the presence of MoO_3 (ICSD 151750), **Figures 1b** [28]. Raman spectroscopy has been performed to investigate additional local structural changes in the carbon host. As expected, both materials show the presence of the G-band due to C-sp^2 domains of the graphitic structure and of the D-band due to the lateral unsaturated bonds of the graphene hexagonal sheets as well as the local C-sp^3 centers in the disordered carbon. The presence of this band indicates the occurrence of extended defects or graphite-like nano-domains. The ratio between the intensities of the D-band and G-band (I_D/I_G) can give a qualitative indication of either the lateral size of the graphene sheets or the defect concentration in the hexagonal layers, being this last structural properties indirectly related to the oxidation degree of carbon [29]. The relation of intensities for the bands D and G has been determined in both samples to be about $I_D/I_G= 1.0$. Therefore, the addiction of MoO_3 does not change the structural properties of the rGO.

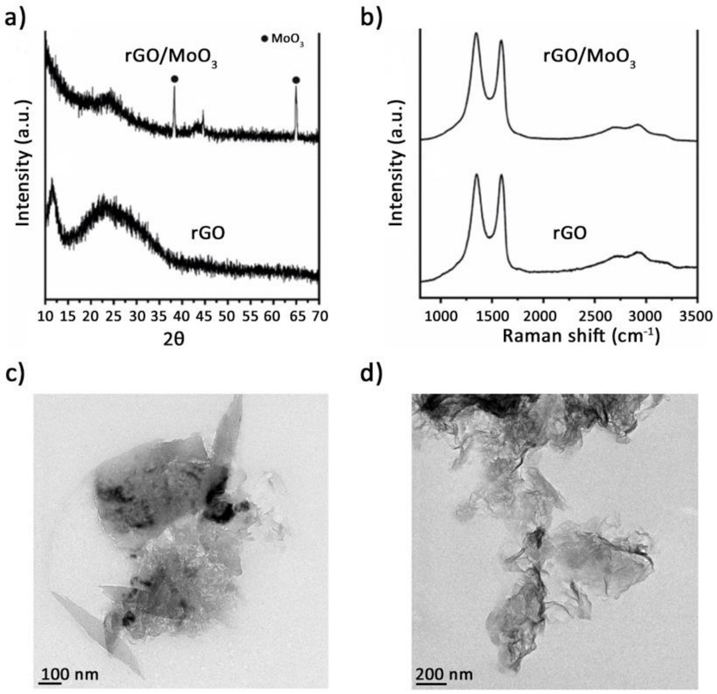

Figure 1. (a) X-ray diffraction pattern and **(b)** Raman spectra measured at 532 nm laser excitation wavelength of pristine rGo and of modified rGO/MoO_3. TEM images of the **(c)** reduced graphene oxide and **(d)** of the rGO/MoO_3.

Transmission electron microscopy (TEM) has been performed to investigate the morphology of samples and in particular the changes the decoration with MoO_3. Transmission micrographs of rGO shows flakes of 200-400 nm in diameter aggregated in secondary particles (see the **Figure 1c)**. A similar morphology has been observed also in the rGO/MoO_3 case, i.e. submicrometric sheets/flakes aggregated in micrometric particles, whereas the energy dispersive analysis (EDS) confirms the presence of Mo, see **Figure 1d** and **Figure S1** in supporting information section.

In order to get information about the surface composition of samples, X-ray photoelectron (XP) spectroscopy of rGO/MoO_3/Mo has been performed. The O 1s region of the XP spectra , **Figure 2a**, shows a significant peak at 530.9 eV, corresponding to the O-Mo bond, while the peaks at 531.8 eV and 533.1 eV belong to the O=C and O-C bonds, respectively [30,31]. The C 1s region, see the **Figure 2b**, shows a major peak at 284.5 eV corresponding to the sp^2 C-C bond, while the peaks at 285.3 eV, 286.2 eV and 288.5 eV belong to the sp^3 C-C, C-O and C=O bonds, respectively [32]. Turning to the Mo 3d region, the corresponding spectrum shown in the **Figure**

2c shows two intense peaks deconvoluted into a doublet with a separation of approximately 3.13 eV (236.13 eV) (Mo^{6+}) [33]..

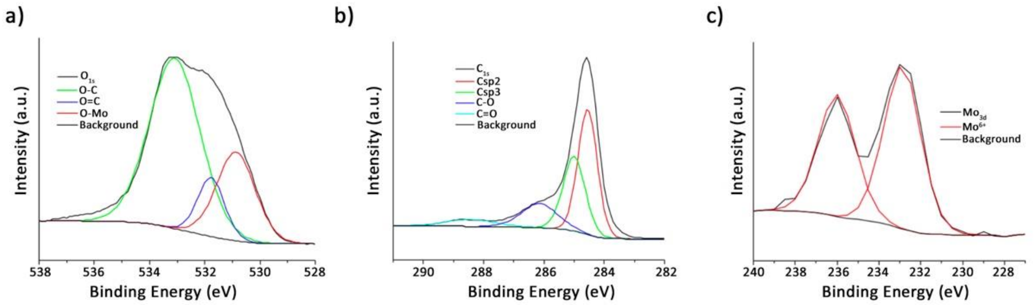

Figure 2. X-ray photoelectron spectroscopy spectra of rGO/MoO_3: **(a)** O 1s core level; **(b)** C 1s core level; **(c)** Mo 3d core level.

Overall, the decoration with MoO_3 of the rGO surface, does not impact nither the structure nor the morphology of the samples. The most relevant alteration is the presence on the hydrophobic surface or rGO of hydrophilic regions corresponding to the MoO_3 nanoparticles adsorbed over the host matrix..

2.2 Polysulfide adsorption capability of carbon hosts

A qualitative discrimination between the adsorption abilities of the rGO and of the rGO/MoO_3 has been obtained by optical white light observations (see Figure S1 in the Supporting Information section) of a polysulfide-rich solution left at room temperature in direct contact with each of the samples. After the absorption, the color of the polysulfide solution in equilibrium with modified rGO electrodic powder (**Figure S2a**) shifts to soft yellow, almost transparent, while the solution (**Figure S2b**) in equilibrium over rGO shows a strong yellow tone. To quantify the absorption ability, UV-vis spectroscopy of pristine carbon and of the rGO/MoO_3 after Li_2S_8 has been carried out: generally speaking higher concentrations of Li_2S_8 corresponds to darker shades of yellow and stronger absorbance around the blue spectrum**.** The UV-vis spectroscopy results (see the **Figure S2c** in SI section) are in good excellent agreement with previous qualitative observations, indeed the rGO/MoO$_3$ shows a lower blue spectrum absorbance compered to the bare rGO, indicating an improved chemisorption of polysulfides.

XPS measurements have been also performed on the rGO/MnO$_3$ sample after the adsorption of Li$_2$S$_8$ solution to investigate the surface speciation of S-conteining species and the absorption mechanim, as shown in **Figures 3**. In the O$_{1s}$ region (**Figure 3a)** the broad peak can be deconvoluted using three components centred at 530.75, 532.36 and 533.38 eV that possibly correspond to O-Mo, SO$_x^{2-}$ / CO$_3^{2-}$ / O=C and O-C, respectively [34–36]. Turning to the C$_{1s}$ region shown in the **Figure 3b**, as expected, a variety of XPS lines occurs: C$_{sp2}$ (C=C) at 284.61 eV, Csp^3 (C-C) / C-H at 285.6 eV, C-O / C-S at 286.44 eV, C=O at 289.03 eV and CO$_3^{2-}$ at 290.59 eV [32,36].

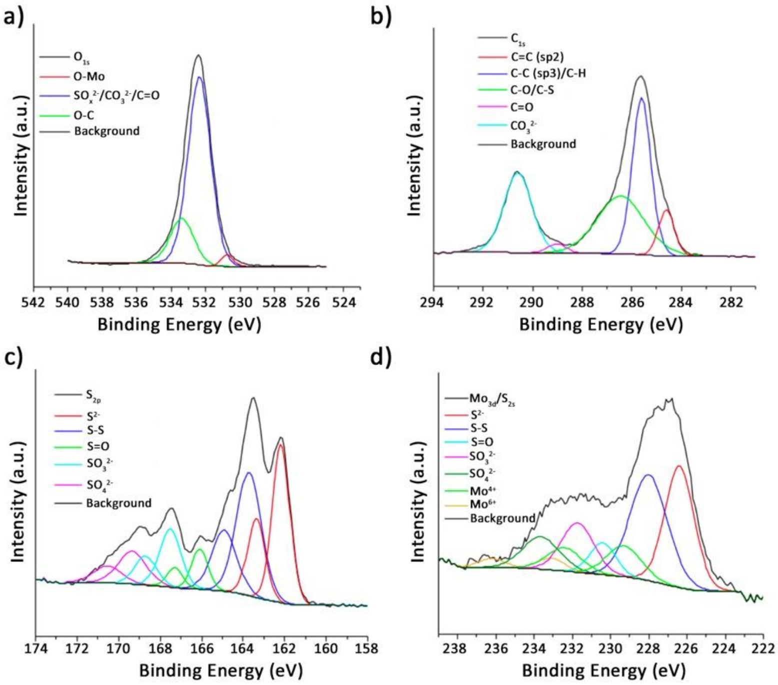

Figure 3. XPS analysis on the rGO/MoO$_3$ after Li$_2$S$_8$ adsorption: **(a)** O 1s, **(b)** C 1S, **(c)** O 1s, **(d)** Mo 3d/S 2s.

The S$_{2p}$ region of the XP spectra (see **Figure 3c)** shows a complex convoluted signal that can be de-convoluted by five doublet components with a relation between areas (S$_{2p1/2}$=S$_{2p3/2}$·0.5) due to p orbitals [1] and 1.19 eV of distance. The doublets are 162.18-163.37 eV, 163.72-164.91 eV, 166.09-167.28 eV, 167.51-168.7 eV and 169.33-170.52 eV, that correspond to S^{2-}, S-S, S=O, SO_3^{2-} and SO_4^{2-} respectively [37,38]. In agreement with the S_{2s} region, also the S_{2p} one (see the **Figure 3d**) can be de-convoluted (S^{2-} is located at 226.4 eV, S-S at 228.01 eV, S=O at 230.39 eV, SO_3^{2-} at 231.81 eV, and SO_4^{2-} at 233.63 eV).

The Mo_{3d} region shown in the **Figure 3d** unfortunately overlaps with the S_{2s} one, but a tentative de-convolution can be outlined. The doublet 229.42-232.56 eV corresponds to Mo^{4+} and 233.07-236.21 eV to other oxidation states of molybdenum, Mo^{6+} [39,40].

Overall, the XP data suggests that polysulfides interact with the MnO_3 particles by a spontaneous redox mechanism that leads to a surface reduction of Mo6+ to Mo4+/Mo3+ that parallels the formation of oxidized sulfur containing species, like sulfite and sulfate.

First-principles calculations were performed to understand further the interaction between the pristine rGO, the rGO/MoO_3, S_8 and LiPs. Adsorption on rGO/MoO_3 surface was modeled by considering only the on-top MoO_3 slab. The calculated adsorption energies (E_{ads}) for lithium sulfide (Li_2S_x) and sulfur (S_8) on each substrate is reported in **Figure 4a**. Given the presence of polar interacting moieties on both surfaces, in all cases LiPs show stronger interactions than apolar S_8. The E_{ads} of sulfur, mostly due to dispersion interactions, is quantitatively unaffected by the nature of the substrate. However, the ionic nature of lithium polysulfides determines a striking difference in their interaction with the two substrates: for long-chain Li_2S_8 and Li_2S_6 the adsorption energy on MoO_3 is increased by 30-40% with respect to rGO, while it is roughly doubled for Li_2S_4, Li_2S_2 and Li_2S. The equilibrium structures of LiPs-rGO and LiPs-MoO_3 are illustrated in **Figure 4b,c**. The strength of LiPs-MoO_3 interactions can be qualitatively ascribed to the abundance of polar sites on the oxide surface, where ionic moieties are easily stabilized. Dfference-charge density plots in **Figure S3** show instead that large charge accumulation (yellow surfaces) takes place on the O terminations of rGO surfaces, which bind Li_2S_x much more asymmetrically than MoO_3.

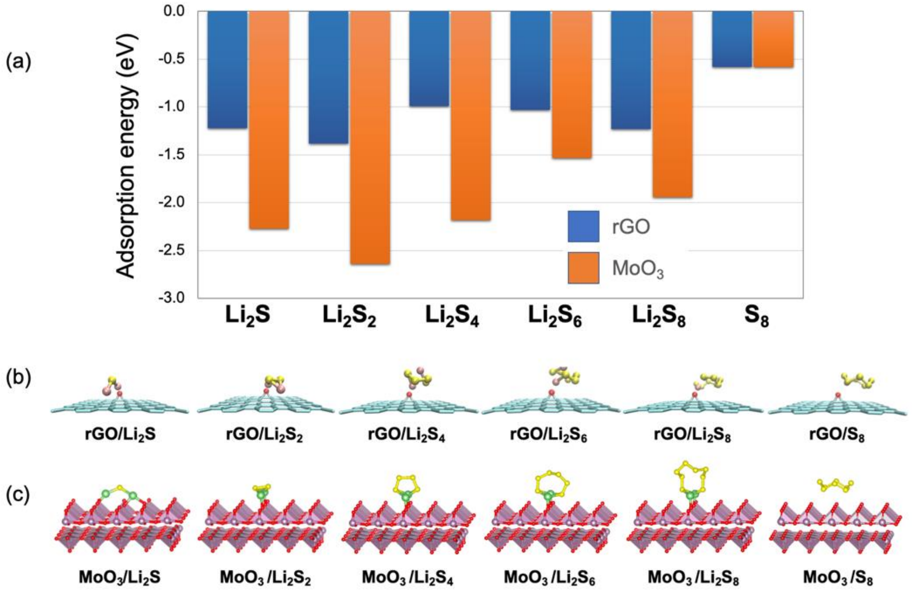

Figure 4. Results from first-principle calculations: (**a)** theoretical adsorption energy for Li_2S_x lithium polysulfide and S_8 sulfur species on reduced graphene oxide (orange bars) and MoO_3 (blue bars) surface; (**b-c)** optimized geometry structures for Li_2S_x–surface adsorbates on rGO and MoO_3.

Overall, one may speculate that the strong affinity of MoO_3 substrate to lithium polysulfide can effectively lead to two parallel mechansims that retain polysulfides on the porous positive electrode.

1. A spontaneous redox reaction of polysulfide with the molybdenum oxide leading to insoluble sulfates/sulfites;
2. A strong lithium polysufides chemisorption over the MoO_3 surface.

Both these mechanisms may limit the polysulfide dissolution and indirectly their diffusion to the lithium metal electrode ,thus mitigating the shuttle effect upon cycling.

On passing one also has to mention that the second mechanism (polysulfide chemisorption) may also contribute to the enhancement of the electrochemical conversion of long-chain polysufide to solid Li_2S_2. In fact, being the Li_2S_2/Li_2S rate-determining step of the overall mechanism[41,42], the surface trapping of polysulfide can speed up their reductive breakdown to form Li_2S_2 thus increasing the activity of this reagent at the electrode and indirectly boosting the overall conversion performance to Li_2S. Therefore, the synergetic effect MoO_3 as a polysulfide mediator is better than reduced graphene oxide, which is consistent with experimental results, see Supporting Information.

2.3. Electrochemical test of sulfur-rGO/MoO_3 electrode

For building the sulfur electrode, Li_2S_8 was deposited on rGO/MoO_3 by drop casting 20 µL of 1 M of Li_2S_8/DME solution. The solvent was evaporated to remove the excess weight before assembling the Li–S cell. The electrode was prepared with a sulfur mass loading of 4.9 mg·cm^{-2}. The sulfur content was approximately 50 wt.% of the total electrode mass (rGO/MoO_3/Mo and Al current collector = 5 mg cm^{-2}). Note that Li–S reported in the state-of-art are generally fabricated employing relatively large amounts of electrolyte, ranging from 1:20 to 1:30 sulfur to electrolyte (S/E; mg/uL) ratio. In this study, we built Li–S cells with a S/E ratio of 1:10. The performance of the composite rGO based electrodes loeaded with Li2S8 have been checked by galvanostatic cycling in Li/S aprotic cells using a DO:DME LiNO3 DOL:DME $LiNO_3$ 0.4M, LiTFSI 1M, electrolyte. Each cell has been activated by a preliminary discharge/charge cycle at low rate (i.e. 0.033C where 1C = 1675 mA·g^{-1}), whereas the standard cycling tests have been perfomed at 0.1C in the 1.9-2.7 V voltage range, The electrochemical performance of the rGO/MoO_3 electrode are shown in the **Figure 5.** This sample can deliver a discharge capacity ranging between 700 to 600 mAh·g^{-1} with high Coulombic efficiency and negligible capacity loss in prolonged cycling (more than 300 cycles). Differently, the performance of the rGO-based electrodes are unsatisfactory (**Figure S4** in SI section) and drastic capacity losses parallel scatterend and poor Coulombic efficiencies.

One may speculate that the enhancement of the performance in the rGO/MoO3-based electrodes can result from the mitigated “shuttle effect” caused by the limited dissolution of LiPs into the electrolyte and the subsequent minor interaction with Li metal surface at the negative electrode side. These beneficial effects apparently suppress the active material loss thus boosting the performance stability.

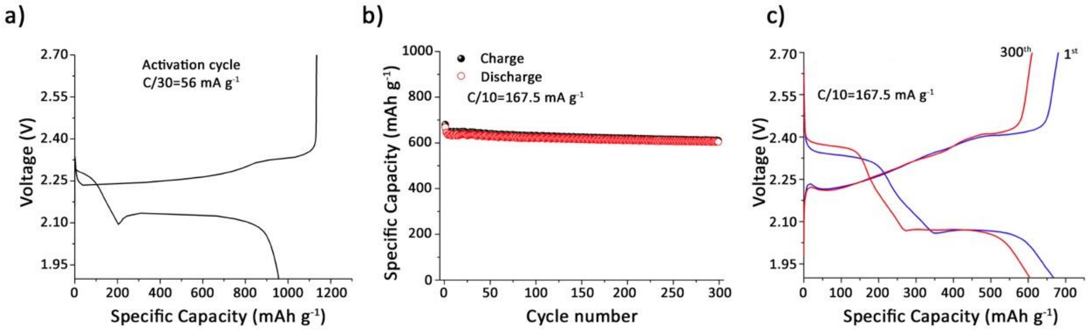

Figure 5. cycling performance of 4.9 mg cm^{-2} sulfur loading rGO/MoO$_3$/Li$_2$S$_8$ cathode in Li-half-cell. **(a)** Voltage profile during the activation cycle at C/30. **(b)** Prolonged cycling performance at C/10. **(c)** Voltage profiles comparison at cycle 1st and 300th. 1C=1675 mA g^{-1}); cell configuration Li/DOLDME LiTFSI 1.0 M, LiNO$_3$ 0.4 M/ rGO/MoO$_3$/Li$_2$S$_8$.

3. Conclusion

A new approach to the design of stable Li–S cells is proposed. The configuration involves the use of rGO substrate modified with MoO$_3$. The presence of this is demonstrated to improve interactions of S$_8$ and Li$_2$S$_n$ species with rGO-based electrode, thus substantially stabilizing the electrochemical performance. The MoO$_3$ functions as an efficient polysulfide mediator with a leading role of polysulfide scavenger, confining the active material at the cathode side and preventing migrations to the Li anode. This is demonstrated both by experimental and computational tests. The material here shows the potential of carbon electrode functionalization to build Li–S with good performance and long cycling stability.

4. Experimental section

4.1. Decoration of graphene with MoO$_3$ and Mo nanoparticles using hydrothermal synthesis

Graphene decorated with MoO$_3$ nanoparticles was prepared by hydrothermal synthesis. Graphene oxide (GO) was used as a precursor of graphene and molybdenum chloride (V) (MoCl$_5$, Sigma-Aldrich, Spain) as a precursor of MoO$_3$. Sodium borohydride (NaBH$_4$, ABCR) was employed as a reductant reagent for graphene nanosheets. First, graphene oxide suspension was sonicated for 20 minutes to get a homogeneous suspension. Then, molybdenum (V) chloride was added, and the solution was sonicated for 90 minutes. Subsequently, sodium borohydride was added, and the solution was sonicated again for 15 minutes. Finally, the solution was transferred to a Teflon-lined stainless-steel autoclave and heated in an electric oven at 120 °C for 24 hours. The resulting product was separated and dried at 100 °C for 24 hours. Finally, dried powder was grounded and sieved through <180 µm.

4.2. Characterization of rGO and rGO-MoO_3

Samples were characterized by X-ray diffraction (XRD) using a powder X-ray diffractometer (XRD, AXS D8 Advanced, Bruker, UK) equipped with Cu-Kα radiation ($\lambda = 0.15406$ nm) in the range from 10° to 70°. The step size was 0.03° and the step time of 0.5 s. The identification of the crystalline phases was made by using diffraction pattern files provided by JCPDS (International Centre for Diffraction Data). High-resolution transmission electron microscopy (HR-TEM) was employed using a JEOL JEM 2100F with an acceleration voltage of 200 kV and a field emission gun. Samples were prepared for HR-TEM by dispersing the final powders in ethanol. One drop of the dispersion was then dropped on the carbon-copper grid. Raman spectra were recorded on a Jobin Yvon labRam HR UV 800 with 532 nm laser excitation. XPS spectra were acquired in a SPECS spectrometer with a Phoibos 100 hemispherical analyzer. The base pressure in the UHV chamber was below 1.0×10^{-7} Pa. The X-ray source was monochromatic Al-Kα at 100 W X-ray powder and anode voltage of 14.00 kV. The photo-excited electrons were analyzed using a pass energy of 50eV for the survey spectra and 10 eV for the high-resolution core-level spectra. Data processing was performed using CasaXPS software.

4.3. Electrodes preparation and electrochemical characterization

Electrodes were prepared by mixing 200 mg of rGO or rGO/MoO_3 (80%), 10% PVDF (Aldrich) and 10% carbon Super P (Timcall), in 2 ml NMP (N-Methyl-2-pyrrolidone, Sigma Aldrich). The slurry solution was cast on aluminum foil using Doctor Blade coater (250 µm thickness). Following, the foil was dried on the heating plate at 100 ºC for 5 hours. After full dry 10 mm diameter electrodes were cut and further dried at 100ºC under vacuum. Coin-type cells were built using the rGO and rGO/MoO_3 electrodes. Firstly, 10µl of Li_2S_8 1M DME solution was drop cast on 10 mm electrodes and dried until total evaporation of DME at 80 °C. Whatman separator (12mm) was soaked with 50 µl of DOL: DME (1:1 w: w), $LiNO_3$ 0.4M, LiTFSI 1M, electrolyte and used between rGO/Li_2S_8 or $rGO/MoO_3/Li_2S_8$ and Lithium metal disk (11 mm). The cells were built by adding 20 µl on top of the electrode surface and 30 µl in the separator. Cells were cycled between 1.8 and 2.7 V using a current density of C/30 for 1 activation cycle and following a C/10 current for the following cycle (1C=1675.5 mA g^{-1}). All cycling tests were performed using a Maccor battery tester system. All assembling phases were performed in an Argon-filled glovebox. The Li_2S_8 polysulfide was prepared by dissolving 8 mole of Li metal (Chemetall) and 1 mole of S_8 (Aldrich) in 1 liter of DME solution and heating the solution at 80 ºC for 24 h until a red color was obtained. 10µl of 1M Li_2S_8 in DME (1,2-Dimethoxyethane, Sigma-Aldrich) solution is adsorbed on the surface of the electrode (10 mm diameter), and following DME solvent is evaporated at 80 °C. To analyze the adsorption properties of pristine rGo and rGO/MoO_3 to adsorb Li-polysulfides, 60 mg of each material was introduced in two different glass vials and 5ml of 0.01 M Li_2S_8 DME solution were added. Pictures of the solutions were taken at 10, 20 and 30 minutes, 1, 2, 18 and 24 hours. U-VIS spectroscopy tests (SME-E thunderOptics equipped with a mini light source (visible white radiation)) were performed to analyze the adsorption ability of both pristine rGo and rGO/MoO_3. The UV-spectrometer was SME-E thunderOptics and was equipped with a mini light source (visible white radiation). X-ray spectroscopy was performed on the surface of the rGO/MoO_3 electrode before and after adsorption/evaporation of 10µl of 1M Li_2S_8 in DME solution.

DFT calculations

Periodic density functional theory (DFT) calculations were performed using the open-source Quantum ESPRESSO software [43]. The PBE functional was adopted, together with projector-augmented wave (PAW) pseudopotentials, and DFT-D3 dispersion corrections [44] were added to improve the description of van der Waals and weak interactions. The kinetic energy cutoff for the plane-wave basis was set to 40 Ry. A 2x2x1 grid scheme was used to sample the k-points in all the systems. In calculations involving molybdenum atoms, the DFT+U method by Dudarev et al.

[45] was employed to correct for the localization of *d* electrons, using U_{eff} with a value of 6.3 eV. For both systems, the cell parameters of the pristine surface were relaxed while leaving a vacuum region of ~17 Å between the vertical periodic replicas of the surface. Consistently with other studies [46,47], the adsorption of the polysulfide on MoO3 was modeled along the (010) surface of the thermodynamically stable α-MoO_3 phase, consisting of one bilayer slab. Adsorbate-surface geometries were then optimized at the fixed cell parameters of the respective pristine surface. Finally, the adsorption energy was calculated as:

$$\mathrm{E}_{ads} = \mathrm{E}_{surf/Li-S} - \left(\mathrm{E}_{surf} + \mathrm{E}_{Li-S}\right)$$

where $E_{surf/Li/S}$ is the total energy of the polysulfide + surface, while E_{surf} and $E_{Li/S}$ are the energy of the surface and the polysulfide alone, respectively.

Acknowledgements

Juan Piñuela Noval acknowledges the Programa “Severo Ochoa” of Grants for Research and Teaching of the Principality of Asturias for the funds received for the elaboration of the Ph. D. Thesis (Ref.: BP20 041). Juan Piñuela Noval also thanks the grant “Ayuda de Estancias Breves en otros Centros de Investigación” within the Programa “Severo Ochoa” for the training in research and teaching in 2022 (Ref.: EB22-11). Daniel Fernández-González acknowledges the grant (Juan de la Cierva-Formación program) FJC2019-041139-I funded by MCIN/AEI/10.13039/501100011033 (Ministerio de Ciencia e Innovación, Agencia Estatal de Investigación). This research was supported by the project Investigación industrial de materiales estratégicos para baterías de ión-litio de alta densidad energética y coste optimizado en electromovilidad sostenible LiOn-HD, promoted by Iniciativas Estratégicas Sectoriales de Innovación Empresarial (Programa "Misiones CDTI"), en el marco del Programa Estatal de Liderazgo Empresarial en 1+D+I, del Plan Estatal de Investigación Científica y Técnica y de Innovación 2017-2020. Science and Innovation Ministery of Spain. The authors are grateful to Ainhoa Macías San Miguel from Nanomaterials and Nanotechnology Research Center (CINN) for providing technical assistance.

References

[1] Z. Wang, Y. Dong, H. Li, Z. Zhao, H. Bin Wu, C. Hao, S. Liu, J. Qiu, X. W. D. Lou, *Nat Commun* **2014**, *5*, DOI 10.1038/ncomms6002.

[2] M. Agostini, J. Y. Hwang, H. M. Kim, P. Bruni, S. Brutti, F. Croce, A. Matic, Y. K. Sun, *Adv Energy Mater* **2018**, *8*, DOI 10.1002/aenm.201801560.

[3] J. H. Lee, J. Kang, S. W. Kim, W. Halim, M. W. Frey, Y. L. Joo, *ACS Omega* **2018**, *3*, 16465–16471.

[4] K. Zhu, C. Wang, Z. Chi, F. Ke, Y. Yang, A. Wang, W. Wang, L. Miao, *Front Energy Res* **2019**, *7*, DOI 10.3389/fenrg.2019.00123.

[5] D. Su, D. Zhou, C. Wang, G. Wang, *Adv Funct Mater* **2018**, *28*, DOI 10.1002/adfm.201800154.

[6] Y. C. Ko, C. H. Hsu, C. A. Lo, C. M. Wu, H. L. Yu, C. H. Hsu, H. P. Lin, C. Y. Mou, H. L. Wu, *ACS Sustain Chem Eng* **2022**, *10*, 4462–4472.

[7] F. Sun, J. Wang, H. Chen, W. Li, W. Qiao, D. Long, L. Ling, *ACS Appl Mater Interfaces* **2013**, *5*, 5630–5638.

[8] Z. Zhang, Z. Li, F. Hao, X. Wang, Q. Li, Y. Qi, R. Fan, L. Yin, *Adv Funct Mater* **2014**, *24*, 2500–2509.

[9] Z. Li, X. Li, Y. Liao, X. Li, W. Li, *J Power Sources* **2016**, *334*, 23–30.

[10] L. Ma, H. L. Zhuang, S. Wei, K. E. Hendrickson, M. S. Kim, G. Cohn, R. G. Hennig, L. A. Archer, *ACS Nano* **2016**, *10*, 1050–1059.

[11] A. Abdul Razzaq, Y. Yao, R. Shah, P. Qi, L. Miao, M. Chen, X. Zhao, Y. Peng, Z. Deng, *Energy Storage Mater* **2019**, *16*, 194–202.

[12] R. Fang, S. Zhao, S. Pei, X. Qian, P. X. Hou, H. M. Cheng, C. Liu, F. Li, *ACS Nano* **2016**, *10*, 8676–8682.

[13] Y. Zhang, Z. Gao, N. Song, J. He, X. Li, *Mater Today Energy* **2018**, *9*, 319–335.

[14] Q. Pang, X. Liang, C. Y. Kwok, L. F. Nazar, *Nat Energy* **2016**, *1*, DOI 10.1038/nenergy.2016.132.

[15] J. Sun, J. Y. Hwang, P. Jankowski, L. Xiao, J. S. Sanchez, Z. Xia, S. Lee, A. V. Talyzin, A. Matic, V. Palermo, Y. K. Sun, M. Agostini, *Small* **2021**, *17*, DOI 10.1002/smll.202007242.

[16] J. Zhang, H. Huang, J. Bae, S. H. Chung, W. Zhang, A. Manthiram, G. Yu, *Small Methods* **2018**, *2*, DOI 10.1002/smtd.201700279.

[17] J. Liang, Z. H. Sun, F. Li, H. M. Cheng, *Energy Storage Mater* **2016**, *2*, 76–106.

[18] Z. Xiao, Z. Yang, L. Zhang, H. Pan, R. Wang, *ACS Nano* **2017**, *11*, 8488–8498.

[19] Y. Liu, A. Chatterjee, P. Rusch, C. Wu, P. Nan, M. Peng, F. Bettels, T. Li, C. Ma, C. Zhang, B. Ge, N. C. Bigall, H. Pfnür, F. Ding, L. Zhang, *ACS Nano* **2021**, *15*, 15047–15056.

[20] H. Li, J. Wang, Y. Zhang, Y. Wang, A. Mentbayeva, Z. Bakenov, *J Power Sources* **2019**, *437*, DOI 10.1016/j.jpowsour.2019.226901.

[21] G. Zhou, E. Paek, G. S. Hwang, A. Manthiram, *Nat Commun* **2015**, *6*, DOI 10.1038/ncomms8760.

[22] Z. Sun, J. Zhang, L. Yin, G. Hu, R. Fang, H. M. Cheng, F. Li, *Nat Commun* **2017**, *8*, DOI 10.1038/ncomms14627.

[23] Y. Tian, Y. Zhao, Y. Zhang, L. Ricardez-Sandoval, X. Wang, J. Li, *ACS Appl Mater Interfaces* **2019**, *11*, 23271–23279.

[24] S. Liu, X. Zhang, S. Wu, X. Chen, X. Yang, W. Yue, J. Lu, W. Zhou, *ACS Nano* **2020**, *14*, 8220–8231.

[25] J. Liu, X. Liu, Q. Zhang, X. Liang, J. Yan, H. H. Tan, Y. Yu, Y. Wu, *Electrochim Acta* **2021**, *382*, DOI 10.1016/j.electacta.2021.138267.

[26] H. Park, S. Lee, H. Kim, H. Park, H. Kim, J. Kim, M. Agostini, Y. Sun, J. Hwang, *Carbon Energy* **2024**, DOI 10.1002/cey2.472.

[27] A. Marjani, A. T. Nakhjiri, M. Adimi, H. F. Jirandehi, S. Shirazian, *Sci Rep* **2020**, *10*, DOI 10.1038/s41598-020-58472-y.

[28] P. Zheng, T. Liu, Y. Su, X. Yuan, L. Zhang, S. Guo, *J Alloys Compd* **2017**, *703*, 10–12.

[29] D. López-Díaz, M. López Holgado, J. L. García-Fierro, M. M. Velázquez, *Journal of Physical Chemistry C* **2017**, *121*, 20489–20497.

[30] S. H. Ha, Y. S. Jeong, Y. J. Lee, *ACS Appl Mater Interfaces* **2013**, *5*, 12295–12303.

[31] J. Światowska-Mrowiecka, S. De Diesbach, V. Maurice, S. Zanna, L. Klein, E. Briand, I. Vickridge, P. Marcus, *Journal of Physical Chemistry C* **2008**, *112*, 11050–11058.

[32] C. K. Chua, Z. Sofer, M. Pumera, *Chemistry - A European Journal* **2012**, *18*, 13453–13459.

[33] M. Anwar, C. A. Hogarth, R. Bulpett, *An XPS Study of Amorphous MoOa/SiO Films Deposited by Co-Evaporation*, **1990**.

[34] Y. Diao, K. Xie, S. Xiong, X. Hong, *J Electrochem Soc* **2012**, *159*, A1816–A1821.

[35] R. Xu, J. Lu, K. Amine, *Adv Energy Mater* **2015**, *5*, DOI 10.1002/aenm.201500408.

[36] Y. X. Mo, Y. J. Wu, Z. W. Yin, W. F. Ren, Z. G. Gao, P. F. Zhang, J. X. Lin, Y. Zhou, J. T. Li, L. Huang, S. G. Sun, *ChemistrySelect* **2020**, *5*, 8969–8979.

[37] H. Chen, A. Pei, D. Lin, J. Xie, A. Yang, J. Xu, K. Lin, J. Wang, H. Wang, F. Shi, D. Boyle, Y. Cui, *Adv Energy Mater* **2019**, *9*, DOI 10.1002/aenm.201900858.

[38] M. Sadd, M. Agostini, S. Xiong, A. Matic, *ChemPhysChem* **2022**, *23*, DOI 10.1002/cphc.202100853.

[39] H. J. Song, M. C. Sung, H. Yoon, B. Ju, D. W. Kim, *Advanced Science* **2019**, *6*, DOI 10.1002/advs.201802135.

[40] Q. Zhang, L. Pastor-Pérez, W. Jin, S. Gu, T. R. Reina, *Appl Catal B* **2019**, *244*, 889–898.

[41] J. Y. Hwang, H. M. Kim, S. Shin, Y. K. Sun, *Adv Funct Mater* **2018**, *28*, DOI 10.1002/adfm.201704294.

[42] X. Tang, Z. Xu, Z. Sun, J. Zhou, X. Wu, H. Lin, J. Rong, S. Zhuo, F. Li, *Energy Technology* **2019**, *7*, DOI 10.1002/ente.201900574.

[43] P. Giannozzi, O. Andreussi, T. Brumme, O. Bunau, M. Buongiorno Nardelli, M. Calandra, R. Car, C. Cavazzoni, D. Ceresoli, M. Cococcioni, N. Colonna, I. Carnimeo, A. Dal Corso, S. De Gironcoli, P. Delugas, R. A. Distasio, A. Ferretti, A. Floris, G. Fratesi, G. Fugallo, R. Gebauer, U. Gerstmann, F. Giustino, T. Gorni, J. Jia, M. Kawamura, H. Y. Ko, A. Kokalj, E. Kücükbenli, M. Lazzeri, M. Marsili, N. Marzari, F. Mauri, N. L. Nguyen, H. V. Nguyen, A. Otero-De-La-Roza, L. Paulatto, S. Poncé, D. Rocca, R. Sabatini, B. Santra, M. Schlipf, A. P. Seitsonen, A. Smogunov, I. Timrov, T. Thonhauser, P. Umari, N. Vast, X. Wu, S. Baroni, *Journal of Physics Condensed Matter* **2017**, *29*, DOI 10.1088/1361-648X/aa8f79.

[44] S. Grimme, J. Antony, S. Ehrlich, H. Krieg, *Journal of Chemical Physics* **2010**, *132*, DOI 10.1063/1.3382344.

[45] S. L. Dudarev, G. A. Botton, S. Y. Savrasov, C. J. Humphreys, A. P. Sutton, *Electron-Energy-Loss Spectra and the Structural Stability of Nickel Oxide: An LSDAU Study*, **1998**.

[46] Y. H. Lei, Z. X. Chen, *Journal of Physical Chemistry C* **2012**, *116*, 25757–25764.

[47] I. Badran, N. Sahar Riyaz, A. M. Shraim, N. N. Nassar, *Comput Theor Chem* **2022**, *1211*, DOI 10.1016/j.comptc.2022.113689.

Supporting Information

Enhancement of Li/S battery performance by a modified reduced graphene oxide carbon host decorated with MoO_3.

Juan Piñuela-Noval,[1] Daniel Fernández-González,[1] Marta Suárez,[1] Luis Felipe Verdeja,[2] Arcangelo Celeste,[3] Adriano Pierini,[3] Franco Mazzei,[4] Maria Assunta Navarra,[3] Sergio Brutti,[3] Adolfo Fernández,[1] Marco Agostini[4].

[1]Nanomaterials and Nanotechnology Research Center (CINN-CSIC), Universidad de Oviedo (UO), Principado de Asturias (PA), Avda. de la Vega, 4-6, 33940, El Entrego, Spain.

[2]Departamento de Ciencia de los Materiales e Ingeniería Metalúrgica, Escuela de Minas, Energía y Materiales, Universidad de Oviedo, Calle Independencia, s/n, 33004, Oviedo/Uviéu, Asturias, Spain.

[3] Department of Chemistry and Drug Technologies, Sapienza University of Rome, P.le Aldo Moro 5, 00185 Rome, Italy.

[4]Department of Chemistry, Università di Roma "La Sapienza", p.le Aldo Moro 5, 00185 Roma, Italy.

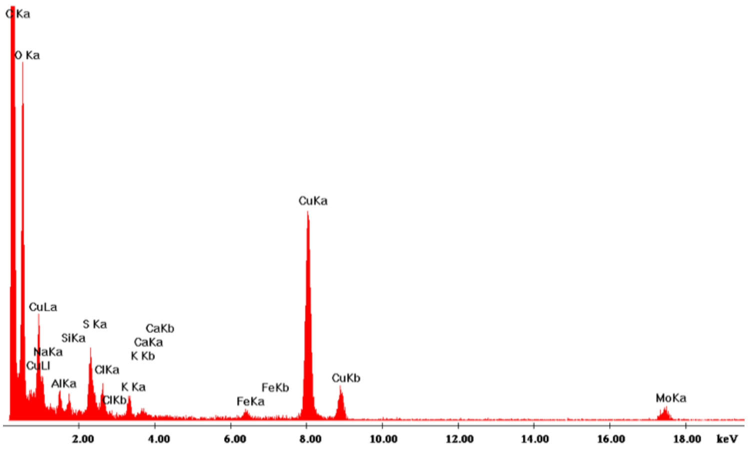

Figure S1. Energy Dispersive Spectroscopy (EDS) analysis related to TEM image of Figure 1d.

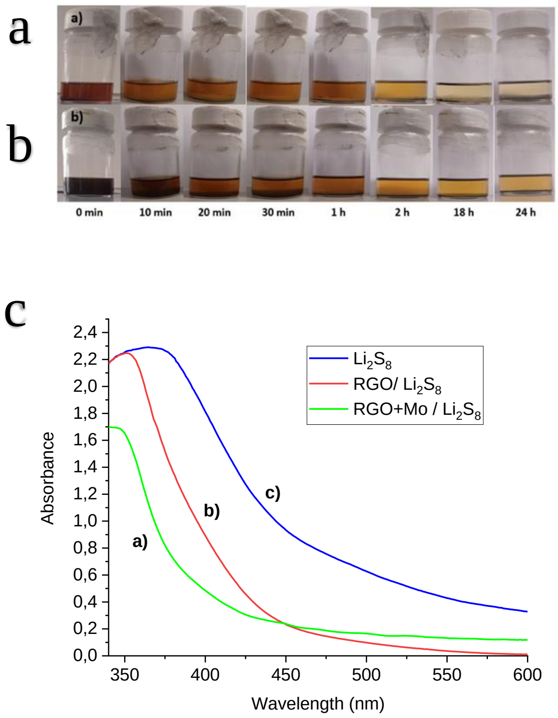

Figure S2. Results of the visual test adsorption: (a) rGO/MoO_3/Mo; (b) pristine rGO. Results of the absorbance test for the samples prepared by hydrothermal and colloidal synthesis and Li_2S_8 (c).

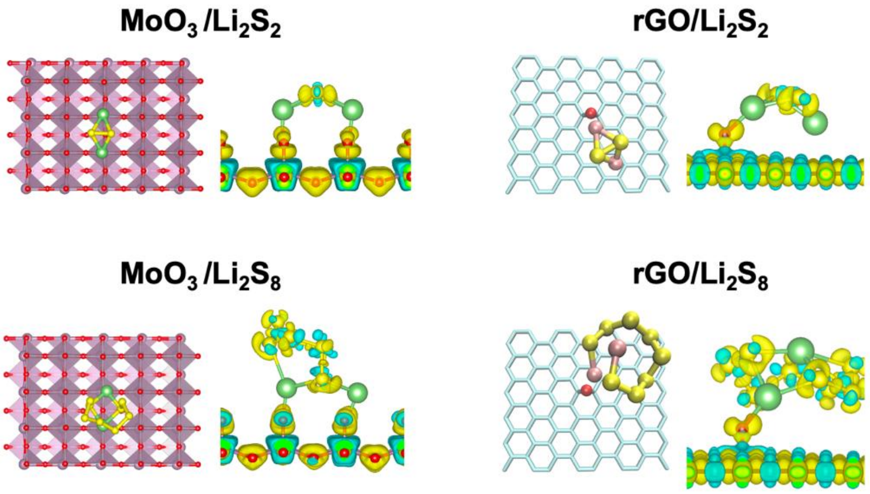

Figure S3. On-top view of DFT optimized structures (left) and charge density difference plots (right) for selected lithium polysulfide systems. Yellow and cyan isosurfaces in charge density plots represent charge accumulation and charge depletion regions, respectively.

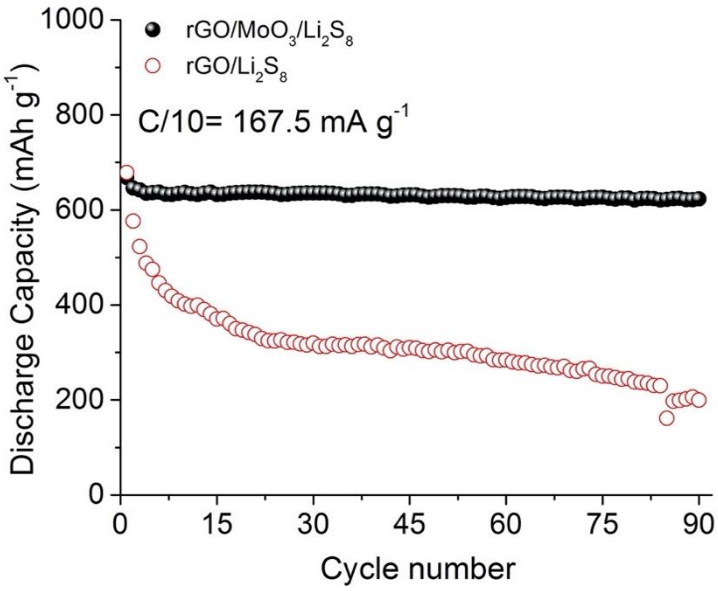

Figure S4. Cycling performance comparison between pristine rGO and modified rGO/MoO_3 in Li/S half-cell; 1st cycle C/30 and following C/10 (1C=1675 mA g^{-1}).

9. Conclusiones y trabajos a futuro

9.1. Disipadores de calor

Los trabajos realizados en esta tesis doctoral han permitido extraer varias conclusiones:

1. El molibdeno y el cromo forman carburos estables (MoC y Cr_3C_2) tras su tratamiento en el SPS por reacción con el grafito del constituyente matriz. De esta forma se logra un cuerpo denso con unas buenas propiedades mecánicas y unas adecuadas conductividades eléctrica y térmica. Estas propiedades, junto con el bajo coeficiente de expansión, hacen de estos materiales compuestos un candidato prometedor para el campo de la disipación de energía.

2. Se ha demostrado que era posible obtener composites grafito-MoC con propiedades adecuadas para la disipación de calor empleando una presión de compactación para obtener el cuerpo verde de 15 MPa (20 veces inferior a la empleada por investigadores) y con la tecnología SPS se logró obtener el cuerpo denso sinterizado a 2400 ºC (que es 200 ºC inferior a las empleadas por otros investigadores). Para las composiciones estudiadas, la que contenía un 10% en volumen de molibdeno, y fabricado mediante la ruta de la síntesis coloidal, proporcionaba las mejores propiedades: densificación del 85.24 %, Módulo de Young de 224.19 GPa, conductividad eléctrica de 1.07 MS/m, conductividad térmica que alcanza los 255.35 W/m K, y una resistencia a flexión de 53.45 MPa.

3. Por otra parte, se ha demostrado que los compuestos de grafito con cromo (carburo de cromo tras la sinterización) permitían obtener compuestos densos con mejores propiedades, pero a una temperatura de sinterización notablemente inferior a la requerida en el caso del sistema carbono-molibdeno. De entre las composiciones estudiada, la que contenía un 7% en volumen proporcionaba las mejores propiedades: densificación del 86.22%, Módulo de Young de 52.7 GPa, conductividad eléctrica de 0.79 MS/m, conductividad térmica que alcanza los 264 W/m K, y una resistencia a flexión de 38.97 MPa. Contenidos superiores al 7% en volumen de cromo no permitieron una mejora de las propiedades porque la fase líquida se perdía por extrusión en los bordes de la pieza.

4. Además, se ha demostrado que la ruta de síntesis coloidal permitía lograr una mejor distribución de la segunda fase en el material compuesto, lo que se trasladaba a las propiedades finales del composite. De esta manera, para el contenido en cromo óptimo de cromo (7% en volumen) en el composite, se lograron las mejores propiedades con una temperatura de sinterización de tan solamente 1900 ºC: densificación del 93.57%, Módulo de Young de 51.4 GPa, conductividad eléctrica de 0.75 MS/m, conductividad térmica que alcanza los 370.1 W/m K, una resistencia a flexión de 117.5 MPa y un coeficiente de expansión de $3.2 \cdot 10^{-6}$ K^{-1}. De esta manera, se logra una conductividad térmica relativa de 149.2 frente a los 102.1 que se obtenían para el mejor composite de grafito-MoC, y los 87.8 y 43 del aluminio y el cobre, respectivamente, haciendo del composite grafito-Cr_3C_2 una potencial alternativa para la disipación de calor.

Tras alcanzar los resultados mostrados en esta parte de la tesis, surgen nuevas ideas que pueden ser tenidas en cuenta para trabajos futuros:

- Por una parte, escalado de la ruta de síntesis coloidal para la fabricación a escala industrial de los composites grafito – metal (Mo y Cr) para su comercialización. Realizar pruebas relacionadas con el apantallamiento de neutrones para valorar el posible uso del cromo como segunda fase en los composites de grafito empleados en los colimadores del acelerador de partículas del CERN.

- Introducción de una tercera fase que permita alcanzar una mayor conductividad térmica: fibras de carbono y/o un tejido carbono-carbono colocados en la dirección perpendicular a la aplicación de la presión.

- Búsqueda de nuevos sistemas carbono (grafito)-metal (níquel) que puedan seguir reduciendo las condiciones de fabricación sin conducir a una merma en las propiedades funcionales de disipación de calor o apantallamiento de neutrones.

9.2. Almacenamiento de energía

Por su parte, las investigaciones centradas en las celdas electroquímicas de baterías Li-ion y Li-S han reportado varias conclusiones de gran interés:

1. El empleo de materiales compuestos de grafito con carburo de cromo o grafito con carburo de molibdeno como material anódico junto con un 20% de

nanopartículas de silicio, permite lograr una mejora sustancial de las propiedades electroquímica de las baterías de Li-Ion. Esta mejora en las propiedades electroquímicas se logra como consecuencia de unas superiores propiedades mecánicas conferidas por los carburos metálicos que soportan mejor los cambios de volumen que experimentan las partículas de silicio durante el proceso de litiación y delitiación. Así pues, la presencia de los carburos permite estabilizar el rendimiento electroquímico (en el entorno de los 250 $mAh \cdot g^{-1}$ de capacidad específica) por encima de los 400 ciclos, sin una caída evidente, especialmente en el caso del composite grafito-MoC.

2. El empleo del nanocomposite formado por óxido de grafeno reducido decorado con MoO_3 en los electrodos de las baterías de Li-S permite mejorar las prestaciones electroquímicas de este tipo de baterías. El S_8 y el Li_2S_n presentan una buena interacción con el óxido de grafeno reducido conduciendo a una mejora de la estabilidad electroquímica, mientras que el MoO_3 actúa como un *scavenger* de polisulfuros, confinando el material activo en el lado catódico y evitando las migraciones hacia el ánodo de litio. Así pues, el ciclado galvanostático, partiendo de un primer ciclo de activación, ha puesto de manifiesto el buen funcionamiento de este material: más de 300 ciclos con una capacidad específica estable por encima de los 600 $mAh\ g^{-1}$.

Tras alcanzar los resultados mostrados en esta parte de la tesis, surgen nuevas ideas que pueden ser tenidas en cuenta para trabajos futuros:

- Empleo de la ruta coloidal para obtener los composites de grafito con carburos metálicos para lograr así una mejora en las propiedades mecánicas y en el comportamiento electroquímico de las baterías de Li-Ion.

- Estudio de la modificación superficial dentro de los grafitos con carburos para lograr así un mayor rendimiento electroquímico.

- Estudio del escalado a nivel industrial del proceso de fabricación por vía hidrotermal del nanocomposite rGO-MoO_3 para su empleo en las baterías de Li-S.

10. Conclusions and future work

10.1. Heat sinks

Research conducted in this doctoral thesis has allowed us to extract several conclusions:

1. Molybdenum and chromium form stable carbides (MoC and Cr_3C_2) after their treatment in the spark plasma sintering apparatus by reaction with graphite of the matrix constituent. This way, it is possible to obtain a dense body with good mechanical properties and suitable electrical and thermal conductivities. These properties, together with the low thermal expansion coefficient, make these composite materials a promising candidate for the heat dissipation.

2. We have demonstrated that it was possible to obtain graphite-MoC composites with the suitable properties for the heat dissipation using a pressure of 15 MPa to obtain green bodies, which is 20 times lower than that used by other researchers. On another note, the SPS technology allowed to obtain the sintered dense body at 2400 ºC, which is 200 ºC lower than that used by other researchers. For the studied compositions, that of 10 vol. % Mo and manufactured by means of the colloidal processing route provided the best properties: densification rate of 85.24 %, Young modulus of 224.19 GPa, electrical conductivity of 1.07 MS/m, thermal conductivity of 255.35 W/m K, and flexural strength of 53.45 MPa.

3. On the other hand, we have demonstrated that the composites of graphite with chromium (chromium carbide after sintering) allowed to obtain dense bodies with better properties, although at a sintering temperature noticeably lower than that required in the case of the carbon-molybdenum system. From all the studied compositions, that containing a 7 vol. % Cr provided the best properties: densification of 86.22%, Young modulus of 52.7 GPa, electrical conductivity of 0.79 MS/m, thermal conductivity of 264 W/m K, and a flexural strength of 38.97 MPa. Contents in chromium exceed the 7 vol. % did not reported an improvement in the properties because the liquid phase produced chromium losses at the borders of the part due to extrusion.

4. Moreover, we have demonstrated that the colloidal synthesis route allowed to obtain a better distribution of the second phase in the composite, which translated into the final properties of the material. Therefore, for the optimum chromium

content (7 vol. %) in the composite, the best properties were obtained with a sintering temperature of only 1900 ºC: densification of 93.57%, Young modulus of 51.4 GPa, electrical conductivity of 0.75 MS/m, thermal conductivity of 370.1 W/m K, flexural strength of 117.5 MPa and coefficient of thermal expansion of $3.2 \cdot 10^{-6}$ K^{-1}. This way, it is possible to obtain a relative thermal conductivity of 149.2 in front of the 102.1 that were obtained in the case of the graphite-MoC composite, and the 87.8 and 43 of the aluminum and copper, respectively, which makes the composite graphite-Cr_3C_2 a potential alternative for the heat dissipation.

After reaching the results shown in this doctoral thesis, there are several possible research lines that might be considered in future research works:

- On the one hand, scalation of the colloidal synthesis route for the manufacture at the industrial scale of the graphite-metal (Mo and Cr) composites for their commercialization. Making tests oriented to analyze the neutron shielding to validate whether it is possible to use chromium as second phase in the composites of graphite used in the collimators of the Large Hadron Collider of the CERN.

- Introduction of a third phase that might allow to reach a greater thermal conductivity: carbon fibers and/or a carbon-carbon fabric, placed in the perpendicular direction to the applied pressing.

- Searching new systems carbon (graphite)-metal (nickel) that might allow reducing the manufacturing conditions without leading to a deterioration of the functional properties of heat dissipation or neutron shielding.

10.2. Energy storage

On the other hand, research conducted in the field of the electrochemical cells of the Li-Ion and Li-S batteries has provided us several conclusions:

1. The utilization of composites of graphite with chromium carbide or graphite with molybdenum carbide as anodic material together with 20% of silicon nanoparticles allows achieving a substantial improvement of the electrochemical properties of the Li-Ion batteries. This improvement in the electrochemical properties is achieved as a consequence of the superior mechanical properties conferred by the metallic carbides, which resist better to the volume changes that the silicon particles

experience during the lithiation and delithiation process. Thus, the presence of the carbides allows stabilizing the electrochemical performance (in around of 250 mAh·g^{-1} of specific capacity) for more than 400 cycles, without an evident fall, especially in the case of the graphite-MoC composite.

2. The use of the nanocomposite formed by reduced graphene oxide decorated with MoO_3 in the electrodes of the Li-S batteries allows improving the electrochemical properties of this type of batteries. The S_8 and the Li_2S_n exhibit a better interaction with the reduced graphene oxide leading to an improvement of the electrochemical stability, while the MoO_3 acts as a scavenger of polysulphides, confining the active material in the cathodic side, which avoids the migrations towards the lithium anode. Therefore, the galvanostatic cycling, starting from a first cycle of activation, has revealed the good functioning of this material: more than 300 cycles with a specific capacity stable above 600 mAh g^{-1}.

After reaching the results showed in this part of the doctoral thesis, there are new ideas that might be taken into consideration for future research works:

- Utilization of the colloidal synthesis route to obtain composites of graphite with metallic carbides to achieve an improvement of the mechanical properties and in the electrochemical behavior of the Li-Ion batteries.

- Study of the surface modification of the graphite with carbides to achieve a better electrochemical performance.

- Evaluation of the scalation up to the industrial level of the process to manufacture via hydrothermal synthesis the rGO-MoO_3 composite for its utilization in the Li-S batteries.